Neuron

Article

Improvement of sensory deficits in fragile X mice by increasing cortical interneuron activity after the critical period

Graphical abstract

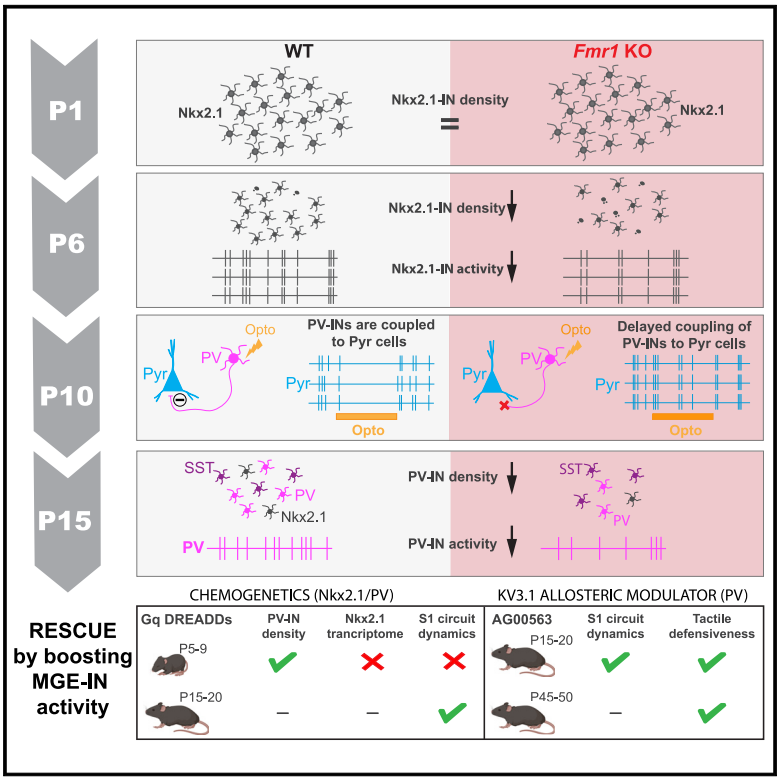

Highlights

- PV interneurons and MGE precursors are hypoactive in developing S1 of *Fmr1* KO mice
- PV neurons are decoupled from pyramidal cells until the second postnatal week
- Lower density of PV cells in S1 of *Fmr1* KO mice and in postmortem FXS human tissue
- Boosting PV activity in S1 ameliorates tactile defensiveness in *Fmr1* KO mice

Authors

Nazim Kourdougli, Anand Suresh, Benjamin Liu, ..., Benjamin J. Hall, Cédric Mombereau, Carlos Portera-Cailliau

Correspondence

cpcailliau@mednet.ucla.edu

In brief

Kourdougli et al. use all-optical *in vivo* approaches to show that parvalbumin interneurons are hypoactive and decoupled from excitatory partners in the developing neocortex of fragile X syndrome model mice. Restoring the activity of remaining PV cells after the second postnatal week (not earlier) ameliorates sensory hypersensitivity in the mouse model.

Kourdougli et al., 2023, Neuron *111*, 1–18
September 20, 2023
https://doi.org/10.1016/j.neuron.2023.06.009

CellPress

Neuron

CellPress
OPEN ACCESS

Article

Improvement of sensory deficits in fragile X mice by increasing cortical interneuron activity after the critical period

Nazim Kourdougli,[1] Anand Suresh,[1] Benjamin Liu,[1] Pablo Juarez,[4] Ashley Lin,[1] David T. Chung,[1] Anette Graven Sams,[7] Michael J. Gandal,[3] Verónica Martínez-Cerdeño,[4,5] Dean V. Buonomano,[1,6] Benjamin J. Hall,[7] Cédric Mombereau,[7] and Carlos Portera-Cailliau[1,2,8,*]

[1]Department of Neurology, UCLA, Los Angeles, CA, USA
[2]Department of Neurobiology, UCLA, Los Angeles, CA, USA
[3]Department of Psychiatry, UCLA, Los Angeles, CA, USA
[4]Department of Pathology, UC Davis, Davis, CA, USA
[5]MIND Institute, UC Davis, Davis, CA, USA
[6]Department of Psychology, UCLA, Los Angeles, CA, USA
[7]Lundbeck A/S H, Ottiliavej 9, 2500 Copenhagen, Denmark
[8]Lead contact
*Correspondence: cpcailliau@mednet.ucla.edu
https://doi.org/10.1016/j.neuron.2023.06.009

SUMMARY

Changes in the function of inhibitory interneurons (INs) during cortical development could contribute to the pathophysiology of neurodevelopmental disorders. Using all-optical *in vivo* approaches, we find that parvalbumin (PV) INs and their immature precursors are hypoactive and transiently decoupled from excitatory neurons in postnatal mouse somatosensory cortex (S1) of *Fmr1* KO mice, a model of fragile X syndrome (FXS). This leads to a loss of parvalbumin INs (PV-INs) in both mice and humans with FXS. Increasing the activity of future PV-INs in neonatal *Fmr1* KO mice restores PV-IN density and ameliorates transcriptional dysregulation in S1, but not circuit dysfunction. Critically, administering an allosteric modulator of Kv3.1 channels after the S1 critical period does rescue circuit dynamics and tactile defensiveness. Symptoms in FXS and related disorders could be mitigated by targeting PV-INs.

INTRODUCTION

Neurodevelopmental disorders (NDDs) arise due to changes in developmental trajectories of neurons during the early stages of circuit assembly in the brain. Although symptoms of NDDs, such as intellectual disability and autism, are first recognized in the toddler stage, circuit differences are likely present at birth and may begin even earlier.[1] From a therapeutic perspective, identifying the earliest circuit changes in NDDs is critical because early interventions are more likely to redirect the trajectory of neural development before it is irreversibly changed as a consequence of genetic and/or environmental factors.

Differences in GABAergic inhibition and excitability have been implicated in the origins of NDDs and autism and proposed as targets for therapy.[2–5] However, the prevalent notion that an imbalance in excitatory and inhibitory signaling is associated with NDDs is principally based on observations in adulthood. In the last decade, as our understanding of cortical development grew significantly, there has been increased awareness about the important developmental role of inhibitory interneurons (INs) in shaping neuronal circuits.[6,7] The typical density, function, and integration of INs into cortical networks all depend on genetic and activity-dependent programs.[8] Deviations from the usual trajectory of these developmental programs in NDDs could have an impact on functional circuit assembly.[4,5] For example, hypofunction of cortical INs has been described in multiple models of autism and other psychiatric conditions,[4,9–11] but the nature of GABAergic population dynamics throughout neonatal development in NDDs remains an unexplored territory.

To investigate this, we focused on fragile X syndrome (FXS) because it is the most common single gene cause of intellectual disability and autism[12] and because hypoactivity of fast-spiking parvalbumin (PV) INs has been observed repeatedly in *Fmr1* knockout mice (*Fmr1* KO, referring to both male *Fmr1*$^{-/y}$ and female *Fmr1*$^{-/-}$ mice), the principal animal model of FXS.[13–16] Additionally, reciprocal connectivity of fast-spiking INs with excitatory cells is altered in layer (L) 4 of S1 in developing *Fmr1* KO mice.[15,17,18] In this study, we examined the developmental origins of PV-IN hypoactivity in L2/3 of S1 *in vivo* because we previously identified early postnatal circuit changes in *Fmr1* mice (excessive network synchrony and reduced adaptation to repetitive tactile stimulation) that could be associated with

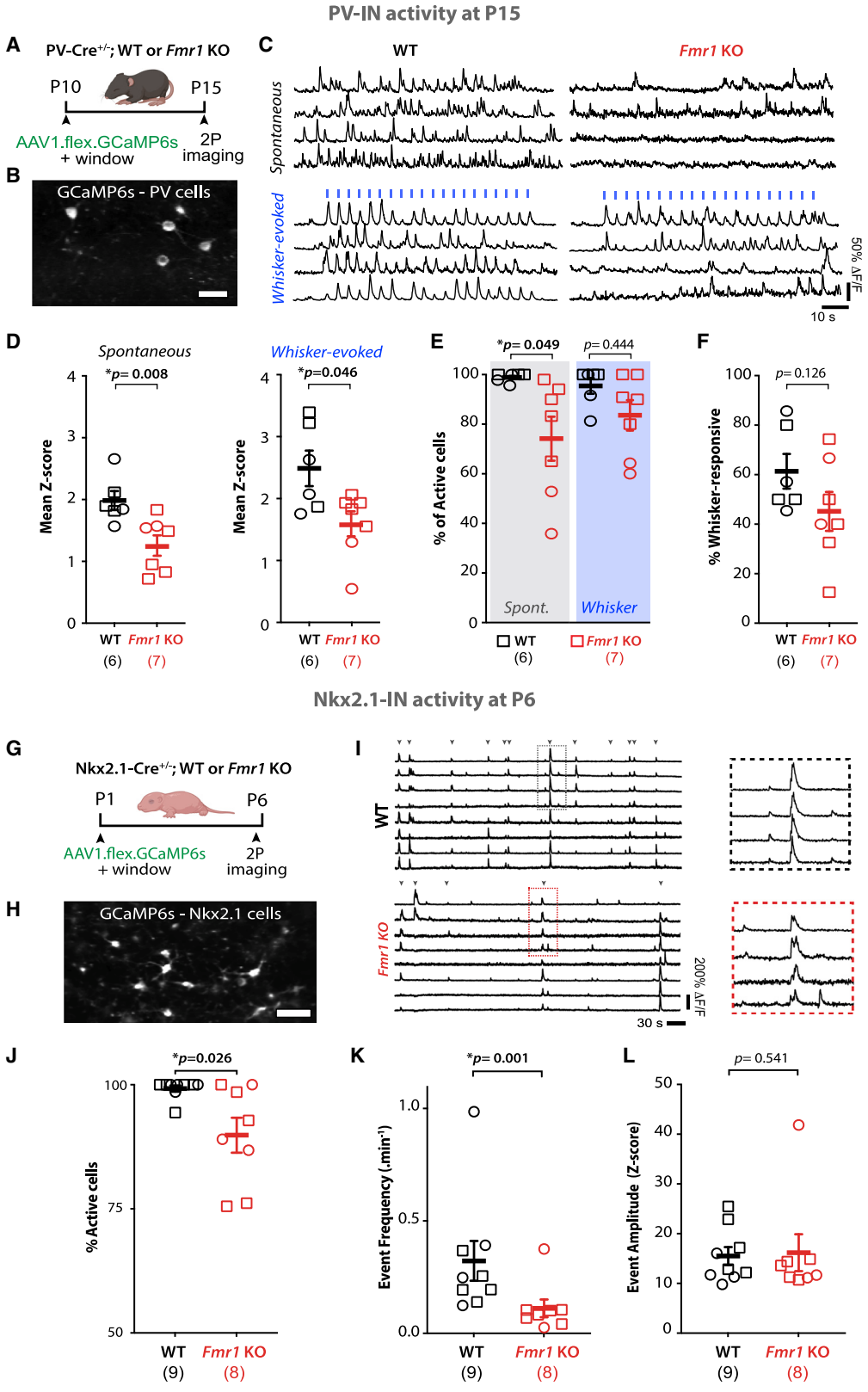

(legend on next page)

Please cite this article in press as: Kourdougli et al., Improvement of sensory deficits in fragile X mice by increasing cortical interneuron activity after the critical period, Neuron (2023), https://doi.org/10.1016/j.neuron.2023.06.009

reduced PV-IN activity.[19,20] We show that PV-INs and their immature counterparts from the medial ganglionic eminence (MGE), which express the transcription factor Nkx2.1, are hypoactive in S1 as early as postnatal day (P) 6 and fail to modulate excitatory neurons in *Fmr1* KO mice before P15. Their density is also reduced in S1 from early postnatal development to adulthood in *Fmr1* KO mice and, remarkably, also in humans with FXS. Interestingly, an early chemogenetic intervention to increase Nkx2.1-IN firing in *Fmr1* KO mice at P5–P9 failed to restore circuit dysfunction despite partially correcting their S1 transcriptome, whereas a delayed intervention at P15–P20 (post S1 critical period) was more successful. Finally, boosting PV-IN activity more globally with a Kv3.1 channel modulator at P15–P20 significantly improved both circuit and behavioral sensory phenotypes of *Fmr1* KO mice. Thus, circuit changes in FXS (and perhaps in other NDDs) can be reversed by targeting PV-INs, but the timing of this intervention may be critical.

RESULTS

Reduced activity of cortical PV-INs and MGE-derived INs in early postnatal *Fmr1* KO mice

Several *in vivo* studies have shown that the activity of cortical PV-INs is reduced in adult *Fmr1* KO mice.[13,14] Moreover, we previously discovered pronounced circuit changes in S1 during the critical period at P14–P16 that could be due to reduced inhibition, including fewer whisker-responsive excitatory pyramidal (Pyr) neurons and lack of neuronal adaptation to repeated stimulation. To assess whether PV-INs were also hypoactive in S1 earlier in development, we used *in vivo* two-photon calcium imaging at P15 to record from them in S1 of PV-Cre;WT or *Fmr1* KO mice injected with AAV1-CAG-Flex-GCaMP6s at P10 (Figures 1A–1C). This approach led to GCaMP6s expression in ~80% of PV-INs in L2/3 of the transfected region (Figures S1A and S1B). We found that both spontaneous and whisker-evoked activity of PV-INs were significantly reduced by ~35% in *Fmr1* KO mice (n = 7) compared with WT mice (n = 6) (Figures 1D–1F). The percentage of PV-INs that were spontaneously active was also significantly reduced (Figure 1E), although the percentage of whisker-responsive PV-INs was not different from controls (Figure 1F).

Somatostatin-expressing INs (SST-INs) and PV-INs both arise from a common precursor in the MGE.[21–23] Therefore, we also recorded the activity of SST-INs *in vivo* at P15 in *Sst*-FlpO$^{+/-}$ mice (Figures S2A and S2B). We did not find significant differences between genotypes in either spontaneous or whisker-evoked activity, although the percentage of whisker-responsive SST-INs was lower in *Fmr1* KO mice (Figures S2C–S2E). Thus, PV-INs in S1, but not SST-INs, manifest significant hypoactivity in 2-week-old *Fmr1* KO mice.

During the period that spans from the establishment of barrels to the closure of S1 critical period, GABAergic assemblies display synchronous dynamics that help shape developing circuits.[24,25] We next investigated whether differences in MGE-IN activity during the first postnatal week contribute to previously reported signs of early cortical circuit dysfunction.[19,26,27] Cortical PV-INs do not express PVALB before P10,[23,28,29] but their immature precursors from the MGE can be identified through their expression of the transcription factor *Nkx2.1*. We used *in vivo* calcium imaging to record from MGE-INs at P6 in Nkx2.1-Cre mice injected with AAV1-CAG-Flex-GCaMP6s into S1 at P1 (Figures 1G–1I), which led to 43% of Nkx2.1-INs expressing the indicator in the transfected region (Figures S1C and S1D); a small fraction of Nkx2.1-INs also express SST at P6 (Figures S1E–S1H). Early cortical network activity is dominated by large and infrequent synchronous network events that propagate as waves.[30,31] We confirmed that MGE-INs participated in synchronous cortical activity, as previously reported.[32] However, we found a significantly lower proportion of active Nkx2.1-INs and a lower frequency of synchronous MGE-IN network events in *Fmr1* KO mice (n = 8) compared with WT controls (n = 9), although the amplitude of these events was similar (Figures 1J–1L). Hence, Nkx2.1-INs (which give rise to PV- and SST-INs) are hypoactive at P6 and less likely to participate in synchronous network activity.

Future PV-INs within the Nkx2.1-IN population fail to modulate Pyr cells in neonatal *Fmr1* KO mice

The hypoactivity of Nkx2.1-INs could account for the previously reported hypersynchrony and hyperactivity of Pyr neurons in early postnatal *Fmr1* KO mice.[19,26,27] Indeed, the maturation of cortical

Figure 1. PV-INs and their MGE-derived immature INs are hypoactive in S1 of developing *Fmr1* KO mice

(A) Cartoon of experimental design for in vivo recordings at P15.

(B) Example field of view of PV-INs expressing AAV1-flex-GCaMP6s in S1 cortex of PV-Cre mice (scale bars, 25 μm).

(C) Representative traces of PV-IN calcium transients in WT and *Fmr1* KO mice. Whisker stimulation (blue bars, 1 s at 10 Hz, 3 s inter-stimulus interval [I.S.I.]).

(D) Mean *Z* scores of PV-INs at P15 are significantly lower in *Fmr1* KO than in WT mice. In (D)–(F) and (J)–(L), symbols represent individual mice (sample size in parenthesis, females = circles, males = squares. (Spontaneous: 1.98 ± 0.15 for WT vs. 1.28 ± 0.17 for *Fmr1* KO; whisker-evoked: 2.49 ± 0.29 for WT vs. 1.61 ± 0.21 for *Fmr1* KO, respectively; p = 0.008 and p = 0.046, Mann-Whitney (M-W) U test, n = 6 WT and n = 7 *Fmr1* KO mice.)

(E) Percentage of active PV-INs in WT and *Fmr1* KO mice (spontaneous: 98.9% ± 0.8% for WT vs. 74.2% ± 8.9% for *Fmr1* KO; p = 0.049, whisker-evoked: 95.5% ± 3.2% for WT vs. 83.6% ± 6.1% for *Fmr1* KO, p = 0.444, M-W U test).

(F) Percentage of stimulus-locked PV-INs (61.4% ± 6.9% for WT vs. 45.2% ± 7.9% for *Fmr1* KO; p = 0.126, M-W t test).

(G) Experimental design for *in vivo* recordings at P6.

(H) Example field of view of Nkx2.1-INs expressing AAV1-flex-GcaMP6s in S1 cortex of *Nkx2.1*-Cre mice (scale bars, 25 μm).

(I) Example calcium traces of Nkx2.1-INs in WT and *Fmr1* KO mice. Inset shows expanded traces for representative synchronous network events.

(J) The percentage of active Nkx2.1-INs at P6 was significantly lower in *Fmr1* KO mice than in WT controls. (99.2% ± 0.6% for WT and 89.8% ± 3.5% for *Fmr1* KO, n = 9 and 8, respectively; p = 0.026, M-W U test).

(K) The frequency of synchronous network events for Nkx2.1-INs was significantly lower in *Fmr1* KO mice. (0.32 ± 0.09 events per min for WT vs. 0.11 ± 0.04 for *Fmr1* KO, n = 9 WT and n = 8 *Fmr1* KO, p = 1.4 × 10^{-3}, M-W U test).

(L) The amplitude of calcium transient events of Nkx2.1-INs was not different between genotypes (15.5 ± 1.8 for WT vs. 16.2 ± 3.7 for *Fmr1* KO, p = 0.541, M-W U test). Error bars represent the standard error of the mean (SEM).

Please cite this article in press as: Kourdougli et al., Improvement of sensory deficits in fragile X mice by increasing cortical interneuron activity after the critical period, Neuron (2023), https://doi.org/10.1016/j.neuron.2023.06.009

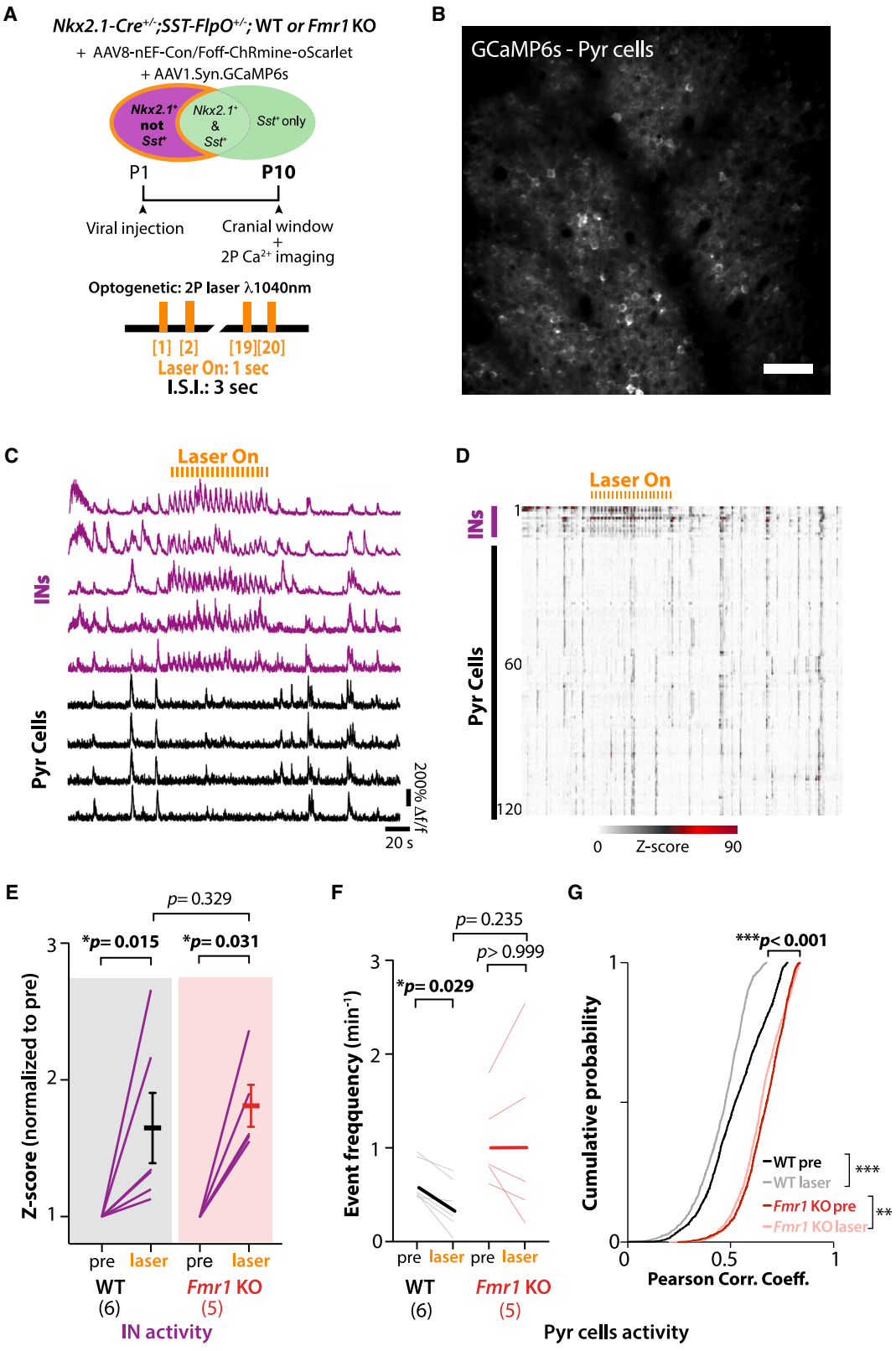

(legend on next page)

networks depends on the proper integration and function of GABAergic INs,[7,33] and co-activation of MGE-INs and Pyr cells during the first postnatal week is thought to restrict the spread of spontaneous synchronous network events.[32,34] However, although GABAergic perisomatic axons are observed in the first postnatal days, functional synaptic inhibition in S1 does not emerge until P8–P10.[35,36] Because fast-spiking INs in S1 of *Fmr1* KO mice seem significantly immature relative to those in WT controls,[15] we sought to determine whether or not Nkx2.1-INs in developing *Fmr1* KO mice are properly integrated into the S1 network. We used an all-optical two-photon optogenetic approach *in vivo*[37,38] to specifically increase the firing of putative future PV-INs within this population, since SST-INs are not hypoactive at P15 (Figure S2). Because SST-INs and PV-INs arise from a common MGE-derived precursor, they cannot be distinguished in Nkx2.1-Cre mice at P6. However, SST-INs begin to express SST before PV-INs express PVALB[21–23]; the SST mRNA is active even during embryonic development.[39] Thus, we used an intersectional genetic strategy[40] to optogenetically activate putative future PV-INs at P10 without activating SST-INs. We generated Nkx2.1-Cre;Sst-FlpO mice and injected rAAV8-nEF1-Con/Foff-ChRmine-oScarlet into S1 at P1 (Figure 2A), allowing the expression of ChRmine exclusively in Nkx2.1-Cre$^+$/Sst-FlpO$^-$ cells (Figures S3A–S3D). This allowed us to record from INs and Pyr cells simultaneously at P10 while we delivered pulses of laser light (1-s pulses at 1,040 nm every 3 s) (Figures 2C and 2D; Video S1). Although laser stimulation significantly drove the activity of Nkx2.1$^+$;Sst$^-$-INs in both WT and *Fmr1* KO mice (Figure 2E), it only reduced Pyr cell activity in WT mice, as manifested by a lower frequency of their synchronous events (Figure 2F), as well as a lower proportion of active cells per event (Figure S3E). Laser stimulation also significantly decorrelated activity in both WT mice and *Fmr1* KO mice, but the magnitude of the effect was negligible in the latter (Figures 2G and S3F). There was no effect on network activity in control mice that did not express ChRmine (Figure S3G). Incidentally, L2/3 Pyr cell activity at P10 was hypersynchronous in *Fmr1* KO mice (Figures 2G, S3F, and S4), as previously reported.[19,27] Taken together, these optogenetic results show that putative future PV-INs in *Fmr1* KO mice at P10 are functionally decoupled from Pyr cells and fail to properly modulate network activity.

What are the consequences of having Nkx2.1-INs that are hypoactive and largely decoupled from Pyr cells during neonatal cortical development? It is known that a wave of programmed cell death affects MGE-INs from ~P5 to P10 in mice,[41] which is regulated by cortical network activity.[32,42] Decreasing or increasing the activity of INs in the neonatal period results in lower or higher density of INs in juvenile mice, respectively.[43,44] We considered the possibility that the significant hypoactivity of Nkx2.1-INs in *Fmr1* KO mice might lead to their excessive cell death and, eventually, a reduced density of PV-INs. Previous reports of reduced PV-IN density in adult S1 and primary auditory cortex of *Fmr1* KO mice had used PVALB immunoreactivity.[45,46] However, because PVALB expression correlates with PV-IN activity levels,[47] we chose instead to quantify their density in PV-Cre;tdTom mice (see STAR Methods). We found a drastic reduction in the density of PV-Cre;tdTom$^+$ in *Fmr1* KO mice at P15 throughout the cortex (Figure S5A), including a 65% reduction in S1 across all layers (Figures 3A and 3B). A significant reduction in PV-IN density was also observed in the S1 of 9- and 10-month-old *Fmr1* KO mice (Figures S5B and S5C), suggesting that their loss is permanent. Interestingly, the density of SST- and calretinin-INs was higher, whereas calbindin-IN density was similar in adult *Fmr1* KO mice (Figures S6A–S6G), consistent with the large overlap between these two IN subclasses.[48]

To determine whether this phenotype is perhaps unique to *Fmr1* KO mice, we also quantified the density of three major types of INs in human autopsy material from adult FXS cases and age-matched neurotypical (NT) controls (n = 8 each) using immunohistochemistry (see STAR Methods). Remarkably, we found that the density of PVALB-expressing INs in Brodmann area 3 (equivalent to S1 in mice) was significantly lower (by 42%) in FXS cases compared with NT controls (Figures 3C and 3D). In contrast, the density of calretinin-expressing and calbindin-expressing IN subclasses was not different between FXS cases and NT controls (Figures S6H and S6I). This suggests that PV-IN density in S1 is similarly reduced in both *Fmr1* KO mice and humans with FXS.

We also observed a reduced density of Nkx2.1-Cre;tdTom$^+$ cells in *Fmr1* KO mice at both P6 and P10 (Figure 3E), but not at P1, suggesting that the lower density of PV-INs is not caused by reduced migration and/or neurogenesis of MGE-INs. Next, we quantified the expression of the cell death marker cleaved caspase-3 within Nkx2.1Cre;tdTom$^+$-INs and found an increased density of apoptotic MGE-INs at P6 in *Fmr1* KO mice (Figures S7A and S7B). To further confirm that loss of

Figure 2. Nkx2.1-INs form a weak functional network with Pyr cells in neonatal *Fmr1* KO mice

(A) Experimental design for optogenetic experiments.

(B) Example field of view of Pyr cells expressing GCaMP6s in Nkx2.1-Cre;SST-FlpO mice at P10.

(C) Representative calcium traces for 5 presumed Nkx2.1$^+$/Sst$^-$-INs (magenta) and 4 Pyr cells (black).

(D) Raster plot of neuronal activity in a representative WT mouse.

(E) Mean *Z* score of activity in Nkx2.1$^+$/SST$^-$-INs before (pre) and during optogenetic stimulation (laser). Each line represents an individual mouse (mean normalized *Z* score increased by 63.7% ± 25.5% for WT, p = 0.015, and 79.9% ± 15.3%, p = 0.031, for *Fmr1* KO mice upon laser-on stimulation; Wilcoxon matched-pairs signed rank test; n = 6 and 5, respectively).

(F) Mean frequency of Pyr cell calcium transients was significantly lower during optogenetic stimulation in WT mice but was unchanged in *Fmr1* KO mice. (0.63 ± 0.09 events per min pre vs. 0.38 ± 0.11 with laser; p = 0.029 in WT; 1.06 ± 0.21 events per min pre vs. 1.06 ± 0.43 with laser for *Fmr1* KO, p > 0.99; two-way ANOVA, post hoc Tukey).

(G) Pairwise correlation coefficients of Pyr cells were significantly modulated by optogenetic stimulation in both WT and *Fmr1* KO mice but the magnitude of the effect was greater in WT (mean correlation coefficient WT: 0.52 ± 0.004 for pre vs. 0.45 ± 0.004 for laser; p = 2.2 × 10^{-16}; *Fmr1* KO: 0.66 ± 0.002 for pre vs. 0.64 ± 0.003 for laser, p = 3.3 × 10^{-9}; and p < 0.001 for WT pre vs. *Fmr1* KO pre; Kolmogorov-Smirnov test).

Error bars represent SEM.

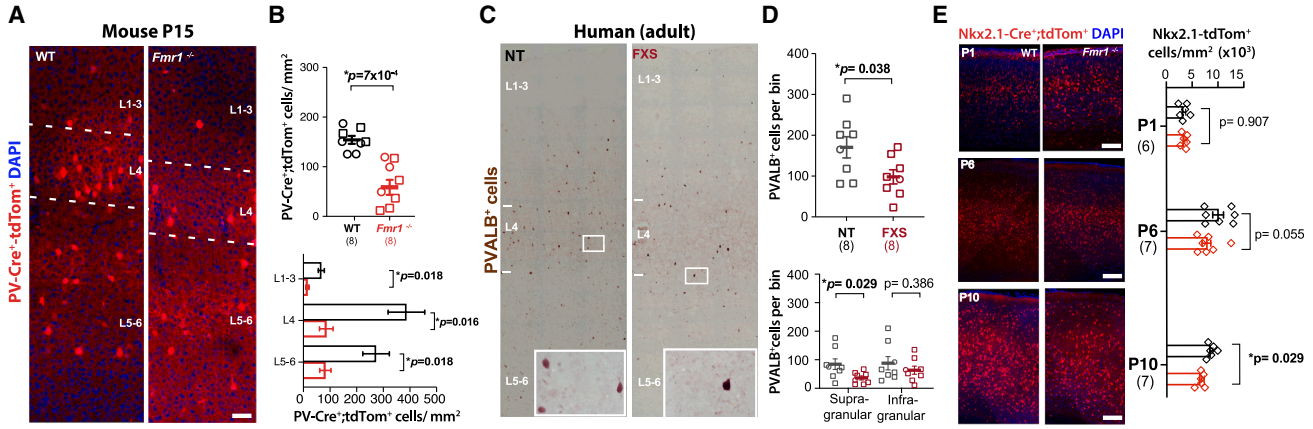

Figure 3. Reduced density of PV-INs and their MGE-derived precursors in mice and humans with FXS

(A) Example images from coronal sections through barrel field of S1 cortex (S1BF) from *PV*-Cre;tdTom mice at P15. (DAPI in blue.) Scale bars, 50 μm.

(B) Mean density of *PV*-tdTom$^+$ INs is significantly lower in *Fmr1* KO mice overall (top) and across cortical layers (bottom). Sample size in parenthesis, diamonds indicate the sex was not recorded. (Total density: 154.1 ± 8.0 cells per mm^2 for WT vs. 58.5 ± 15.1 for *Fmr1* KO; n = 9 and n = 8, respectively; p = 0.0007, unpaired t test; L2/3: 56.1 ± 9.4 vs. 12.7 ± 4.5, p = 0.018; L4: 322.0 ± 57.4 vs. 71.7 ± 21.1, p = 0.016; L5/6: 227.3 ± 41.5 vs. 68.7, p = 0.018 two-way ANOVA with post hoc Holm-Sidak test.)

(C) Example images from coronal sections through BA3 from neurotypical (NT) and FXS human tissue.

(D) Mean density of PVALB$^+$ cells in BA3 is significantly lower in FXS cases overall (top) and in supragranular cortical layers (bottom) (170.6 ± 26.0 PVALB$^+$ cells per bin for NT vs. 98.1 ± 17.4 for FXS cases, n = 8 cases each; p = 0.038, unpaired t test; supragranular layer: 83.6 ± 18.6 for neurotypical vs. 35.5 ± 7.0, p = 0.0294; infragranular: 87.0 ± 23.2 vs. 62.6 ± 14.3, p = 0.386, unpaired t test). See also Table S1.

(E) Coronal sections through S1 showing Nkx2.1-Cre;tdTom$^+$ INs (red) in WT and *Fmr1* KO mice at P1 and P10 (DAPI: blue). Scale bars, 100 μm.

(F) Mean density of Nkx2.1;tdTom$^+$ INs is lower in *Fmr1* KO mice at P6 and P10, but not at P1. (P1: 3,408 ± 354 cells/mm^2 for WT vs. 3,472 ± 548 for *Fmr1* KO, p = 0.907; P6: 10,200 ± 1,027 cells/mm^2 for WT vs. 8,035 ± 860 for *Fmr1* KO, p = 0.056; P10: 8,633 ± 318 for WT vs. 6,650 ± 279 for *Fmr1* KO, p = 0.029; n = 6 per genotype at P1 and P10, n = 7 at P6, two-way ANOVA with post hoc Holm-Sidak).

Error bars represent SEM.

MGE-INs was due to apoptosis, we performed longitudinal *in vivo* imaging of Nkx2.1-Cre;tdTom$^+$ IN at P6 and P7 in *Fmr1* KO mice. We found several examples of pyknotic Nkx2.1-Cre;tdTom$^+$ INs and evidence that they disappeared within the short interval between imaging sessions (Figure S7C). Considering findings from previous developmental studies[32,42] and the fact that MGE-INs complete their migration by the end of the first postnatal week,[49] our data suggest that the reduced density of Nkx2.1-INs at P6–P10 is due to apoptosis and that those cells are irreversibly lost (Figure S7D).

Activating of Nkx2.1-INs in neonatal *Fmr1* KO mice partially rescues PV cell density

Our findings thus far are consistent with a model in which hypoactivity of the Nkx2.1-IN population and their uncoupling from Pyr cells in neonatal *Fmr1* KO mice result in excess developmental cell death of future PV-INs.[42] We reasoned that artificially increasing the activity of Nkx2.1-INs during the apoptosis window (P5–P10) in *Fmr1* KO mice might rescue the density of PV-INs and other circuit phenotypes.[20] To test this, we used designer receptors exclusively activated by designer drugs (DREADDs) and injected rAAV5-DIO-hM3Dq-mCherry (or a rAAV5-DIO-mCherry control virus) in Nkx2.1-Cre;*Fmr1* KO mice at P1 (Figure 4A) and performed immunohistochemistry for PVALB at P15 (Figure 4B). This virus approach led to only a small proportion (25%) of PVALB$^+$ cells expressing the Gq-DREADD (Figures S8A and S8B). Next, we administered a DREADD agonist, compound 21 (C21; 1 mg/kg s.c., twice daily), from P5 to P9 (Figure 4A).[50] We found that the density of PVALB-expressing INs in L2/3 of *Fmr1* KO;hM3Dq mice at P15 was fully restored to WT levels but remained significantly below WT levels in *Fmr1* KO;mCherry controls treated with C21 (Figures 4B and 4C). The effect of DREADDs on PVALB density was less pronounced in deeper layers (Figure S8C). The fact that increasing MGE-IN activity can prevent their death in *Fmr1* KO mice further confirms our theory that many MGE-INs eventually die because of their hypoactivity.

Neonatal chemogenetic activation of Nkx2.1-INs partially rescues the global cortical transcriptome but further derails the Nkx2.1-specific translatome

Having restored the density of PV-INs to WT levels by boosting Nkx2.1-IN activity with Gq-DREADDS in neonatal *Fmr1* KO mice, we hypothesized that this strategy might have been sufficient to restore the developmental trajectory of the entire local cortical circuit. To test this, we first investigated transcriptional differences in S1 between WT and *Fmr1* KO mice and whether expressing Gq-DREADDs in Nkx2.1-INs might reduce those differences. Previous studies in *Fmr1* KO mice had shown that loss of fragile X messenger ribonucleoprotein (FMRP), which is a translational suppressor of key proteins involved in brain maturation and plasticity,[51–53] causes transcriptional dysregulation in the adult hippocampus and cerebellum.[54–56] However, to date, there are no mRNA sequencing (RNA-seq) studies specific to MGE-INs in the neocortex during early postnatal development. Moreover, neuronal activity is known to regulate multiple aspects of IN

Please cite this article in press as: Kourdougli et al., Improvement of sensory deficits in fragile X mice by increasing cortical interneuron activity after the critical period, Neuron (2023), https://doi.org/10.1016/j.neuron.2023.06.009

CellPress
OPEN ACCESS

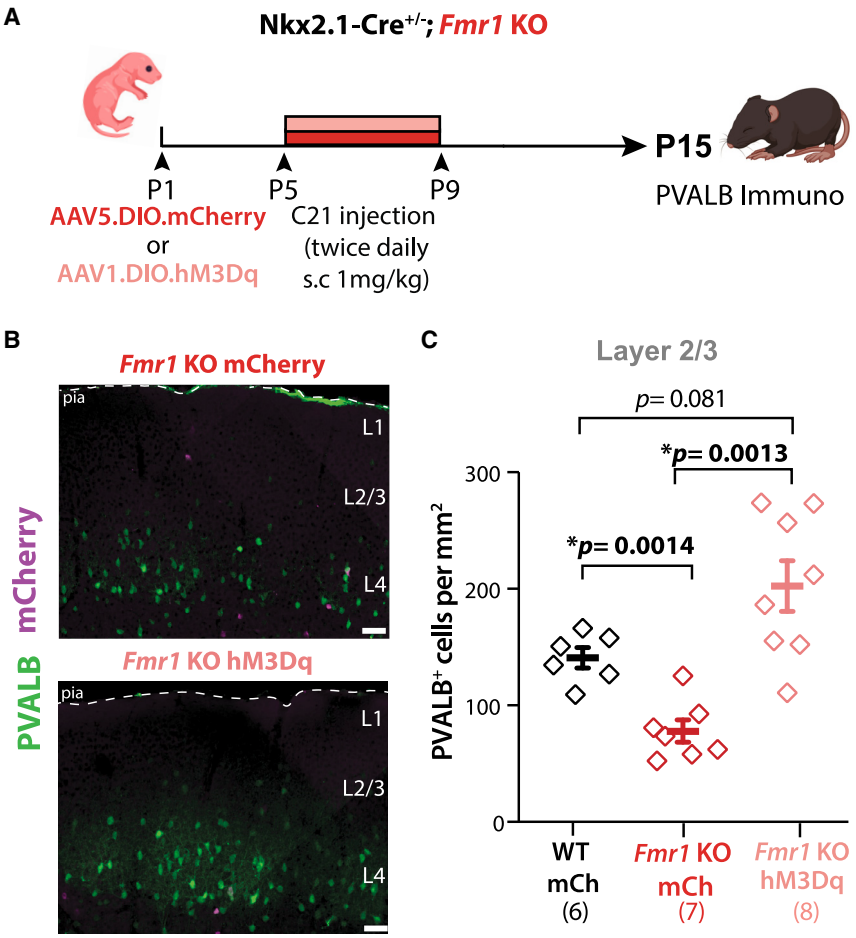

Figure 4. Chronic chemogenetic activation of Nkx2.1-INs in S1 restores PV-IN density in L2/3 of neonatal *Fmr1* KO mice

(A) Experimental design for chronic chemogenetic activation of Nkx2.1-INs in *Fmr1* KO mice.

(B) Representative images of PVALB immunostaining. Scale bars, 50 μm.

(C) Quantification of total PVALB$^+$ cell density at P15 in S1BF. (141 ± 8.6, 80.6 ± 10.8, and 202.6 ± 21.7 cells/mm^2, n = 6, 7, and 8, respectively, two-way ANOVA with post hoc Holm-Sidak).

Error bars represent SEM.

development, including their transcriptional program.[33,57–59] Thus, the changes in the activity of both MGE-INs and Pyr cells of neonatal *Fmr1* KO mice (Figures 1 and 2) are likely to impact transcription both globally in the cortex but also specifically within Nkx2.1-INs. Comparing the S1 cortical transcriptome of WT and *Fmr1* KO mice at P15 would also help us uncover potential molecular mechanisms underlying MGE-IN hypofunction.

We used a RiboTag RNA-seq approach,[60] which allowed us to assess both the global transcriptome in S1 and the Nkx2.1-IN-specific translatome (see STAR Methods).[61] First, we generated Nkx2.1-Cre;Rpl22$^{HA/-}$ (WT or *Fmr1* KO) triple transgenic mice and virally expressed hM3Dq (or mCherry) in Nkx2.1-INs from P1 onward (Figures 5A and 5B). We identified 2,898 differentially expressed (DE) genes in the bulk RNA samples (before RiboTag pull-down) of *Fmr1* KO;mCherry mice (n = 8 mice) compared with WT;mCherry mice (n = 7 mice; Figure 5C). Gene ontology (GO) analysis (see STAR Methods) revealed enrichment in genes involved in "synapse organization" and "neuronal apoptosis," among other categories (Figure 5D). Notably, we found that several MGE-INs expressing genes (or transcription factors)[59,62,63] were significantly downregulated in *Fmr1* KO mice, including several PV-enriched genes (e.g., *Pvalb*, *Bcan*, *Syt2*, and *Kcnab3*), whereas other MGE-IN genes were upregulated, including some SST-enriched genes (*Sst* and *Pcdh18*) (Figure S9A).

We also compared the DE genes from the bulk transcriptome of P15 *Fmr1* KO-mCherry mice with a list of genes that are bound to FMRP (presumably regulated by it) in developing or adult mice.[64,65] Strikingly, 266 of the DE genes were known FMRP targets (Figure 5E), which implies that in the absence of FMRP, its own mRNA targets are transcriptionally dysregulated from early developmental stages. Furthermore, our list of DE genes from the bulk cortical transcriptome also partially overlaps with the previously published lists of DE genes in the hippocampus and cerebellum of adult *Fmr1* KO mice (Figure S9B).[54,55]

We next analyzed the Nkx2.1-specific translatome (RiboTag "pull-down") and identified 2,039 DE genes in *Fmr1* KO;mCherry mice, including downregulated *Pvalb*, *Pink1*, and *Gabra2* (Figure 5F). GO analysis revealed an enrichment of upregulated genes in "synapse organization," "axonogenesis," and "neural migration" and downregulated genes in "lipid metabolism" and "neuron proliferation/morphogenesis" (Figure 5G). Furthermore, we found several "neuronal apoptosis" DE genes in the Nkx2.1 translatome (Figure S10B), which may relate to the excess death of MGE-INs (Figures 3 and S7). Additionally, 279 of the DE genes in the Nkx2.1 translatome are FMRP targets (Figure 5H), and most of these (242/279) are upregulated in *Fmr1* KO mice. This again highlights the fact that loss of FMRP has hitherto unrecognized consequences on Nkx2.1-IN gene expression that are already apparent at 2 weeks of age.

Our principal goal had been to determine whether a DREADD-mediated boost of Nkx2.1-IN firing in *Fmr1* KO mice might reduce their dysregulated gene expression (as an indication that it could restore their identity and function). We first compared the DE genes from the bulk transcriptome of *Fmr1* KO;hM3Dq mice (n = 7 mice) treated with C21 from P5 to P9 with those of similarly treated *Fmr1* KO;mCherry controls (n = 8 mice) and found 15% fewer DE genes (2,463 vs. 2,898; Figures 6A–6C and 6F). Although our chemogenetic intervention targeted INs, DE genes associated with excitatory neurons showed surprisingly more improvement in expression than those of inhibitory neurons (Figure 6D). The expression of several

Please cite this article in press as: Kourdougli et al., Improvement of sensory deficits in fragile X mice by increasing cortical interneuron activity after the critical period, Neuron (2023), https://doi.org/10.1016/j.neuron.2023.06.009

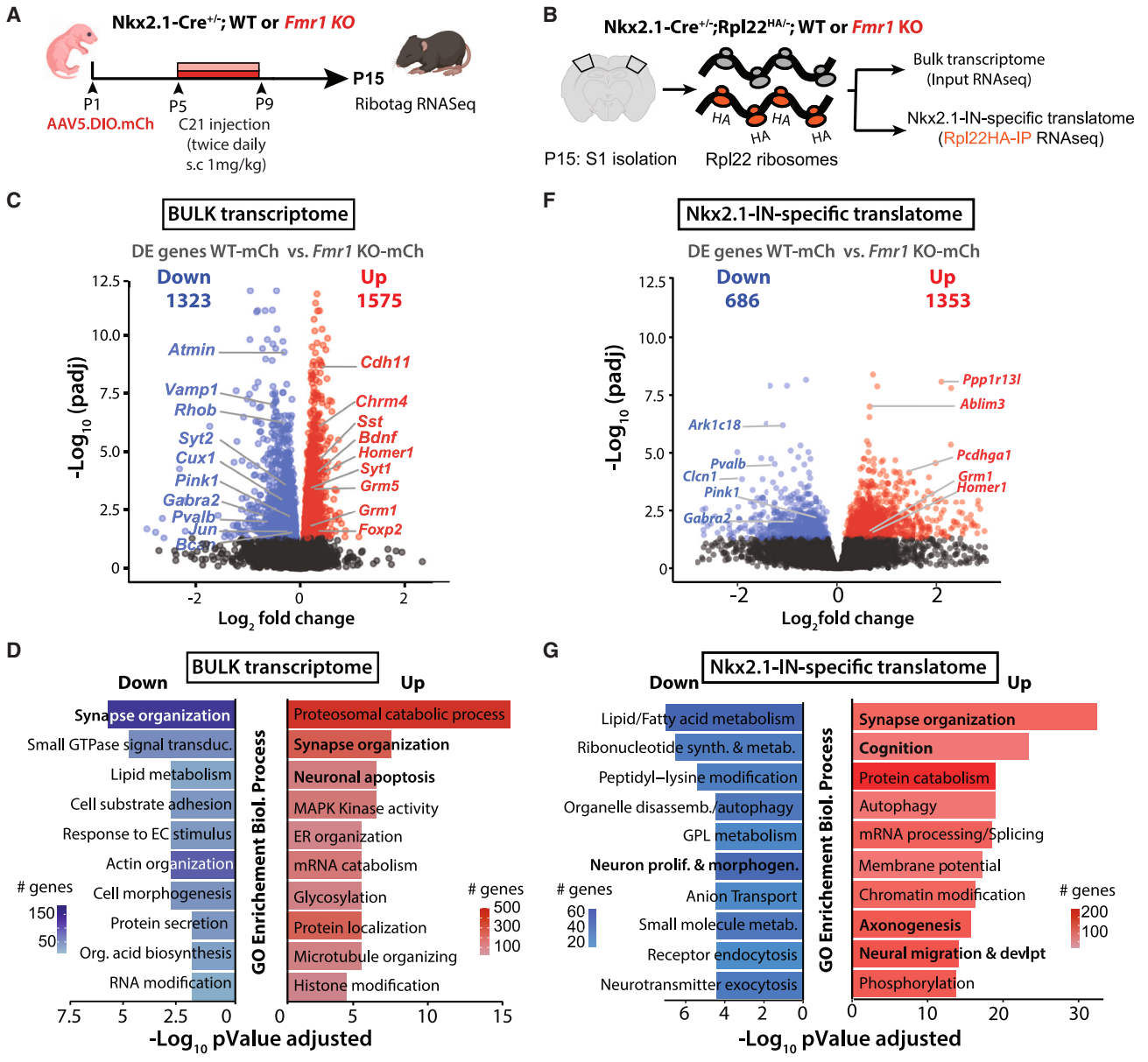

(legend on next page)

genes enriched in MGE-INs was restored to WT levels, including genes expressed in basket and chandelier cells (*Pvalb*, *Kcnn2*, *Wasf3*, and *Sox11*) as well as SST-INs (*Cnst*) (Figures 6E, 6H, and S9A). DE genes in the bulk transcriptome whose expression was rescued by Gq-DREADDs belonged primarily to "synapse organization" and "neuronal apoptosis" categories (Figures S9C, S10A, and S10B).

When we turned to the Nkx2.1-specific translatome, we found a dramatic and unexpected increase in the number of DE genes (6,105) in chemogenetically treated *Fmr1* KO-hM3Dq mice compared with WT controls (Figures 6B and 6G). Although some GO analysis categories were improved in *Fmr1* KO;hM3Dq mice (Figure S9E), many others were newly dysregulated. Moreover, within the Nkx2.1-IN translatome, the chemogenetic intervention had only a modest effect on DE genes associated with MGE-INs (Figure 6I).

In summary, our RiboTag RNA-seq approach uncovered previously unknown dysregulation in the neocortical transcriptome and Nkx2.1-specific translatome of *Fmr1* KO mice at a very early stage of development. Chronically increasing the activity of Nkx2.1-INs in *Fmr1* KO mice from P5 to P9 modestly restored the global cortical transcriptome while further derailing the translatome of Nkx2.1-INs.

Post-critical-period, but not neonatal, chemogenetic activation of Nkx2.1-INs partially rescues S1 circuit deficits in *Fmr1* KO mice

We next tested whether the same neonatal DREADD manipulation of Nkx2.1-INs could restore circuit changes in *Fmr1* KO mice. We focused on two robust S1 phenotypes we previously reported in *Fmr1* KO mice at P15, namely the low percentage of whisker-responsive Pyr cells in L2/3 and their lack of adaptation to repetitive whisker stimulation.[20] Once again, we virally expressed hM3Dq (or mCherry) in *Fmr1* KO mice and administered C21 from P5 to P9. We then implanted cranial windows (and injected rAAV1-Syn-GCaMP6s) at P15 and performed *in vivo* calcium imaging of Pyr cells at P21 (Figures 7A and 7B). This neonatal DREADD activation of Nkx2.1-INs did not significantly change the proportion of whisker-responsive Pyr neurons, nor their adaptation to repetitive whisker stimulation in *Fmr1* KO mice (Figures 7C and 7D). We hypothesized that this failure to restore Pyr cell responsivity and adaptation was due to the fact that immature Nkx2.1-INs are decoupled from Pyr cells (Figures 2 and S3). To further test this theory, we used the same hM3Dq-DREADD approach in a different group of *Fmr1* KO mice (n = 4) but acutely administered C21 at P10 to activate Nkx2.1-INs and monitored with calcium imaging the activity of both Nkx2.1-INs and Pyr cells (Figures S11A and S11B; Video S2). We discovered that C21 could reliably increase the activity of Nkx2.1-INs (Figure S11C), but it failed to suppress Pyr cell firing in *Fmr1* KO mice (Figure S11D). Not surprisingly, when we administered C21 chronically from P5 to P9 in a separate cohort of *Fmr1* KO mice (n = 4) and recorded Pyr cell activity at P10, we found that it did not change the synchronous network events (Figures S11E and S11F). Thus, activating Nkx2.1-INs neonatally fails to modulate sensory-evoked activity in *Fmr1* KO mice because MGE-INs are not yet functionally connected with Pyr cells before P10.

Several aspects of cortical maturation are known to be transiently delayed in *Fmr1* KO mice but eventually catch up to WT levels.[19,66,67] We wondered whether the coupling of Nkx2.1-INs (or eventually PV-INs) to Pyr cells is similarly delayed in *in vivo* in *Fmr1* KO mice and therefore tested whether PV-INs might be able to modulate Pyr cell activity in L2/3 of S1 by the end of the second postnatal week. We first used an acute chemogenetic approach to transiently increase PV-IN activity by expressing hM3Dq (or mCherry) and GCaMP6s at P10 in PV-Cre;*Fmr1* KO mice and then recorded from L2/3 Pyr neurons *in vivo* at P15, before and 30–40 min after administering a single dose of C21 (1 mg/kg s.c.) (Figure S12A). Compared with vehicle injection, acute C21 injection resulted in a significant reduction of spontaneous activity of Pyr cells in *Fmr1* KO mice expressing hM3Dq (n = 10), but not in mCherry controls (n = 6) (Figure S12B). We also repeated the all-optical approach with ChRmine optogenetics in Nkx2.1-Cre;Sst-FlpO;*Fmr1* KO mice at P15 (n = 3) and discovered that, unlike at P10, optogenetic activation of putative future PV-INs significantly reduced Pyr cell activity (Figures S12C–S12F). As expected, no effect was observed in mCherry-expressing controls (n = 2).

Knowing that PV-INs are capable of modulating Pyr cells in *Fmr1* KO mice by P15, we tested the effect of chronic chemogenetic activation of Nkx2.1-INs from P15 to P20 on S1 circuit deficits (Figure 7E). Post-critical period DREADD activation of Nkx2.1-INs significantly increased the proportion of whisker-responsive neurons (Figure 7F) and modestly increased their adaptation to repetitive whisker stimulation, although this did not reach significance (Figure 7G). Similarly, using an acute chemogenetic approach at P15 but targeting PV-INs (instead of Nkx2.1-INs) in PV-Cre;*Fmr1* KO mice at P15, we observed that a single dose of C21 also caused a significant increase in the percentage of whisker-responsive Pyr cells in the hM3Dq group compared with vehicle injection, but no change

Figure 5. Bulk transcriptome and Nkx2.1-IN-specific translatome are altered in P15 *Fmr1* KO mice

(A) Experimental design for transcriptomic analysis at P15.

(B) Cartoon of RiboTag approach for RNA-seq in S1 at P15.

(C) Volcano plot of differentially expressed (DE) genes in the bulk RNA of *Fmr1* KO-mCherry mice (n = 8) compared with WT-mCherry mice (n = 7).

(D) Top 10 "GO terms" of the bulk transcriptome in *Fmr1* KO-mCherry mice using the biological process package (see STAR Methods).

(E) Number of DE genes in *Fmr1* KO-mCherry mice within the bulk transcriptome dataset that are known targets of FMRP, based on previously published database (see STAR Methods). Heatmaps represent the changes of expression as *Z* scores among the top 25 upregulated and downregulated genes.

(F) Volcano plot of DE genes in the Nkx2.1-IN-specific translatome of *Fmr1* KO-mCherry mice (n = 8) compared to WT-mCherry control (n = 3).

(G) Top 10 GO terms in Nkx2.1-IN-specific translatome in *Fmr1* KO-mCherry mice.

(H) Number of DE genes in *Fmr1* KO-mCherry mice within the Nkx2.1-specific translatome dataset that are known targets of FMRP (shown as in E).

Error bars represent SEM.

Please cite this article in press as: Kourdougli et al., Improvement of sensory deficits in fragile X mice by increasing cortical interneuron activity after the critical period, Neuron (2023), https://doi.org/10.1016/j.neuron.2023.06.009

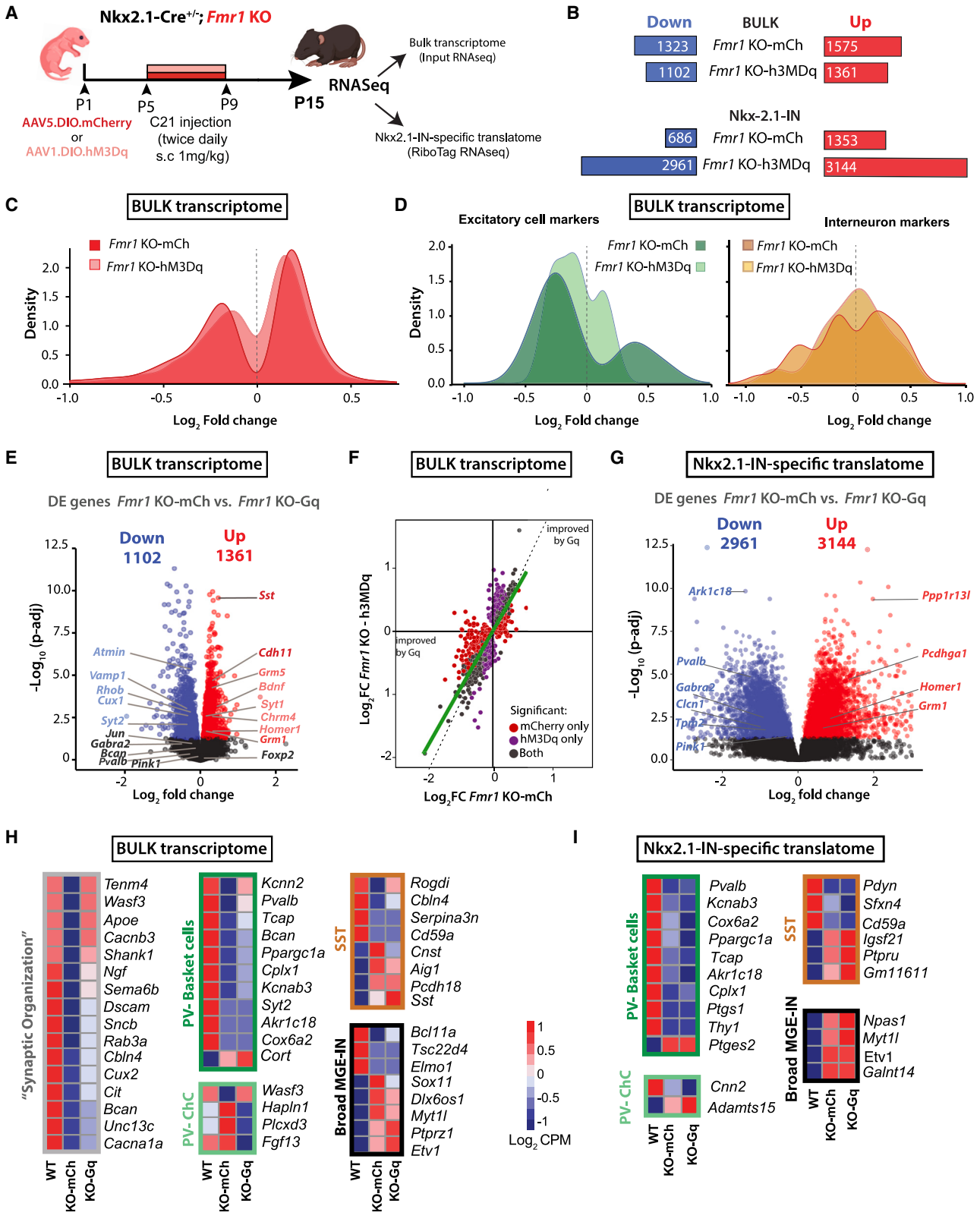

(legend on next page)

Please cite this article in press as: Kourdougli et al., Improvement of sensory deficits in fragile X mice by increasing cortical interneuron activity after the critical period, Neuron (2023), https://doi.org/10.1016/j.neuron.2023.06.009

to their adaptation (Figures S12G–S12I). Altogether, these results suggest that by the end of second postnatal week, putative future PV-INs within the Nkx2.1 population in *Fmr1* KO mice are finally functionally integrated into S1 and that boosting their firing at this age (but not earlier) can lessen whisker-evoked circuit deficits.

Boosting PV-IN activity using a Kv3.1 modulator ameliorates S1 circuit deficits and tactile defensiveness in juvenile *Fmr1* KO mice

Our chronic chemogenetic activation of Nkx2.1-INs from P15 to P20 only partially restored S1 circuit dysfunction in *Fmr1* KO mice. One possibility is that because the local viral injection only infects a subset of our targeted neurons (Figures S8A and S8B), we could not drive the activity of a sufficient number of Nkx2.1-INs with DREADDs. We therefore tested a chronic pharmacologic approach to achieve a more global and longer-lasting increase of PV cell activity in *Fmr1* KO mice after the critical period. After ~P10, cortical PV-INs assume their fast-spiking characteristics due to their expression of Kv3.1b channels. This subclass of voltage-gated potassium channels, responsible for rapid repolarization that enables their fast-spiking behavior, is almost exclusively expressed in PV-INs.[68,69] We reasoned that targeting Kv3.1b channels pharmacologically could be used to modulate the firing of PV-INs as a potential treatment for FXS. We used the compound AG00563 (1-(4-methylbenzene-1-sulfonyl)-N-[(1,3-oxazol-2-yl)methyl]-1H-pyrrole-3-carboxamide), a Kv3.1-positive allosteric modulator (Figure 8A). Patch-clamp recordings of identified PV-INs in acute slices from P14 to P16 PV-Cre;tdTom;*Fmr1* KO mice (see STAR Methods) showed that bath application of AG00563 (10 μM) significantly increased their excitability (Figures 8B and 8C). Of note, AG000563 did not affect the membrane potential or excitability of Pyr cells nor the input resistance of PV-INs or Pyr cells (Figures S13A–S13E).

Using *in vivo* calcium imaging, we found that acute administration of AG00563 (3 mg/kg s.c.) at P15 significantly increased the fraction of whisker-responsive Pyr cells but did not change their adaptation index (Figures S13F–S13H), which matches our results with acute excitatory DREADDs in PV-INs (Figures S12G–S12I). We next administered AG00563 (or vehicle) chronically (3 mg/kg s.c., twice daily) to *Fmr1* KO mice from P15 to P20 and then performed calcium imaging the following day (Figures 8D and 8E). We found that when compared with vehicle controls (n = 11 mice), the proportion of whisker-responsive Pyr cells in S1 was significantly higher in AG00563-treated mice (n = 13 mice) (Figure 8F), reaching near WT levels.[20] Moreover, the adaptation index of Pyr cells was also significantly increased by AG00563 (Figure 8G).

The absence of neuronal adaptation in certain brain circuits is one potential reason why children with NDDs/autism exhibit sensory hypersensitivity: they are unable to "tune out" non-threatening or non-salient stimuli.[70] We used a tactile defensiveness assay based on repetitive whisker stimulation[20] (see STAR Methods and Figure 8H) to test whether AG006563 might lessen the maladaptive avoidance/defensive behaviors previously observed in *Fmr1* KO mice. We found that mice chronically treated with AG00563 from P15 to P20 manifested significantly less grabbing of the stimulator than vehicle-treated *Fmr1* KO controls, and they also spent more time demonstrating healthy adaptive behaviors, such as grooming (Figure 8I). Overall, more AG00563-treated juvenile *Fmr1* KO mice displayed grooming and fewer showed grabbing during whisker stimulation, whereas the opposite was true in vehicle-treated *Fmr1* KO mice (Figure S13I). To determine whether this pharmacologic approach could also be beneficial in older animals, we also treated young adult *Fmr1* KO mice with AG00563 (from P45 to P50) and found a significant reduction in the proportion of time spent grabbing the stimulator (Figure 8J). Therefore, chronic pharmacological activation of PV-INs any time after P15 can ameliorate S1 sensory circuit deficits and rescue behavioral manifestations of tactile defensiveness in *Fmr1* KO mice.

DISCUSSION

We set out to identify when IN hypofunction first begins in *Fmr1* KO mice to better understand how developmental trajectories of cortical circuits are changed in FXS and in other NDDs that share a cortical IN hypofunction phenotype.[4] We used an intersectional strategy to express chemo- and opto-genetic tools to manipulate Nkx2.1-INs, as well as *in vivo* calcium imaging to record

Figure 6. Neonatal chemogenetic activation of Nkx2.1-INs partially rescues the bulk S1 transcriptome but further derails the Nkx2.1-IN translatome

(A) Experimental design for chronic chemogenetic activation of Nkx2.1-INs (from P5 to P9) in *Fmr1* KO mice and RNA-seq at P15.

(B) Top: the total number of downregulated and upregulated genes in the bulk transcriptome was 15% smaller in *Fmr1* KO-hM3Dq mice than in *Fmr1* KO-mCherry. Bottom: the total number of downregulated and upregulated genes in the translatome.

(C) Density plot showing how the DREADD manipulation led to fewer DE genes in the *Fmr1* KO-hM3Dq group compared with WT mice.

(D) Density plot showing how the DREADD manipulation affected expression of genes specific to excitatory cells (left) or interneurons (right). Note that fewer genes are different from WT mice in the *Fmr1* KO-hM3Dq group, particularly for excitatory cell markers.

(E) Volcano plot of DE genes in the bulk RNA of *Fmr1* KO-hM3Dq mice (n = 7) compared to WT-mCherry controls (n = 8). DE genes that had been labeled in Figure 5C and were fully or partially corrected by the DREADD manipulation are shown in charcoal or lighter color font, respectively.

(F) Correlation plot of genes affected in the *Fmr1* KO-mCherry and *Fmr1* KO-hM3Dq. Red and purple dots denote DE genes that are uniquely and significantly different from WT controls in *Fmr1* KO-mCherry and *Fmr1* KO-hM3Dq mice, respectively. Gray dots are shared DE genes in both groups (unaffected by DREADDs), whereas purple genes are less different from WT than red genes.

(G) Volcano plot of DE genes in the Nkx2.1-IN-specific translatome of *Fmr1* KO-mCherry mice (n = 8) compared to WT-mCherry controls (n = 3).

(H) Representative examples of how DREADDs affected genes for the "synaptic organization" GO term (gray), or different subclasses of MGE-INs. Scale bar represents the $\log_2$ CPMs (count per millions).

(I) List of DE genes associated with different subclasses of MGE-INs for which expression was changed by DREADDs (same groups as in H).

Error bars represent SEM.

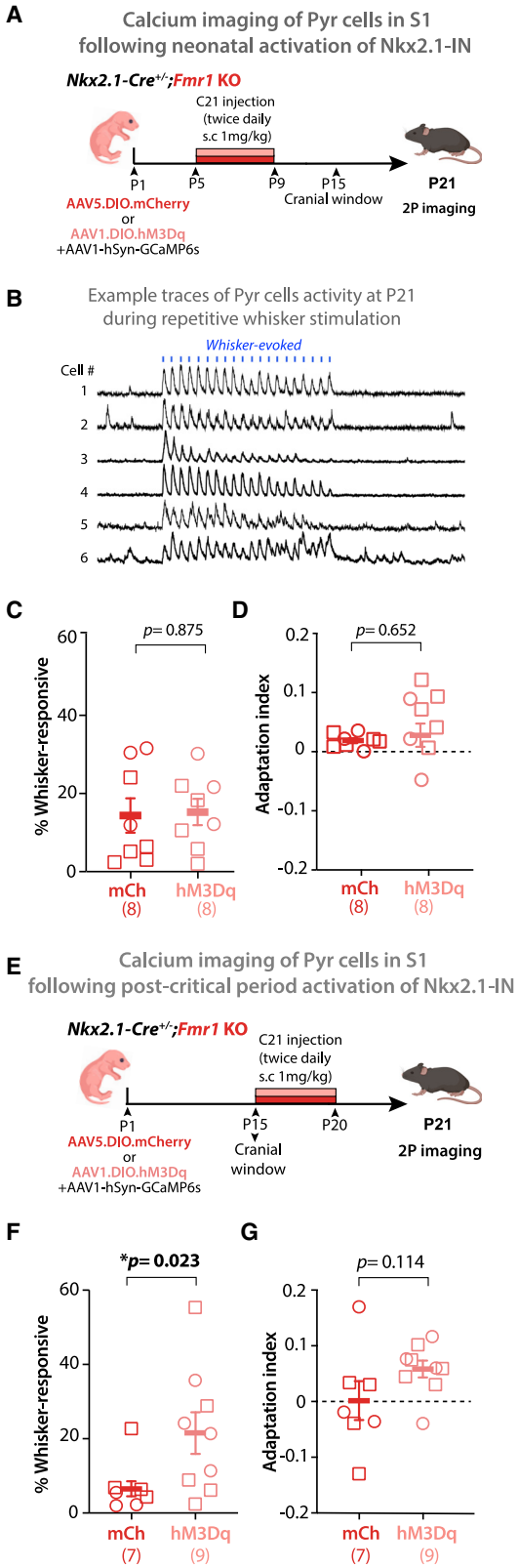

Figure 7. Post-critical period but not neonatal chronic chemogenetic activation of Nkx2.1-INs improves S1 circuit deficits

(A) Experimental design for chronic chemogenetic activation of Nkx2.1-INs in neonatal *Fmr1* KO mice from P5 to P9 and for assessing circuit function using *in vivo* two-photon calcium imaging at P21.

(B) Example traces of L2/3 Pyr cell calcium transients in a *Fmr1* KO mouse. Whisker stimulation (1 s at 10 Hz, 3 s I.S.I., blue bars).

(C) The proportion of whisker-responsive Pyr cells was not changed by DREADDs in *Fmr1* KO mice. (14.4% ± 4.4% vs. 15.3% ± 3.3%, p = 0.875, unpaired t test).

(D) The neuronal adaptation index of Pyr cells to repetitive whisker stimulation was not changed by chemogenetics (0.02 ± 0.004 for *Fmr1* KO mCherry vs. 0.03 ± 0.01 for *Fmr1* KO; p = 0.652, unpaired t test).

(E) Experimental design for chronic chemogenetic activation of Nkx2.1-INs in juvenile (post-critical period) *Fmr1* KO mice.

(F) The proportion of whisker-responsive Pyr cells was significantly changed by DREADDs in *Fmr1* KO mice. (6.5% ± 2.7% vs. 21.6% ± 6.4%, p = 0.0229, M-W U test).

(G) The neuronal adaptation index of Pyr cells to repetitive whisker stimulation was ~340% higher in the *Fmr1* KO-hM3Dq group compared to *Fmr1* KO-mCherry controls, though the difference was not significant (0.0016 ± 0.03 for *Fmr1* KO-mCherry vs. 0.058 ± 0.015 for *Fmr1* KO; p = 0.114, M-W U test). Error bars represent SEM.

from them and their excitatory Pyr cell partners. We discovered the following: (1) PV-INs and their immature precursors from the MGE in *Fmr1* KO mice are hypoactive as early as P6 and their density is reduced in both mice and humans with FXS because of an excess of developmental apoptosis. (2) The bulk S1 cortical transcriptome and the MGE IN-specific translatome are drastically changed in *Fmr1* KO mice at the closure of the S1 critical period. (3) Increasing the activity of MGE-INs during the apoptosis window (P5–P10) restores the density of PV-INs and a subset of DE cortical genes but fails to rescue circuit dynamics because MGE-INs are decoupled from Pyr cells at that stage. (4) In contrast, boosting PV-IN activity after the S1 critical period (P15–P20) does restore network activity in S1, especially when using a Kv3.1 allosteric modulator, which also ameliorates tactile defensiveness in *Fmr1* KO mice.

Critical developmental role of Nkx2.1-INs in sensory circuits in FXS

GABAergic INs govern crucial steps in the maturation of brain circuits and have been hypothesized to play a key role in NDDs.[4,5] We confirm previous observations that, during the early postnatal period, spontaneous Pyr cell activity is hypersynchronous in *Fmr1* KO mice.[19,27] Additionally, we now demonstrate that Nkx2.1-INs are hypoactive in neonatal *Fmr1* KO mice during a time that coincides with the emergence of perisomatic GABAergic inhibition onto Pyr cells.[36] Considering the emerging knowledge about IN-Pyr connectivity in neonatal cortex,[22,71] this hypoactivity likely has drastic consequences for both structural and functional connectivity[72] and sensory processing. Inhibition is likely necessary for the desynchronization of network activity at around P12.[30] Indeed, our all-optical two-photon optogenetic approach demonstrated that activation of Nkx2.1-INs can drive the decorrelation of Pyr cells in WT mice at P10 (Figure 2F). The previously reported developmental delay in this desynchronization in *Fmr1* KO mice[19,27] is probably due to the fact that Nkx2.1-INs are hypoactive and functionally decoupled from Pyr cells. Thus, early

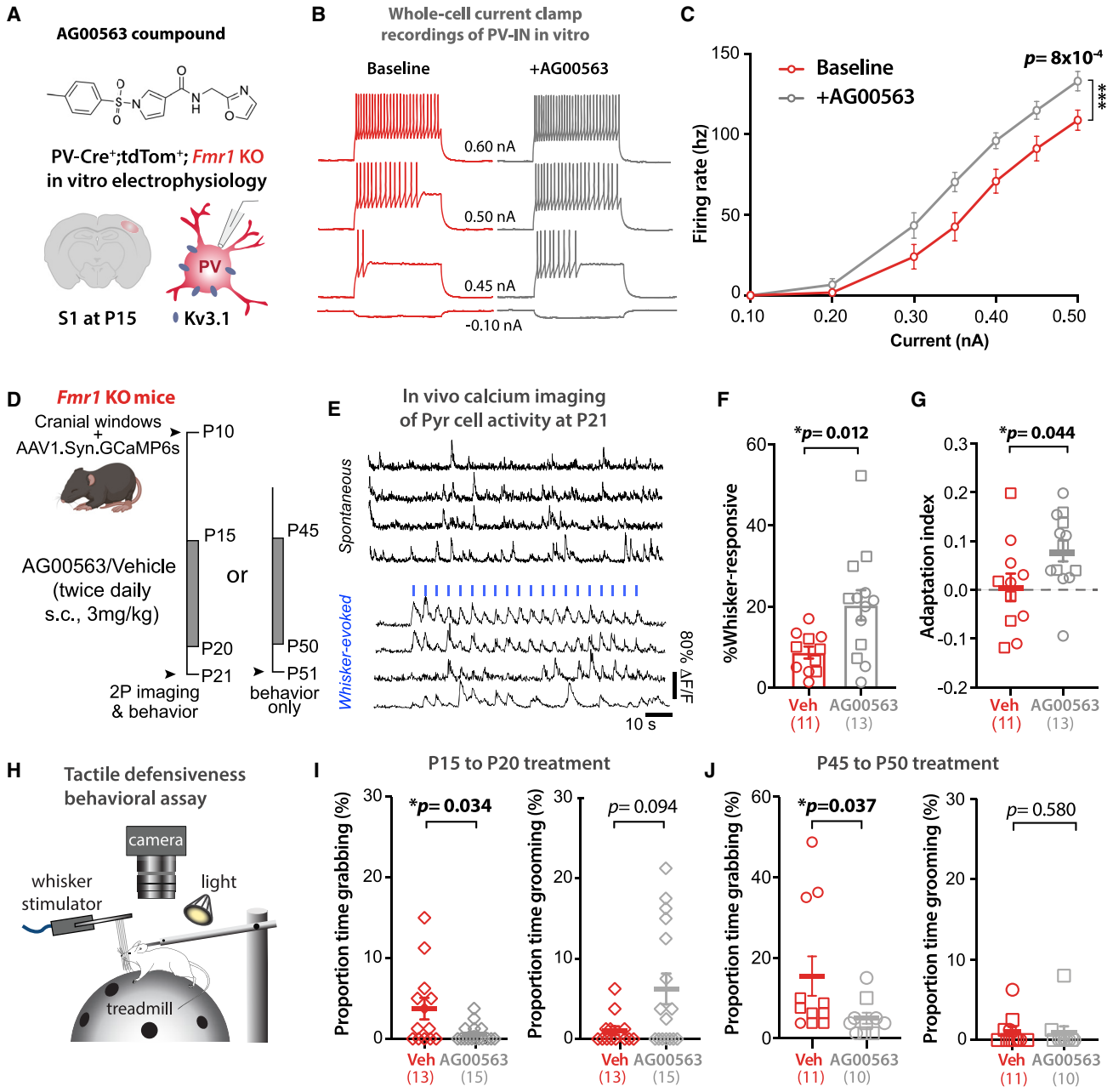

Figure 8. A Kv3.1 allosteric modulator, AG00563, ameliorates circuit function and tactile defensiveness in juvenile and young adult *Fmr1* KO mice

(A) Chemical structure of the AG00563 compound and experimental design for the *in vitro* patch-clamp recordings of PV-INs.

(B) Example traces of action potential trains evoked by 250 ms current injection in a PV-Cre-tdTom^{+} cell in S1 from a *Fmr1* KO mouse at P15.

(C) Cumulative input-output curves during baseline (red) or AG00563 (gray) (n = 15 cells from 6 PV-Cre;tdTom;*Fmr1* KO mice, two-way RM ANOVA).

(D) Experimental design for chronic AG00563 vs. vehicle treatment (3 mg/kg s.c., twice daily) from P15 to P20 or P45 to P50 in *Fmr1* KO mice.

(E) Example traces of L2/3 Pyr cell calcium transients in *Fmr1* KO mouse. Whisker stimulation (1 s at 10 Hz, 3 s I.S.I., blue bars).

(F) The percentage of whisker-responsive Pyr cells was significantly higher in *Fmr1* KO mice treated with AG00563 than in vehicle controls. (20.3% ± 3.7% vs. 8.7% ± 1.5%, p = 0.012; unpaired t test, n = 13 and 11 mice, respectively).

(G) The adaptation index of Pyr cells was also significantly higher in *Fmr1* KO mice treated with AG00563-compared with vehicle controls. (0.08 ± 0.03 vs. 0.01 ± 0.03; p = 0.0438; unpaired t test).

(H) Cartoon of tactile defensiveness behavioral assay.

(legend continued on next page)

changes in cortical connectivity could have profound effects on the developmental trajectory of PV-INs.

Our RiboTag RNA-seq reveals that several PV-IN genes are dysregulated in *Fmr1* KO mice at P15, which is consistent with prior studies showing developmental delays in the maturation of the intrinsic properties and morphogenesis of fast-spiking INs,[15] as well as their excitatory inputs.[17,18] Our new data suggest that the developmental trajectory of cortical INs in FXS begins to deviate very early in development, when highly synchronous neural activity dominates in the neocortex, a stage that roughly corresponds to the late 3rd trimester of gestation in humans.[73] Importantly, our results are not consistent with major disruptions in the generation or migration of MGE-INs.

Excess developmental death of PV-INs in FXS

There has been some controversy about whether the lower density of PV-INs reported in several models of NDDs/autism represents an artifact.[4] The argument is that those studies had relied on PVALB immunohistochemistry to identify PV-INs, and yet, PVALB expression levels are known to correlate with PV-IN activity[47]; therefore, low PV-IN density in autism models might just reflect their hypoactivity.[74] In the present study, we circumvent this potential confound in *Fmr1* KO mice by counting tdTom$^+$ cells in PV-Cre;Ai9 mice and confirm a marked reduction in PV-IN density. In some mice, only rare, scattered cortical PV-INs could be identified (Figure S5A; example 2). It may seem counterintuitive that PV-IN density in both WT and *Fmr1* KO mice was higher at 9 months of age than at P15 (Figures 3A, 3B, and S5B). Our results match those of several other studies that quantified PV-IN density using immunohistochemistry or *in situ* hybridization.[42,46,75–80] This is almost certainly due to the fact that, even by P15, not all future PV-INs have turned on the *Pvalb* promoter.

We also found strong evidence that Nkx2.1-INs succumb to programmed cell death (Figure S7). The increased density of SST-INs in *Fmr1* KO mice (Figure S6), and their higher thalamocortical afferent connectivity,[23] may represent compensatory phenomena for the loss of PV-INs (and their hypoactivity). It is possible that some MGE-INs that would have become PV-INs actually differentiated into SST-INs (Figure S7D).

We report, for the first time, that the density of PV-INs (but not calretinin- or calbindin-expressing INs) is also reduced in human FXS cases (Figures 3C and 3D). This apparent loss of PVALB$^+$ INs in human tissue could be a result of their hypoactivity or perhaps the unique vulnerability of these neurons to the postmortem delay in FXS. Still, the parallels between mouse and human data with regard to reduced PV-IN density remain striking. Interestingly, organoids derived from human induced pluripotent stem cells from patients with FXS had a lower density of GABAergic neurons,[81] which was felt to be due to reduced neurogenesis. Because we found a normal density of Nkx2.1-INs at P1 in *Fmr1* KO mice, we do not believe that the reduced PV-IN density is caused by differences in their birth or migration. Additional studies will be needed to confirm these results in a larger number of human cases and ideally with attempts to correlate age and symptom severity with PV-IN density in various brain regions.

Insights from RNA-seq studies in developing *Fmr1* KO mice

FMRP is an mRNA-binding protein that, in response to neuronal activity, negatively regulates the translation of many mRNAs that encode proteins important for neuronal development and synaptic function.[64,82] Our bulk RNA-seq dataset identified dozens of DE genes (including *Chrm4*, *Syt2*, and *Nedd4*) that had been previously found in RNA-seq screens from the hippocampus of adult *Fmr1* KO mice,[54,55] suggesting that the dysregulation of those genes is affected by loss of FMRP from early developmental stages. The relatively small overlap (72 DE genes) between our study and previous ones may be due to the differences in techniques, brain regions, or mouse age. Our RiboTag study is the first to show that loss of FMRP causes a profound dysregulation of the translatome of MGE-INs during development. This dataset will hopefully provide an opportunity for future comparisons of developmental RNA-seq datasets. Surprisingly, boosting the activity of Nkx2.1-INs, which significantly reduced their developmental apoptosis, did not reduce the number of MGE-IN-specific DE genes; in fact, it caused a massive dysregulation of their translatome. Perhaps this is a cautionary note that intervening at early stages of cortical development to modulate the activity of immature neurons could have unintended consequences. Thus, further investigations are needed to fully understand the effects of early developmental IN hypoactivity on gene expression, circuit plasticity, and sensory processing.

Why did chronic chemogenetic activation of Nkx2.1-INs at P5–P9 fail to fully rescue S1 circuit dynamics in *Fmr1* KO mice?

One of our most striking observations was that raising the excitability of INs in neonatal *Fmr1* KO mice was not sufficient to restore sensory-evoked network function in S1. Our data provide strong evidence that the reason is that MGE-INs are decoupled from their Pyr cell partners during neonatal development (Figure 2). This could reflect changes in INs themselves (e.g., a delay in synaptogenesis) or in post-synaptic Pyr cells (e.g., changes in post-synaptic GABA receptor expression). We also find that eventually, PV-IN → Pyr cell connectivity is established (Figure S12), which is consistent with the known delayed maturation PV-INs in *Fmr1* KO mice.[15,18] This likely explains why we could restore circuit dynamics in S1 and ameliorate sensory avoidance behaviors in *Fmr1* KO mice by boosting PV-IN firing after P15, but not earlier.

(I) Left: the proportion of time spent grabbing the stimulator was significantly lower in AG00563-treated mice than in vehicle controls (0.62% ± 0.28 s vs. 3.75% ± 1.33 s, p = 0.0343, M-W U test, n = 15 and 13 *Fmr1* KO mice, respectively). Right: the proportion of time spent grooming was higher in AG00563-treated group, but not significant (6.25% ± 1.9 s vs. 1.06% ± 0.53 s, p = 0.094, M-W U test).
(J) Left: the proportion of time spent grabbing the stimulator was significantly lower in AG00563-treated adult *Fmr1* KO mice than in vehicle controls (5.0% ± 1.38 s vs. 15.45% ± 4.9 s, p = 0.037, M-W U test, n = 10 and 11 mice, respectively). Right: the proportion of time spent grooming (1.02% ± 0.57 s vs. 0.92% ± 0.79 s, p = 0.58, M-W U test).
Error bars represent SEM.

Implications for the treatment of FXS

Because symptoms of NDDs are first recognized in toddlers, it is generally understood that they arise because of changes in the brain that likely occur *in utero*. This makes sense for FXS because expression of FMRP in the brain starts prenatally; hence, its absence could change the typical developmental trajectory of brain maturation in the third trimester of gestation or earlier. Therapeutic interventions for intellectual disability or autism that begin at the earliest stages of brain development should therefore be the most effective.[1,83] However, we found that increasing the activity of Nkx2.1-INs in neonatal mice did not fully rescue *Fmr1* KO circuit phenotypes in S1, whereas increasing PV-IN firing after P15 did and also mitigated tactile defensiveness. This offers hope in FXS because it means that interventions to boost IN activity need not start at birth (this may not be in fact desirable) but could be efficacious if started in childhood, adolescence, or even adulthood.[14] Atypical sensory perception is present in toddlers with FXS and other NDDs and is believed to contribute to social communication differences, repetitive behaviors, and learning disability in adulthood.[1,84] Our encouraging preclinical results with the Kv3.1 activator AG00563 suggest that increasing activity of PV-INs is a plausible strategy to lessen certain symptoms in children and adults with NDDs.

STAR★METHODS

Detailed methods are provided in the online version of this paper and include the following:

- KEY RESOURCES TABLE
- RESOURCE AVAILABILITY
  - Lead contact
  - Materials availability
  - Data and code availability
- EXPERIMENTAL MODEL AND STUDY PARTICIPANT DETAILS
  - Mice lines
  - Study participant details
- METHOD DETAILS
  - Viral injections
  - Cranial windows
  - Intrinsic signal imaging
  - *In vivo* two-photon (2P) calcium imaging in head-restrained mice
  - *In vivo* two-photon optogenetic stimulation
  - Nkx2.1-Cre-specific RiboTag RNA extraction and sequencing
  - Data analysis for calcium imaging
  - Brain slice electrophysiology
  - Immunohistochemistry and IN quantification in mouse tissue
  - Histology and IN quantification in human tissue
  - DREADD agonist (C21) administration *in vivo*
  - AG00563 treatment *in vivo*
  - Tactile defensiveness assay in head-restrained mice
- QUANTIFICATION AND STATISTICAL ANALYSIS

SUPPLEMENTAL INFORMATION

Supplemental information can be found online at https://doi.org/10.1016/j.neuron.2023.06.009.

ACKNOWLEDGMENTS

The authors thank Anis Contractor and Aaron McGee for feedback on the manuscript and Fuying Gao and Riki Kawaguchi from the bioinformatics core at UCLA. This work was supported by the following grants: R01NS117597 (NIH-NINDS); R01HD054453 (NIH-NICHD); Department of Defense (DOD) 13196175; 5P50HD055784 for the UCLA Center for Autism Research and Treatment Pilot program from the Semel Institute at UCLA (NIH and the UCLA Clinical and Translational Science Institute Pilot Grant program), awarded to C.P.-C.; R01NS116589 (NIH-NINDS), awarded to D.V.B.; R01MH094681 (NIH-NIMH), awarded to V.M.-C.; and a grant from the FRAXA foundation, awarded to N.K.

AUTHOR CONTRIBUTIONS

Conceptualization, N.K., C.P.-C., and V.M.-C. for the human studies; D.V.B. and B.L. for the *in vitro* recordings; and N.K., C.P.-C., A.G.S., C.M., and B.H. for the AG00563 experiments. Methodology, N.K., C.P.-C., A.S., D.V.B., and M.J.G.; investigation, N.K., A.S., B.L., A.L., D.T.C., and P.J.; N.K. and C.P.-C. wrote the manuscript with input from other authors.

DECLARATION OF INTERESTS

A.G.S., C.M., and B.J.H. are employees of H. Lundbeck A/S, who developed the AG00563 compound. A patent was filled by H. Lundbeck A/S (WO 2020/089262).

INCLUSION AND DIVERSITY

We support inclusive, diverse, and equitable conduct of research.

Received: May 9, 2022
Revised: April 14, 2023
Accepted: June 16, 2023
Published: July 13, 2023

REFERENCES

1. Robertson, C.E., and Baron-Cohen, S. (2017). Sensory perception in autism. Nat. Rev. Neurosci. *18*, 671–684.
2. Rubenstein, J.L.R., and Merzenich, M.M. (2003). Model of autism: increased ratio of excitation/inhibition in key neural systems. Genes Brain Behav. *2*, 255–267. https://doi.org/10.1034/j.1601-183x.2003.00037.x.
3. Contractor, A., Klyachko, V.A., and Portera-Cailliau, C. (2015). Altered neuronal and circuit excitability in fragile X syndrome. Neuron *87*, 699–715.
4. Contractor, A., Ethell, I.M., and Portera-Cailliau, C. (2021). Cortical interneurons in autism. Nat. Neurosci. *24*, 1648–1659. https://doi.org/10.1038/s41593-021-00967-6.
5. Marín, O. (2016). Developmental timing and critical windows for the treatment of psychiatric disorders. Nat. Med. *22*, 1229–1238. https://doi.org/10.1038/nm.4225.
6. Dorrn, A.L., Yuan, K., Barker, A.J., Schreiner, C.E., and Froemke, R.C. (2010). Developmental sensory experience balances cortical excitation and inhibition. Nature *465*, 932–936. https://doi.org/10.1038/nature09119.
7. Fishell, G., and Kepecs, A. (2020). Interneuron types as attractors and controllers. Annu. Rev. Neurosci. *43*, 1–30. https://doi.org/10.1146/annurev-neuro-070918-050421.

8. Wamsley, B., and Fishell, G. (2017). Genetic and activity-dependent mechanisms underlying interneuron diversity. Nat. Rev. Neurosci. *18*, 299–309. https://doi.org/10.1038/nrn.2017.30.

9. Salazar, R.F., Bertollini, C., Mutel, S., Roo, M., and Muller, D. (2018). Restoring wild-type-like CA1 network dynamics and behavior during adulthood in a mouse model of schizophrenia. Nat. Neurosci. *21*, 1–14. https://doi.org/10.1038/s41593-018-0225-y.

10. Chen, Q., Deister, C.A., Gao, X., Guo, B., Lynn-Jones, T., Chen, N., Wells, M.F., Liu, R., Goard, M.J., Feng, S., et al. (2020). Dysfunction of cortical GABAergic neurons leads to sensory hyper-reactivity in a Shank3 mouse model of ASD. Nat. Neurosci. *23*, 1–18. https://doi.org/10.1038/s41593-020-0598-6.

11. Marín, O. (2012). Interneuron dysfunction in psychiatric disorders. Nat. Rev. Neurosci. *13*, 107–120. https://doi.org/10.1038/nrn3155.

12. Rifé, M., Badenas, C., Mallolas, J., Jiménez, L., Cervera, R., Maya, A., Glover, G., Rivera, F., and Milà, M. (2003). Incidence of fragile X in 5,000 consecutive newborn males. Genet. Test. *7*, 339–343. https://doi.org/10.1089/109065703322783725.

13. Antoine, M.W., Langberg, T., Schnepel, P., and Feldman, D.E. (2019). Increased excitation-inhibition ratio stabilizes synapse and circuit excitability in four autism mouse models. Neuron *101*, 648–661.e4. https://doi.org/10.1016/j.neuron.2018.12.026.

14. Goel, A., Cantu, D.A., Guilfoyle, J., Chaudhari, G.R., Newadkar, A., Todisco, B., Alba, D., Kourdougli, N., Schmitt, L.M., Pedapati, E., et al. (2018). Impaired perceptual learning in a mouse model of fragile X syndrome is mediated by parvalbumin neuron dysfunction and is reversible. Nat. Neurosci. *21*, 1–14. https://doi.org/10.1038/s41593-018-0231-0.

15. Nomura, T., Musial, T.F., Marshall, J.J., Zhu, Y., Remmers, C.L., Xu, J., and Nicholson, D.A. (2017). Delayed maturation of fast-spiking interneurons is rectified by activation of the TrkB receptor in the mouse model of fragile X syndrome. J. Neurosci. *37*. 2893-2816. https://doi.org/10.1523/jneurosci.2893-16.2017.

16. Berzhanskaya, J., Phillips, M.A., Shen, J., and Colonnese, M.T. (2017). Sensory hypo-excitability in a rat model of fetal development in fragile X syndrome. Nature *6*, 1–12. https://doi.org/10.1038/srep30769.

17. Gibson, J.R., Bartley, A.F., Hays, S.A., and Huber, K.M. (2008). Imbalance of neocortical excitation and inhibition and altered UP states reflect network hyperexcitability in the mouse model of fragile X syndrome. J. Neurophysiol. *100*, 2615–2626. https://doi.org/10.1152/jn.90752.2008.

18. Domanski, A.P.F., Booker, S.A., Wyllie, D.J.A., Isaac, J.T.R., and Kind, P.C. (2019). Cellular and synaptic phenotypes lead to disrupted information processing in Fmr1-KO mouse layer 4 barrel cortex. Nat. Commun. *10*, 4814. https://doi.org/10.1038/s41467-019-12736-y.

19. Gonçalves, J.T., Anstey, J.E., Golshani, P., and Portera-Cailliau, C. (2013). Circuit level defects in the developing neocortex of fragile X mice. Nat. Neurosci. *16*, 903–909. https://doi.org/10.1038/nn.3415.

20. He, C.X., Cantu, D.A., Mantri, S.S., Zeiger, W.A., Goel, A., and Portera-Cailliau, C. (2017). Tactile defensiveness and impaired adaptation of neuronal activity in the Fmr1 knock-out mouse model of autism. J. Neurosci. *37*, 6475–6487. https://doi.org/10.1523/JNEUROSCI.0651-17.2017.

21. Tuncdemir, S.N., Wamsley, B., Stam, F.J., Osakada, F., Goulding, M., Callaway, E.M., Rudy, B., and Fishell, G. (2016). Early somatostatin interneuron connectivity mediates the maturation of deep layer cortical circuits. Neuron *89*, 521–535. https://doi.org/10.1016/j.neuron.2015.11.020.

22. Marques-Smith, A., Lyngholm, D., Kaufmann, A.-K., Stacey, J.A., Hoerder-Suabedissen, A., Becker, E.B.E., Wilson, M.C., Molnár, Z., and Butt, S.J. (2016). A transient translaminar GABAergic interneuron circuit connects thalamocortical recipient layers in neonatal somatosensory cortex. Neuron *89*, 536–549. https://doi.org/10.1016/j.neuron.2016.01.015.

23. Pouchelon, G., Dwivedi, D., Bollmann, Y., Agba, C.K., Xu, Q., Mirow, A.M.C., Kim, S., Qiu, Y., Sevier, E., Ritola, K.D., et al. (2021). The organization and development of cortical interneuron presynaptic circuits are area specific. Cell Rep. *37*, 109993. https://doi.org/10.1016/j.celrep.2021.109993.

24. Mòdol, L., Bollmann, Y., Tressard, T., Baude, A., Che, A., Duan, Z.R.S., Babij, R., De Marco García, N.V.D.M., and Cossart, R. (2020). Assemblies of perisomatic GABAergic neurons in the developing barrel cortex. Neuron *105*, 93–105.e4. https://doi.org/10.1016/j.neuron.2019.10.007.

25. Stern, E.A., Maravall, M., and Svoboda, K. (2001). Rapid development and plasticity of layer 2/3 maps in rat barrel cortex in vivo. Neuron *31*, 305–315. https://doi.org/10.1016/s0896-6273(01)00360-9.

26. La Fata, G.L., Gärtner, A., Domínguez-Iturza, N., Dresselaers, T., Dawitz, J., Poorthuis, R.B., Averna, M., Himmelreich, U., Meredith, R.M., Achsel, T., et al. (2014). FMRP regulates multipolar to bipolar transition affecting neuronal migration and cortical circuitry. Nat. Neurosci. *17*, 1693–1700. https://doi.org/10.1038/nn.3870.

27. Cheyne, J.E., Zabouri, N., Baddeley, D., and Lohmann, C. (2019). Spontaneous activity patterns are altered in the developing visual cortex of the Fmr1 knockout mouse. Front. Neural Circuits *13*, 57. https://doi.org/10.3389/fncir.2019.00057.

28. de Lecea, L., del Río, J.A., and Soriano, E. (1995). Developmental expression of parvalbumin mRNA in the cerebral cortex and hippocampus of the rat. Brain Res. Mol. Brain Res. *32*, 1–13. https://doi.org/10.1016/0169-328x(95)00056-x.

29. Butt, S.J.B., Sousa, V.H., Fuccillo, M.V., Hjerling-Leffler, J., Miyoshi, G., Kimura, S., and Fishell, G. (2008). The requirement of Nkx2-1 in the temporal specification of cortical interneuron subtypes. Neuron *59*, 722–732. https://doi.org/10.1016/j.neuron.2008.07.031.

30. Rochefort, N.L., Garaschuk, O., Milos, R.-I., Narushima, M., Marandi, N., Pichler, B., Kovalchuk, Y., and Konnerth, A. (2009). Sparsification of neuronal activity in the visual cortex at eye-opening. Proc. Natl. Acad. Sci. USA *106*, 15049–15054. https://doi.org/10.1073/pnas.0907660106.

31. Golshani, P., Gonçalves, J.T., Khoshkhoo, S., Mostany, R., Smirnakis, S., and Portera-Cailliau, C. (2009). Internally mediated developmental desynchronization of neocortical network activity. J. Neurosci. *29*, 10890–10899. https://doi.org/10.1523/JNEUROSCI.2012-09.2009.

32. Duan, Z.R.S., Che, A., Chu, P., Mòdol, L., Bollmann, Y., Babij, R., Fetcho, R.N., Otsuka, T., Fuccillo, M.V., Liston, C., et al. (2020). GABAergic restriction of network dynamics regulates interneuron survival in the developing cortex. Neuron *105*, 75–92.e5. https://doi.org/10.1016/j.neuron.2019.10.008.

33. De Marco García, N.V.D.M., Karayannis, T., and Fishell, G. (2011). Neuronal activity is required for the development of specific cortical interneuron subtypes. Nature *472*, 351–355. https://doi.org/10.1038/nature09865.

34. Leighton, A.H., Cheyne, J.E., Houwen, G.J., Maldonado, P.P., De Winter, F.D., Levelt, C.N., and Lohmann, C. (2021). Somatostatin interneurons restrict cell recruitment to retinally driven spontaneous activity in the developing cortex. Cell Rep. *36*, 109316. https://doi.org/10.1016/j.celrep.2021.109316.

35. Favuzzi, E., Marques-Smith, A., Deogracias, R., Winterflood, C.M., Sánchez-Aguilera, A., Maeso, P., Fernandes, C., and Ewers, H. (2017). Activity-dependent gating of parvalbumin interneuron function by the perineuronal net protein brevican. Neuron *95*, 639–655.e10. https://doi.org/10.1016/j.neuron.2017.06.028.

36. Gour, A., Boergens, K.M., Heike, N., Hua, Y., Laserstein, P., Song, K., and Helmstaedter, M. (2021). Postnatal connectomic development of inhibition in mouse barrel cortex. Science *371*, eabb4534. https://doi.org/10.1126/science.abb4534.

37. Rickgauer, J.P., Deisseroth, K., and Tank, D.W. (2014). Simultaneous cellular-resolution optical perturbation and imaging of place cell firing fields. Nat. Neurosci. *17*, 1816–1824. https://doi.org/10.1038/nn.3866.

38. Packer, A.M., Russell, L.E., Dalgleish, H.W.P., and Häusser, M. (2015). Simultaneous all-optical manipulation and recording of neural circuit

activity with cellular resolution in vivo. Nat. Meth. *12*, 140–146. https://doi.org/10.1038/nmeth.3217.

39. Lim, L., Pakan, J.M.P., Selten, M.M., Marques-Smith, A., Llorca, A., Bae, S.E., Rochefort, N.L., and Marín, O. (2018). Optimization of interneuron function by direct coupling of cell migration and axonal targeting. Nat. Neurosci. *21*, 920–931. https://doi.org/10.1038/s41593-018-0162-9.
40. Fenno, L.E., Ramakrishnan, C., Kim, Y.S., Evans, K.E., Lo, M., Vesuna, S., Inoue, M., Cheung, K.Y.M., Yuen, E., Pichamoorthy, N., et al. (2020). Comprehensive dual- and triple-feature intersectional single-vector delivery of diverse functional payloads to cells of behaving mammals. Neuron *107*, 836–853.e11. https://doi.org/10.1016/j.neuron.2020.06.003.
41. Southwell, D.G., Paredes, M.F., Galvao, R.P., Jones, D.L., Froemke, R.C., Sebe, J.Y., Alfaro-Cervello, C., Tang, Y., Garcia-Verdugo, J.M., Rubenstein, J.L., et al. (2012). Intrinsically determined cell death of developing cortical interneurons. Nature *491*, 109–113. https://doi.org/10.1038/nature11523.
42. Wong, F.K., Bercsenyi, K., Sreenivasan, V., Portalés, A., Fernández-Otero, M., and Marín, O. (2018). Pyramidal cell regulation of interneuron survival sculpts cortical networks. Nature *557*, 668–673. https://doi.org/10.1038/s41586-018-0139-6.
43. Priya, R., Paredes, M.F., Karayannis, T., Yusuf, N., Liu, X., Jaglin, X., Graef, I., Alvarez-Buylla, A., and Fishell, G. (2018). Activity regulates cell death within cortical interneurons through a calcineurin-dependent mechanism. Cell Rep. *22*, 1695–1709. https://doi.org/10.1016/j.celrep.2018.01.007.
44. Denaxa, M., Neves, G., Rabinowitz, A., Kemlo, S., Liodis, P., Burrone, J., and Pachnis, V. (2018). Modulation of apoptosis controls inhibitory interneuron number in the cortex. Cell Rep. *22*, 1710–1721. https://doi.org/10.1016/j.celrep.2018.01.064.
45. Selby, L., Zhang, C., and Sun, Q.-Q. (2007). Major defects in neocortical GABAergic inhibitory circuits in mice lacking the fragile X mental retardation protein. Neurosci. Lett. *412*, 227–232. https://doi.org/10.1016/j.neulet.2006.11.062.
46. Wen, T.H., Afroz, S., Reinhard, S.M., Palacios, A.R., Tapia, K., Binder, D.K., Razak, K.A., and Ethell, I.M. (2018). Genetic reduction of matrix metalloproteinase-9 promotes formation of perineuronal nets around parvalbumin-expressing interneurons and normalizes auditory cortex responses in developing Fmr1 knock-out mice. Cereb. Cortex *28*, 3951–3964. https://doi.org/10.1093/cercor/bhx258.
47. Donato, F., Rompani, S.B., and Caroni, P. (2013). Parvalbumin-expressing basket-cell network plasticity induced by experience regulates adult learning. Nature *504*, 272–276. https://doi.org/10.1038/nature12866.
48. Rudy, B., Fishell, G., Lee, S., and Hjerling-Leffler, J. (2011). Three groups of interneurons account for nearly 100% of neocortical GABAergic neurons. Dev. Neurobiol. *71*, 45–61. https://doi.org/10.1002/dneu.20853.
49. Bortone, D., and Polleux, F. (2009). KCC2 expression promotes the termination of cortical interneuron migration in a voltage-sensitive calcium-dependent manner. Neuron *62*, 53–71. https://doi.org/10.1016/j.neuron.2009.01.034.
50. Thompson, K.J., Khajehali, E., Bradley, S.J., Navarrete, J.S., Huang, X.P., Slocum, S., Jin, J., Liu, J., Xiong, Y., Olsen, R.H.J., et al. (2018). DREADD Agonist 21 is an effective agonist for muscarinic-based DREADDs in vitro and in vivo. ACS Pharmacol. Transl. Sci. *1*, 61–72. https://doi.org/10.1021/acsptsci.8b00012.
51. Darnell, J.C., and Klann, E. (2013). The translation of translational control by FMRP: therapeutic targets for FXS. Nat. Neurosci. *16*, 1530–1536. https://doi.org/10.1038/nn.3379.
52. Miyashiro, K.Y., Beckel-Mitchener, A., Purk, T.P., Becker, K.G., Barret, T., Liu, L., Carbonetto, S., Weiler, I.J., Greenough, W.T., and Eberwine, J. (2003). RNA cargoes associating with FMRP reveal deficits in cellular functioning in Fmr1 null mice. Neuron *37*, 417–431. https://doi.org/10.1016/s0896-6273(03)00034-5.
53. Das Sharma, S.D., Metz, J.B., Li, H., Hobson, B.D., Hornstein, N., Sulzer, D., Tang, G., and Sims, P.A. (2019). Widespread alterations in translation elongation in the brain of juvenile Fmr1 knockout mice. Cell Rep. *26*, 3313–3322.e5. https://doi.org/10.1016/j.celrep.2019.02.086.
54. Thomson, S.R., Seo, S.S., Barnes, S.A., Louros, S.R., Muscas, M., Dando, O., Kirby, C., Wyllie, D.J.A., Hardingham, G.E., Kind, P.C., et al. (2017). Cell-type-specific translation profiling reveals a novel strategy for treating fragile X syndrome. Neuron *95*, 550–563.e5. https://doi.org/10.1016/j.neuron.2017.07.013.
55. Sawicka, K., Hale, C.R., Park, C.Y., Fak, J.J., Gresack, J.E., Van Driesche, S.J.V., Kang, J.J., Darnell, J.C., and Darnell, R.B. (2019). FMRP has a cell-type-specific role in CA1 pyramidal neurons to regulate autism-related transcripts and circadian memory. eLife *8*, e46919. https://doi.org/10.7554/eLife.46919.
56. Ceolin, L., Bouquier, N., Vitre-Boubaker, J., Rialle, S., Severac, D., Valjent, E., Perroy, J., and Puighermanal, E. (2017). Cell type-specific mRNA dysregulation in hippocampal CA1 pyramidal neurons of the fragile X syndrome mouse model. Front. Mol. Neurosci. *10*, 340. https://doi.org/10.3389/fnmol.2017.00340.
57. Chattopadhyaya, B., Di Cristo, G.D., Higashiyama, H., Knott, G.W., Kuhlman, S.J., Welker, E., and Huang, Z.J. (2004). Experience and activity-dependent maturation of perisomatic GABAergic innervation in primary visual cortex during a postnatal critical period. J. Neurosci. *24*, 9598–9611. https://doi.org/10.1523/JNEUROSCI.1851-04.2004.
58. Dehorter, N., Ciceri, G., Bartolini, G., Lim, L., del Pino, I., and Marín, O. (2015). Tuning of fast-spiking interneuron properties by an activity-dependent transcriptional switch. Science *349*, 1216–1220. https://doi.org/10.1126/science.aab3415.
59. Mahadevan, V., Mitra, A., Zhang, Y., Yuan, X., Peltekian, A., Chittajallu, R., Esnault, C., Maric, D., Rhodes, C., Pelkey, K.A., et al. (2021). NMDARs drive the expression of neuropsychiatric disorder risk genes within GABAergic interneuron subtypes in the juvenile brain. Front. Mol. Neurosci. *14*, 712609. https://doi.org/10.3389/fnmol.2021.712609.
60. Sanz, E., Yang, L., Su, T., Morris, D.R., McKnight, G.S., and Amieux, P.S. (2009). Cell-type-specific isolation of ribosome-associated mRNA from complex tissues. Proc. Natl. Acad. Sci. USA *106*, 13939–13944. https://doi.org/10.1073/pnas.0907143106.
61. Mahadevan, V., Peltekian, A., and McBain, C.J. (2020). Translatome analyses using conditional ribosomal tagging in GABAergic interneurons and other sparse cell types. Curr. Protoc. Neurosci. *92*, e93. https://doi.org/10.1002/cpns.93.
62. Paul, A., Crow, M., Raudales, R., He, M., Gillis, J., and Huang, Z.J. (2017). Transcriptional architecture of synaptic communication delineates GABAergic neuron identity. Cell *171*, 522–539.e20. https://doi.org/10.1016/j.cell.2017.08.032.
63. Favuzzi, E., Deogracias, R., Marques-Smith, A., Maeso, P., Jezequel, J., Exposito-Alonso, D., Balia, M., Kroon, T., Hinojosa, A.J., F Maraver, E.F., et al. (2019). Distinct molecular programs regulate synapse specificity in cortical inhibitory circuits. Science *363*, 413–417. https://doi.org/10.1126/science.aau8977.
64. Darnell, J.C., Van Driesche, S.J.V., Zhang, C., Hung, K.Y.S., Mele, A., Fraser, C.E., Stone, E.F., Chen, C., Fak, J.J., Chi, S.W., et al. (2011). FMRP stalls ribosomal translocation on mRNAs linked to synaptic function and autism. Cell *146*, 247–261. https://doi.org/10.1016/j.cell.2011.06.013.
65. Maurin, T., Lebrigand, K., Castagnola, S., Paquet, A., Jarjat, M., Popa, A., Grossi, M., Rage, F., and Bardoni, B. (2018). HITS-CLIP in various brain areas reveals new targets and new modalities of RNA binding by fragile X mental retardation protein. Nucleic Acids Res. *46*, 6344–6355. https://doi.org/10.1093/nar/gky267.
66. Cruz-Martín, A., Crespo, M., and Portera-Cailliau, C. (2010). Delayed stabilization of dendritic spines in fragile X mice. J. Neurosci. *30*, 7793–7803. https://doi.org/10.1523/JNEUROSCI.0577-10.2010.
67. He, Q., Nomura, T., Xu, J., and Contractor, A. (2014). The developmental switch in GABA polarity is delayed in fragile X mice. J. Neurosci. *34*, 446–450. https://doi.org/10.1523/JNEUROSCI.4447-13.2014.

68. Du, J., Zhang, L., Weiser, M., Rudy, B., and McBain, C.J. (1996). Developmental expression and functional characterization of the potassium-channel subunit Kv3.1b in parvalbumin-containing interneurons of the rat hippocampus. J. Neurosci. *16*, 506–518. https://doi.org/10.1523/JNEUROSCI.16-02-00506.1996.

69. Rudy, B., and McBain, C.J. (2001). Kv3 channels: voltage-gated K+ channels designed for high-frequency repetitive firing. Trends Neurosci. *24*, 517–526. https://doi.org/10.1016/s0166-2236(00)01892-0.

70. Green, S.A., Hernandez, L., Tottenham, N., Krasileva, K., Bookheimer, S.Y., and Dapretto, M. (2015). Neurobiology of sensory overresponsivity in youth with autism spectrum disorders. JAMA Psychiatry *72*, 778–786. https://doi.org/10.1001/jamapsychiatry.2015.0737.

71. Anastasiades, P.G., Marques-Smith, A., Lyngholm, D., Lickiss, T., Raffiq, S., Kätzel, D., Miesenböck, G., and Butt, S.J.B. (2016). GABAergic interneurons form transient layer-specific circuits in early postnatal neocortex. Nat. Commun. *7*, 10584. https://doi.org/10.1038/ncomms10584.

72. Haberl, M.G., Zerbi, V., Veltien, A., Ginger, M., Heerschap, A., and Frick, A. (2015). Structural-functional connectivity deficits of neocortical circuits in the Fmr1-/y mouse model of autism. Sci. Adv. *1*, e1500775. https://doi.org/10.1126/sciadv.1500775.

73. Molnár, Z., Luhmann, H.J., and Kanold, P.O. (2020). Transient cortical circuits match spontaneous and sensory-driven activity during development. Science *370*, eabb2153. https://doi.org/10.1126/science.abb2153.

74. Filice, F., Vörckel, K.J., Sungur, A.Ö., Wöhr, M., and Schwaller, B. (2016). Reduction in parvalbumin expression not loss of the parvalbumin-expressing GABA interneuron subpopulation in genetic parvalbumin and shank mouse models of autism. Mol. Brain *9*, 10. https://doi.org/10.1186/s13041-016-0192-8.

75. Gonchar, Y., Wang, Q., and Burkhalter, A. (2007). Multiple distinct subtypes of GABAergic neurons in mouse visual cortex identified by triple immunostaining. Front. Neuroanat. *1*, 3. https://doi.org/10.3389/neuro.05.003.2007.

76. Huang, Z.J., Kirkwood, A., Pizzorusso, T., Porciatti, V., Morales, B., Bear, M.F., Maffei, L., and Tonegawa, S. (1999). BDNF regulates the maturation of inhibition and the critical period of plasticity in mouse visual cortex. Cell *98*, 739–755. https://doi.org/10.1016/s0092-8674(00)81509-3.

77. Tomassy, G.S., Morello, N., Calcagno, E., and Giustetto, M. (2014). Developmental abnormalities of cortical interneurons precede symptoms onset in a mouse model of Rett syndrome. J. Neurochem. *131*, 115–127. https://doi.org/10.1111/jnc.12803.

78. del Río, J.A., de Lecea, L., Ferrer, I., and Soriano, E. (1994). The development of parvalbumin-immunoreactivity in the neocortex of the mouse. Brain Res. Dev. Brain Res. *81*, 247–259. https://doi.org/10.1016/0165-3806(94)90311-5.

79. Mukhopadhyay, A., McGuire, T., Peng, C.-Y., and Kessler, J.A. (2009). Differential effects of BMP signaling on parvalbumin and somatostatin interneuron differentiation. Development *136*, 2633–2642. https://doi.org/10.1242/dev.034439.

80. Patz, S., Grabert, J., Gorba, T., Wirth, M.J., and Wahle, P. (2004). Parvalbumin expression in visual cortical interneurons depends on neuronal activity and TrkB ligands during an Early period of postnatal development. Cereb. Cortex *14*, 342–351. https://doi.org/10.1093/cercor/bhg132.

81. Kang, Y., Zhou, Y., Li, Y., Han, Y., Xu, J., Niu, W., Li, Z., Liu, S., Feng, H., Huang, W., et al. (2021). A human forebrain organoid model of fragile X syndrome exhibits altered neurogenesis and highlights new treatment strategies. Nat. Neurosci. *24*, 1377–1391. https://doi.org/10.1038/s41593-021-00913-6.

82. Bassell, G.J., and Warren, S.T. (2008). Fragile X syndrome: loss of local mRNA regulation alters synaptic development and function. Neuron *60*, 201–214. https://doi.org/10.1016/j.neuron.2008.10.004.

83. Veenstra-VanderWeele, J., and Warren, Z. (2015). Intervention in the context of development: pathways toward new treatments. Neuropsychopharmacology *40*, 225–237. https://doi.org/10.1038/npp.2014.232.

84. Rogers, S.J., Hepburn, S., and Wehner, E. (2003). Parent reports of sensory symptoms in toddlers with autism and those with other developmental disorders. J. Autism Dev. Disord. *33*, 631–642. https://doi.org/10.1023/b:jadd.0000006000.38991.a7.

85. Stringer, C., Wang, T., Michaelos, M., and Pachitariu, M. (2021). Cellpose: a generalist algorithm for cellular segmentation. Nat. Meth. *18*, 100–106. https://doi.org/10.1038/s41592-020-01018-x.

86. Cantu, D.A., Wang, B., Gongwer, M.W., He, C.X., Goel, A., Suresh, A., Kourdougli, N., Arroyo, E.D., Zeiger, W., and Portera-Cailliau, C. (2020). EZcalcium: open-source toolbox for analysis of calcium imaging data. Front. Neural Circuits *14*, 25. https://doi.org/10.3389/fncir.2020.00025.

87. Love, M.I., Huber, W., and Anders, S. (2014). Moderated estimation of fold change and dispersion for RNA-seq data with DESeq2. Genome Biol. *15*, 550. https://doi.org/10.1186/s13059-014-0550-8.

88. Anders, S., Pyl, P.T., and Huber, W. (2015). HTSeq–a Python framework to work with high-throughput sequencing data. Bioinformatics *31*, 166–169. https://doi.org/10.1093/bioinformatics/btu638.

89. Wu, T., Hu, E., Xu, S., Chen, M., Guo, P., Dai, Z., Feng, T., Zhou, L., Tang, W., Zhan, L., et al. (2021). clusterProfiler 4.0: A universal enrichment tool for interpreting omics data. Innovation (Camb) *2*, 100141. https://doi.org/10.1016/j.xinn.2021.100141.

90. He, C.X., Arroyo, E.D., Cantu, D.A., and Goel, A. (2018). A versatile method for viral transfection of calcium indicators in the neonatal mouse brain. Front. Neural Circuits *12*. 12851-12813. https://doi.org/10.3389/fncir.2018.00056.

91. Zeiger, W.A., Marosi, M., Saggi, S., Noble, N., Samad, I., and Portera-Cailliau, C. (2021). Barrel cortex plasticity after photothrombotic stroke involves potentiating responses of pre-existing circuits but not functional remapping to new circuits. Nat. Commun. *12*, 3972. https://doi.org/10.1038/s41467-021-24211-8.

92. Pologruto, T.A., Sabatini, B.L., and Svoboda, K. (2003). ScanImage: flexible software for operating laser scanning microscopes. Biomed. Eng. OnLine *2*, 13. https://doi.org/10.1186/1475-925X-2-13.

93. Marshel, J.H., Kim, Y.S., Machado, T.A., Quirin, S., Benson, B., Kadmon, J., Raja, C., Chibukhchyan, A., Ramakrishnan, C., Inoue, M., et al. (2019). Cortical layer-specific critical dynamics triggering perception. Science *365*, eaaw5202. https://doi.org/10.1126/science.aaw5202.

94. Schroeder, A., Mueller, O., Stocker, S., Salowsky, R., Leiber, M., Gassmann, M., Lightfoot, S., Menzel, W., Granzow, M., and Ragg, T. (2006). The RIN: an RNA integrity number for assigning integrity values to RNA measurements. BMC Mol. Biol. *7*, 3. https://doi.org/10.1186/1471-2199-7-3.

95. Gandal, M.J., Zhang, P., Hadjimichael, E., Walker, R.L., Chen, C., Liu, S., Won, H., van Bakel, H., Varghese, M., Wang, Y., et al. (2018). Transcriptome-wide isoform-level dysregulation in ASD, schizophrenia, and bipolar disorder. Science *362*, eaat8127. https://doi.org/10.1126/science.aat8127.

96. Langfelder, P., and Horvath, S. (2008). WGCNA: an R package for weighted correlation network analysis. BMC Bioinformatics *9*, 559. https://doi.org/10.1186/1471-2105-9-559.

97. Dombeck, D.A., Khabbaz, A.N., Collman, F., Adelman, T.L., and Tank, D.W. (2007). Imaging large-scale neural activity with cellular resolution in awake, mobile mice. Neuron *56*, 43–57. https://doi.org/10.1016/j.neuron.2007.08.003.

98. Mineault, P.J., Tring, E., Trachtenberg, J.T., and Ringach, D.L. (2016). Enhanced spatial resolution during locomotion and heightened attention in mouse primary visual cortex. J. Neurosci. *36*, 6382–6392.

Please cite this article in press as: Kourdougli et al., Improvement of sensory deficits in fragile X mice by increasing cortical interneuron activity after the critical period, Neuron (2023), https://doi.org/10.1016/j.neuron.2023.06.009

STAR★METHODS

KEY RESOURCES TABLE

REAGENT or RESOURCE	SOURCE	IDENTIFIER
Antibodies		
Mouse anti-Parvalbumin	Sigma-Aldrich	Cat# SAB4200545; RRID:AB_2857970
Mouse anti-Parvalbumin	Swant	Cat# 235; RRID:AB_10000343
Rat anti-Somatostatin	Abcam	Cat# Ab108456; RRID:AB_11158517
Mouse anti-Calretinin	Milllipore	Cat#MAB1568; RRID:AB_94259
Rabbit anti-Calretinin	Swant	Cat# 7697; RRID:AB_2721226
Mouse anti-Calbindin	Swant	Cat# 300 ;RRID:AB_10000347
Rabbit anti-Calbindin	Thermo Fischer Scientific	Cat# PA5-85669; RRID:AB_2792808
Rabbit anti-cleaved caspase3	Cell signaling	Cat# D175-%A1E; RRID:AB_2070042
Chicken anti-GFP	Thermo Fischer Scientific	Cat# 600-901-215; RRID:AB_1537402
Rat anti-mCherry	Thermo Fischer Scientific	Cat# M11240; RRID:AB_2536614
Bacterial and virus strains		
AAV1-Syn-GCaMP6s-WPRE-SV40	Addgene	Cat #100843
AAV1-CAG-Flex-GCaMP6s-WPRE.SV40	Addgene	Cat #100842
AAV8-Ef1a-fDIO-GCaMP6s	Addgene	Cat #105714
AAV1-hSyn-DIO-hM3D(Gq)-mCherry	Addgene	Cat #44361
AAV5-hSyn-DIO-mCherry	Addgene	Cat #50459-AAV5
AAV8-hSyn-DIO-mCherry	Addgene	Cat #50459-AAV8
Biological samples		
Human brain samples	CENE	https://health.ucdavis.edu/mindinstitute/research/cene-brain-bank/cene-about.html
Deposited data		
RNAseq transcriptomic and translatome data at P15	This paper	https://github.com/porteralab/MGERNAseq
Experimental models: Organisms/strains		
Mouse: C57BL/6J (WT)	Jackson Laboratories	Cat #000664
Mouse: B6.129P2-*Fmr1*^{tm1Cgr}/J (C57BL/6J-*Fmr1*$^{-/-}$)	Jackson Laboratories	Cat # 003025
Mouse: FVB.129P2-*Pde6b*$^{+}$ *Tyr*$^{c-ch}$/AntJ (FVB)	Jackson Laboratories	Cat #004828
Mouse: FVB.129P2-*Pde6b*$^{+}$ *Tyr*$^{c-ch}$ *Fmr1*^{tm1Cgr}/J (FVB-Fmr1$^{-/-}$)	Jackson Laboratories	Cat #004826
Mouse: B6;129P2-*Pvalb*$^{tm1(cre)Arbr}$/J (PV-Cre)	Jackson Laboratories	Cat #008069
Mouse: B6.Cg-*Gt(ROSA)26Sor*$^{tm9(CAG-tdTomato)Hze}$/J (Ai9)	Jackson Laboratories	Cat #007909
Mouse: C57BL/6J-Tg(Nkx2-1-cre)2Sand/J (Nkx2.1-Cre)	Jackson Laboratories	Cat #008661
Mouse: B6.Cg-*Gt(ROSA)26Sor*$^{tm14(CAG-tdTomato)Hze}$/J (Ai14)	Jackson Laboratories	Cat #007914
Mouse: B6J.Cg-*Sst*$^{tm3.1(flpo)Zjh}$/AreckJ (SST-FLP)	Jackson Laboratories	Cat #031629
Mouse: B6N.129-*Rpl22*$^{tm1.1Psam}$/J	Jackson Laboratories	Cat #011029
Software and algorithms		
ImajeJ-Fiji 2.0.0	NIH	https://imagej.nih.gov/ij/
MATLAB 2009a/ 2018b/2020a/2022a	MathWorks	https://www.mathworks.com/

(*Continued on next page*)

Continued

REAGENT or RESOURCE	SOURCE	IDENTIFIER
GraphPad Prism	GraphPad Software	https://www.graphpad.com/features
ThorImageLS 4	Thorlabs	https://www.thorlabs.com/
Python 3.8.5	Python Software Foundation	https://www.python.org/
R 4.0.3	R package	https://www.npackd.org/p/r/4.0.3
Suite2P	Janelia Research Campus	https://github.com/MouseLand/suite2p
Cellpose2.0	Stringer et al.[85]	https://github.com/MouseLand/cellpose
EZCalcium	Cantu et al.[86]	https://github.com/porteralab/EZcalcium
DESEQ2	Love et al.[87]	https://github.com/porteralab/EZcalcium
HTseq -count	Anders et al.[88]	N/A
Bioconductor clusterProfiler 4.0	Wu et al.[89]	N/A

RESOURCE AVAILABILITY

Lead contact

Further information and requests for resources and reagents should be directed to and will be fulfilled by the lead contact, Dr. Carlos Portera-Cailliau (cpcailliau@mednet.ucla.edu).

Materials availability

This study did not generate new unique reagents.

Data and code availability

This paper does not report original code. Previously published codes are publicly available at https://github.com/porteralab as listed in the key resources table.

The RNA-seq data generated in this study are publicly available at https://github.com/porteralab/MGERNAseq, as listed in the key resources table.

EXPERIMENTAL MODEL AND STUDY PARTICIPANT DETAILS

Mice lines

All experiments followed the U.S. National Institutes of Health guidelines for animal research, under an animal use protocol (ARC #2007-035) approved by the Chancellor's Animal Research Committee and Office for Animal Research Oversight at the University of California, Los Angeles. All mice were housed in a vivarium with a 12/12 h light/dark cycle and experiments were performed during the light cycle. Mice of both sexes were used in this study (males are represented by a square and females by a circle). Because we use both sexes, we use *Fmr1* KO to describe both male (*Fmr1*$^{-/y}$) and female (Fmr1$^{-/-}$) knockout mice. No sex differences were found in this study.The mouse lines used in this study were obtained from Jackson laboratory: *PV-Cre* mice (JAX 008069), *Ai9*;WT (JAX 007909), *Nkx2.1-Cre;WT* (JAX 008661), *Ai14*;WT (JAX 007914), *Sst-FlpO* (JAX 031629), *Ai65F*;WT (JAX 032864), *Rpl22*$^{HA/HA}$ (JAX0110029). Mouse lines were crossed to WT (JAX line 000664) or *Fmr1* KO female mice (JAX 003025). *PV-Cre* mice and Ai9 reporter lines (both on C57BL/6J background) were back crossed to FVB WT and *Fmr1* KO mice for 10-12 generations.[14] For this study, the following mouse lines were generated: *Nkx2.1-Cre*$^{+/-}$;*Fmr1* KO, Ai14$^{+/+}$;*Fmr1* KO, *Sst-FlpO*$^{+/+}$;*Fmr1* KO, *Nkx2.1-Cre*$^{+/-}$;*Sst-FlpO*$^{+/+}$ WT, *Nkx2.1-Cre*$^{+/-}$;*Sst-FlpO*$^{+/+-}$;*Fmr1* KO, *Nkx2.1-Cre*$^{+/-}$;*Rpl22*$^{HA/HA}$;*WT, Nkx2.1-Cre*$^{+/-}$;*Rpl22*$^{HA/HA}$;*Fmr1* KO. PV-Cre, Nkx2.1-Cre, SST-FlpO, Rpl22 ^{HA}, Ai9 and Ai14 transgenic lines were used as heterozygotes mice in this study.

Study participant details

We collected post-mortem cortical samples of Brodmann Area 3 from 8 FXS cases and 8 neurotypical, sex and age-matched cases (Table S1). The formalin-fixed tissue was obtained from CENE (Hispano-American brain bank of Neurodevelopmental Conditions, https://health.ucdavis.edu/mindinstitute/research/cene-brain-bank/cene-about.html). The neurotypical cases were determined to be free of neurological disorders, including autism or intellectual disability, based on medical records and information gathered at the time of death from next of kin. All cases were males, except for one control case and one FXS case, and no gender difference were found.

METHOD DETAILS

Viral injections

Depending on the experiment, stereotaxic viral injections were done using glass micropipettes (Sutter Instrument, 1.5 mm outer diameter, 0.86 mm inner diameter) through burr holes (at P0-P1 or P6) or at the time of the cranial window (at P10 or P15; see below).

All mice were anesthetized with isoflurane (5% induction, 1-1.5% maintenance via a nose cone, v/v) and placed in a stereotaxic frame with rubber ear bars. Pups were allowed to recover on a warm water circulation blanket before being returned to the dam. For injections at P0-P1, we made a small skin incision on the scalp over the right hemisphere under sterile conditions and drilled a small burr hole over the right S1 cortex using a dental drill, as previously described.[90] A single injection of 250-350 nL of rAAV was done using a Picospritzer (General Valve, 30 pulses of 6 ms, 30 psi). For injections at P10 or P15, we typically pressure-injected 250-350 nL of rAAV at 4-6 different locations over S1 cortex at a depth of 0.2 mm below the dura (30 pulses, 6 ms each, 30 psi). The following viruses were used: AAV1-Syn-GCaMP6s-WPRE-SV40 (Addgene 100843), AAV1-CAG-Flex-GCaMP6s-WPRE.SV40 (Addgene 100842), AAV8-Ef1a-fDIO-GCaMP6s (Addgene 105714), AAV1-hSyn-DIO-hM3D(Gq)-mCherry (Addgene 44361), AAV-hSyn-DIO-mCherry (Addgene 50459-AAV1, 50459-AAV8), AAV8-nEF-Con/Foff-ChRmine-oScarlet, AAV8-EF1a-Con/Foff-2.0-mCherry (Addgene 137133).

Cranial windows

Pups were anesthetized with isoflurane (5% induction, 1.5–2% maintenance via a nose cone, v/v) and secured in a stereotaxic frame with rubber ear bars. A 3.0–3.5 mm diameter craniotomy was performed over the right S1 cortex, under sterile conditions, by removing the skull without disturbing the pia, as described previously.[20,31] The craniotomy was then covered with a 3 mm glass coverslip and secured by cyanoacrylate glue and dental cement. An aluminum head bar was attached to the skull contralaterally to the window with dental cement to secure the animal to the microscope stage. Within 1 h after surgery, the pups appeared fully recovered from the effects of anesthesia and could be returned to their dam. For in vivo imaging at P6 and P10, cranial windows were performed on the day of the recording under 1-1.5% isoflurane anesthesia (5% induction) and we allowed mice to recover for 4-6 h with their dam prior to calcium imaging. For in vivo calcium imaging at P15 or P21, cranial windows were implanted at P10 and P15, respectively, during which we performed GCaMP6s viral injections.

Intrinsic signal imaging

For animals undergoing calcium imaging at P15 or P21, we previously mapped the location of the barrel field of S1 cortex (S1BF), with intrinsic signal imaging, 1-3 d after cranial window surgery, as described previously.[91] The cortical surface was illuminated by green LEDs (535 nm) to visualize the superficial vasculature. The macroscope was then focused ~300 μm below the cortical surface and red LEDs (630 nm) were used to record intrinsic signals, with frames collected at 30 Hz 0.9 s before and 1.5 s after stimulation, using a fast CCD camera (Teledyne Dalsa Pantera 1M60), a frame grabber (64 Xcelera-CL PX4, Dalsa), and custom routines written in MATLAB (version 2009a). Thirty trials separated by 20 s were conducted for each imaging session. The whiskers contralateral to the cranial window were bundled together using bone wax and gently attached to a glass microelectrode coupled to a ceramic piezo-actuator (PI127-Physik Instrumente). Each stimulation trial consisted of a 100 Hz sawtooth stimulation lasting 1.5 s. The response signal was divided by the averaged baseline signal, summed for all trials, with a threshold at a fraction (65%) of maximum response to delineate the cortical representation of stimulated whiskers and guide viral injections to S1BF.

In vivo two-photon (2P) calcium imaging in head-restrained mice

Calcium imaging was performed on one of two microscopes. For Figures 1, 8, S12A, S12B, and S12G–S12I, we used a custom-built 2P microscope and acquired frames (1024x128 down sampled to 256 x 128 pixels, 210x105 μm) at 7.8 Hz with a 20x objective (0.95 NA, Olympus) and ScanImage software.[92] For Figures 2, 7, S2, S3E–S3G, S4, S5C, S11, and S12C–S12F, we used a Bergamo II (Thorlabs) at 15.13 Hz (512 x 512 pixels, or 667 x 667 μm) with the same 20x objective. Both microscopes were coupled to a Chameleon Ultra II Ti:sapphire laser (Coherent) tuned to 930 nm (average power at the sample was <90 mW). We imaged at a depth of 170-190 μm or 220-250 μm below the dura for P6-P10 mice and P15-P21 mice, respectively, corresponding to L2/3. At P15 and P21, mice were lightly sedated with chlorprothixene (2 mg/kg, i.p.) and isoflurane (0.1-0.5%) and kept at 37°C using a temperature control device and heating blanket (Harvard Apparatus). The isoflurane level was manually adjusted to maintain a constant breathing rate (100-150 breaths/min for P15-P16 mice and 140-150 breaths/min for P21 mice). For P6 and P10 experiments mice were unanesthetized and placed in a cotton pad and kept at 37°C using a temperature control device and heating blanket (Harvard Apparatus).[31] Whisker stimulation was achieved by bundling the contralateral whiskers (typically all macrovibrissae of at least 1 cm in length) with soft bone wax and attaching them to a glass capillary coupled to a piezo-actuator.

In vivo two-photon optogenetic stimulation

Optogenetic photostimulation of ChRmine-expressing neurons[93] was performed by scanning (at 15.1 fps) a separate 1,040 nm femtosecond-pulsed laser (Fidelity, Coherent) using the same 2P microscope (Bergamo II). Laser power was typically 50-60 mW at the objective. Photostimulation consisted of twenty 1 s-long stimulation pulses, with an inter-stimulation interval of 3 s, and was controlled by an optical beam shutter controller (SC10, Thorlabs) triggered via custom-built MATLAB code.

Nkx2.1-Cre-specific RiboTag RNA extraction and sequencing

Aged matched (P15), *Nkx2.1-Cre*$^{+/-}$;*Rpl22*$^{HA/-}$;*WT or Nkx2.1-Cre*$^{+/-}$;*Rpl22*$^{HA/-}$;*Fmr1* KO, injected at P1 with AAV virus expressing mCherry or hM3Dq were used for the RiboTag RNA sequencing experiments. For each RNA isolation experiment, coronal sections (1.5 mm thick) containing S1 (A/P -0.5 to +1.82mm, M/L 3.0 to 4.0 mm) were collected and placed in chilled choline-ACSF (132 mM choline, 2.5 mM KCl, 1.25 mM NaH2PO4, 25 mM NaHCO3, 7 mM MgCl2, 0.5 mM CaCl2, and 8 mM D-glucose), from which we

dissected S1 bilaterally. Samples were independently homogenized with a 2 mL Dounce homogenizer in 1mL of supplemented homogenization buffer containing: 1% w/v, HB-S; 1 mM DTT, Protease inhibitors (1X), RNAsin (200 units/mL), Cycloheximide (2 mg/l), Heparin (1mg/mL). 100 μL of the homogenate was used for isolating bulk RNA from S1 cortex. To isolate mRNA of HA-tagged Nkx2.1+ IN-specific ribosomes from non-HA tagged ribosomes, samples were incubated for 4 h with an anti-HA antibody (1:180, 5 μL in 900 μL of homogenate; 901513 Covance Anti-HA antibody), followed by overnight incubation with magnetic beads (Pierce Protein A/G Magnetic Beads 88802, 200 μL) at 4°C at 15 rpm centrifugation. The supernatant was washed thrice with 800 μL of high salt buffer (Tris 50mM, KCl 300mM, $MgCl_2$ 12mM, 10% NP-40 (1%), DTT 1mM, Cycloheximide 100μg/ml, dH_2O), centrifuged at 15 rpm for 10 min at 4°C. For RNA extraction, we used Zymo Research Direct-zol RNA Miniprep kit (R2051) for the homogenate (input), and the Zymo Research Direct-zol RNA Microprep kit (R2061) for the bead-antibody-protein sample (IP); RNA was eluted with DNAase/RNAse-free water. RNA Integrity Number (RIN) scores were used to evaluate the integrity of RNA through the ratio of 28S:18S ribosomal RNA (Agilent TapeStation 4200).[94] We set a minimum of RIN score 7 for our samples.[95] RNA sequencing libraries were prepared using Ovation® RNA-Seq System V2. Libraries were multiplexed for paired-end 50 bp sequencing on NovaSeq S2, with read depth of 50 million reads on average. Demultiplex reads were aligned using STAR to the mouse genome (reference genome ID: mm10) and fragment counts were derived using HTS-seq.[88] Outliers were calculated by measuring connectivity between samples, using the WCGNA package[96] and removing samples >2 SD from the mean for Bulk and IP samples. All analysis was performed using R4.0.3. Differential expression analysis was performed using the Bioconductor DESEQ2 package[87] with FDR of 0.1. Go enrichment analysis was performed using Bioconductor clusterProfiler 4.0.[89] GoTerms with greater then 70% overlap of genes was combined into one category. The GoTerm with the highest category was chosen as the name of the category. Non-brain related pathways were excluded with the gene enrichment analysis. For comparisons with previously published RNAseq data, we compiled all DE genes from those studies[54–56] and compared the compiled list with our DE genes. Statistical significance was tested using the Fisher exact Test in R4.0.3.

Data analysis for calcium imaging

Calcium imaging data were analyzed using custom-written MATLAB routines (MATLAB version 2020a). X–Y drift in the movies was first corrected using either a frame-by-frame, hidden Markov model-based registration routine[97] or a cross-correlation-based, nonrigid alignment algorithm.[98] The choice of registration algorithm did not affect the data analysis since the fluorescence data for each neuron was always normalized to its own baseline. For ROI segmentation, we used either EZcalcium[86] (for Figures 1, 8E–8G, S12B, and S12G–S12I) or Suite2P (for Figures 2, 7, S2, S3E–S3G, S4, S11, and S12C–S12F). To quantify activity levels, a "modified *Z* score" *Z_F* vector (an epoch was 8 consecutive frames wherein *Z_F*> 3 for every frame of that epoch) for each neuron was calculated as *Z_F* [*F*(*t*) mean(quietest period)]/SD(quietest period), where the quietest period is the 10 s period with the lowest variation (standard deviation) in d*F*/*F*, as described previously.[20] All subsequent analyses were performed using the *Z_F* vectors. To define whether an individual cell showed responses that coincided with epochs of whisker stimulation ("stimulus-locked"), a probabilistic bootstrapping (10,000 scrambles, threshold $p<0.01$) method was implemented as previously described[20]; among the ROI comprised in the Z_F vector. To assess adaptation of neuronal activity to repetitive whisker stimulation we calculated an adaptation index: [(*Z* score during first five stimulations) - (*Z* score during last five stimulations)]/[(*Z* score during first five stimulations) + (*Z* score during last five stimulations)]. The percentage of active cells was based on the Z_F vector, calculated as of proportion of cells reaching the criterion of having at least one activity epoch with Z_F> 3 for 8 consecutive frames, amongst the total number of segmented ROIs. A Pearson's correlation coefficient was calculated for all neuron pairs in each calcium imaging movie using the Z_F vector.

Brain slice electrophysiology

PV-Cre;Ai14;*Fmr1* KO mice at P15 were deeply anesthetized using 5% isoflurane prior to decapitation and 400 μm-thick coronal slices were prepared with a vibratome (Leica VT1200S, Germany). Slices were prepared in ice-cold oxygenated (95% O_2 and 5% CO_2) modified artificial cerebrospinal fluid (ACSF) containing (in mM): 92 NMDG, 5 Na^+-ascorbate, 3 Na^+-Pyruvate 2.5 KCl, 10 $MgSO_4$, 2 $CaCl_2$, 1.2 Na2HPO_4, 24 $NaHCO_3$, 5 HEPES, 25 Glucose. Slices were then left to recover in the modified ACSF at ~33°C for 30 min before being transferred to oxygenated regular ACSF at room temperature (RT) for storage for at least 1 h prior to recording. Recordings were made at 32-33°C in oxygenated ACSF containing (in mM) 124 NaCl, 2.5 KCl, 2 $MgSO_4$, 2 $CaCl_2$, 1.2 Na2HPO_4, 24 $NaHCO_3$, 5 HEPES, 13 Glucose, and the perfusion rate was set to 5 mL/min. Whole-cell patch-clamp recordings were performed in cortical L2/3 PV-Cre-tdTom$^+$ cells. Recordings relied on fluorescence visualization using a Zeiss AxioSKOp FS+ microscope and additional verification by their intrinsic electrophysiological properties. For current-clamp recordings, the intracellular solution consisted of (in mM) 100 K-gluconate, 20 KCl, 4 ATP-Mg, 10 phosphocreatine, 0.3 GTP-Na, 10 HEPES (adjusted to pH 7.3 and 300 mOsm). Intrinsic excitability was measured as the number of action potentials evoked during a 250 ms current step at intensities of 0.05, 0.1, 0.15, 0.2, 0.25, 0.3, 0.35, 0.4, 0.45, 0.5 nA. Wash-on of AG00563 (10 μM) was performed at 32-33°C for a minimum of 5 min before assessing PV-IN intrinsic excitability. Series resistance was monitored, and recordings were discarded if series resistance changed by more than 15%, or if apparent loss of current clamp control occurred as reflected by a sudden change in the recording stability.

Immunohistochemistry and IN quantification in mouse tissue

Mice were anesthetized with 5% isoflurane and transcardially perfused with ice cold phosphate buffer saline PBS (0.1 M) followed by ice cold 4% paraformaldehyde in PBS and post-fixed overnight at 4°C. Coronal sections (60 μm) were cut on a vibratome

(Leica VT1200S). Sections were permeabilized with 0.3% Triton X-100 and blocked with 5% normal goat serum (NGS) for 1 h at RT. Sections were then incubated overnight at 4°C with the primary antibody diluted in PBS with 5% NGS and 0.1% Triton X-100. After rinsing in PBS for 5-10 min 3 times, sections were incubated for 1 h at RT with the corresponding Alexa Fluor-conjugated secondary antibody diluted in PBS (1:1000, Invitrogen). After rinsing in PBS for 5-10 min 3 times, sections were mounted onto Superfrost Plus glass slides (Vectashield Vibrance) with DAPI mounting medium and stored in the dark at RT. The following primary antibodies were used: mouse anti-parvalbumin (1:1,000, SAB4200545, Sigma Aldrich), rat anti-somatostatin (1:300, ab108456, Abcam), mouse anti-calretinin (1:500, MAB1568, Millipore), goat anti-mCherry (1:1000, M11240, Millipore), chicken anti-GFP (1:2000, 600-901-215, Thermo Fischer), rabbit anti cleaved-Caspase-3 (1:400, D175-5A1E, Cell Signalling).

To quantify IN density, sections were imaged on an ApoTome2 microscope (Zen2 software, Zeiss; 10X objective, 0.3 NA), and analyzed with ImageJ (https://imagej.nih.gov/ij/). The section sampling fraction (ssf=1/6) for S1BF was determined within [A/P: bregma -0.94mm to -1.94mm]. Composite images spanning the S1BF were acquired by stitching a grid of 4-6 confocal images (2754x2061 pixels). For Nkx2.1Cre^{+};tdTom^{+} and Pv-Cre^{+};tdTom^{+} cell count was performed by automated detection using ImageJ plug-ins (Filter minima=1.5 pixel, Process maxima prominence>200pixels). PVALB^{+} and Cleaved-Caspase3^{+} cell count was performed using Cell counter plug-in. Cortical layers were determined using DAPI counterstaining and cell counts were subdivided into layers 1-3, 4 and 5-6. The size of the total cortical area and layer-specific ROIs were measured using ImageJ. Cell counts were divided by ROI area and reported as cells/mm^2. For the quantification of Nkx2.1-Cre;tdTom^{+} or PV-Cre;tdTom^{+} overlap with GCaMP6s expression, we first applied a filter minima=2 pixels, and process maxima prominence>200pixels for both channels using ImageJ. We next used Cellpose for the segmentation of the cells in each channel (following automated diameter calibration and using the "cyto" model).[85] The generated masks for each channel were then superimposed to quantify the overlap.

Histology and IN quantification in human tissue

Tissue blocks were fixed in 10% buffered formalin, cryoprotected in a 30% sucrose solution in 0.1 M phosphate-buffered saline with 0.1% sodium azide. Tissue was embedded in optimum cutting temperature compound, and frozen at −80 °C. A cryostat was used to cut 14 μm-thick slide-mounted sections, stored at −80 °C until use. Based on Brodmann cortical neuroanatomy, blocks containing area BA3 (primary somatosensory cortex) were isolated from each case. We cut 14 μm sections on a cryostat, stained 1 section with Nissl, and chose sections that exactly matched the von Economo descriptions for BA3. On adjacent sections we performed triple immunostaining for PV, Calbindin (CB), and Calretinin (CR). We used the following primary antibodies for our quantification experiments: monoclonal mouse anti-CB-D28k (1:500, Swant 300, Switzerland), polyclonal rabbit anti-CR (1:500, Swant 7697), and monoclonal mouse anti-PV (1:500, Swant 235). Secondary antibodies were donkey anti-mouse conjugated with biotin, amplified with avidin-biotin complex (ABC) and developed with diaminobenzidine (DAB) or Vector NovaRED substrates (all from Vector, USA) for CB and PV detection, respectively. Donkey anti-rabbit antibody conjugated with alkaline phosphatase and Vector Blue substrate (Vector) was used for CR detection. Tissue was pretreated in Diva decloaker (DV2004 LX, MX, Biocare medical, USA) in a decloaking chamber (Biocare medical, USA) at 110°C for 6 min. Subsequently, immunostained tissues were immersed in 0.1% Nissl for 1 min and then dehydrated in successive baths of 50% ethanol (30 s), 70% ethanol (30 s), 95% ethanol (10 min), and 100% ethanol (5 min), isopropanol (5 min), followed by xylene (15 min). Sections were then mounted and coverslipped with Permount (Fisher). The PV-red staining was visualized as pink following Nissl staining. We quantified the number of immunopositive cells for each interneuron subtype (CB+, CR+, or PV+ cells). We processed 1 section of each case and chose a 3 mm wide bin parallel to the pial surface that extended through the cortical gray matter to include all cortical layers. We imaged the tissue a 100X oil objective (Olympus BX61 microscope Hamamatsu Camera) and quantified IN density using MBF Bioscience StereoInvestigator V.9 Software (MicroBrightField, Williston, VT), on a Precision PWS 690, Intel Xeon CPU computer (Dell) with Windows XP Professional V.2002 system (Microsoft).

DREADD agonist (C21) administration *in vivo*

For DREADD experiments, the agonist C21 (HelloBio) was dissolved in 0.9% saline to 2 mg/mL. For acute DREADD experiments at P15 in *Pv-Cre;Fmr1* KO mice, we injected C21 at 1 mg/kg s.c.[50] For the chronic DREADDs experiments in Nkx2.1 pups we injected C21 twice daily from P5 to P9 at a dose of 1 mg/kg, s.c.

AG00563 treatment *in vivo*

AG00563 (1-(4-methylbenzene-1-sulfonyl)-N-[(1,3-oxazol-2-yl)methyl]-1H-pyrrole-3-carboxamide) was synthesized by Lundbeck. Purified AG00563 was shipped to UCLA for reconstitution and experiments. AG00563 was dissolved in a solution of 10% of hydroxypropyl- β-cyclodextrine (Sigma) in 0.9% saline. For the Kv3.1 pharmacological manipulation, mice were injected with AG000563 (3 mg/kg, s.c.) either once acutely at P15, or chronically (twice daily) from P15 to P20 or P45 to P50. Control animals were injected with a vehicle solution containing 10% of hydroxypropyl-beta cyclodextrine in 0.9% saline.

Tactile defensiveness assay in head-restrained mice

We used a paradigm we previously established to assess tactile defensiveness in juvenile and adult mice.[20] Briefly, titanium head bars were implanted at P15 and then mice were habituated to head restraint and to running on an air-suspended 200 mm polystyrene ball. For habituation, mice were placed on the ball for 20 min/d for 5 consecutive days before testing at P21 or P50. On the test day,

each animal was first placed on the ball for a 3 min baseline period. Next, we performed a sham stimulation trial in which the whisker stimulator was visibly moving, but just out of the reach of the whiskers on the animal's left side. The stimulator consisted of a long, narrow comb of five slightly flexible von Frey nylon filaments that were attached to a piezoelectric actuator (Physik Instrumente). During the stimulation trial, the filaments were intercalated between the whiskers. Bundling of whiskers onto a glass capillary (as was done for calcium imaging) was not feasible for these awake experiments because the mouse could have damaged the capillary or unbundled some of its whiskers with its forepaw. The stimulation protocol consisted of a 10 s baseline followed by 20 sequential bouts of whisker deflections along the anterior–posterior direction (1 s long at 10 Hz), with a 3 s interstimulus interval, and ending with another 10 s post-stimulation baseline. A custom-written semiautomated video analysis was implemented in MATLAB to score defensive behaviors (grabbing the stimulator) and adaptive healthy behaviors (grooming), in each 1s increment of the videos during the 20 stimulations.[20]

QUANTIFICATION AND STATISTICAL ANALYSIS

Unless otherwise specified, results were plotted and tested for statistical significance using Prism 9. Statistical analyses of normality (Lilliefors and Shapiro Wilk tests) were performed on each data set; depending on whether the data significantly deviated from normality ($p<0.05$) or not ($p>0.05$), appropriate non-parametric or parametric tests were performed. The statistical tests performed are mentioned in the text and the legends. For parametric two-group analyses, a Student's t-test (paired or unpaired) was used. For non-parametric tests, we used Mann-Whitney test (two groups) and the Friedman test (repeated measures). Multiple comparisons with single variables were analyzed using one-way ANOVA with post-hoc Bonferroni's test (comparing the mean of each column with the mean of every other column) or Dunnett's test (comparing the mean of each column with the mean of a control column) for normally distributed samples. For multiple comparisons with more than one variable, a two-way ANOVA with post hoc Sidak's test was used. No statistical methods were used to predetermine sample size. Sample sizes were calculated based on similar published studies. In the figures, significance levels are represented with the following convention: * for $p<0.05$; ** for $p<0.01$, *** for $p<0.001$. All experiments were replicated at least in 3 different litters. In all the figures, we plot the standard error of the mean (s.e.m.). Graphs either show individual data points from each animal or group means (averaged over different mice) superimposed on individual data points.

Neuron, Volume *111*

Supplemental information

Improvement of sensory deficits in fragile X mice by increasing cortical interneuron activity after the critical period

Nazim Kourdougli, Anand Suresh, Benjamin Liu, Pablo Juarez, Ashley Lin, David T. Chung, Anette Graven Sams, Michael J. Gandal, Verónica Martínez-Cerdeño, Dean V. Buonomano, Benjamin J. Hall, Cédric Mombereau, and Carlos Portera-Cailliau

Supplemental information

Improvement of sensory deficits in Fragile X mice by increasing cortical interneuron activity after the critical period.

Nazim Kourdougli, Anand Suresh, Benjamin Liu, Pablo Juarez, Ashley Lin, David T. Chung, Anette Graven Sams, Michael Gandal[3] Verónica Martínez-Cerdeño, Dean V. Buonomano, Benjamin J. Hall, Cédric Mombereau, and Carlos Portera-Cailliau*.

Supplementary figures: 13
Supplementary table: 1
Supplementary videos: 2

***Lead Contact:** Carlos Portera-Cailliau

Percentage of PV-tdTom⁺ cells that express GCaMP6S at P15

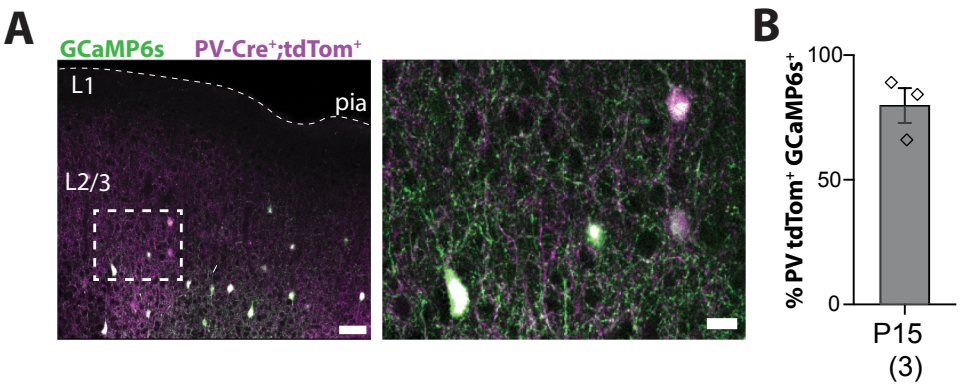

Percentage of Nkx2.1-tdTom⁺ cells that express GCaMP6S at P6

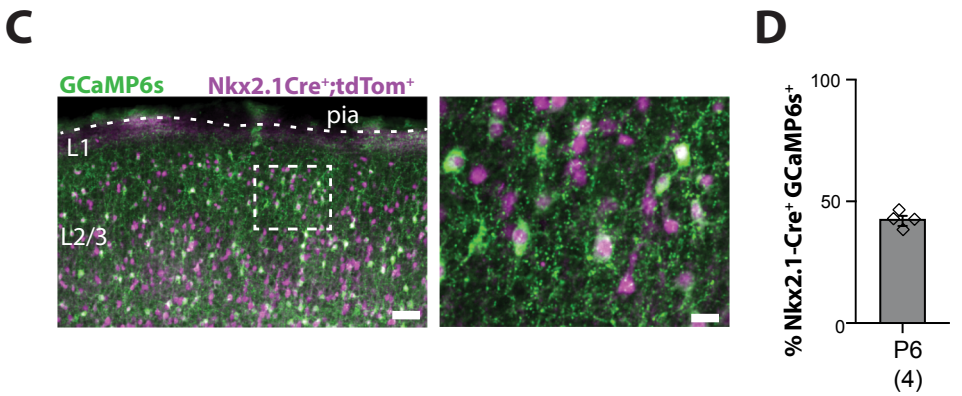

Percentage of Nkx2.1⁺-GCaMP6s⁺ cells that express SST at P6

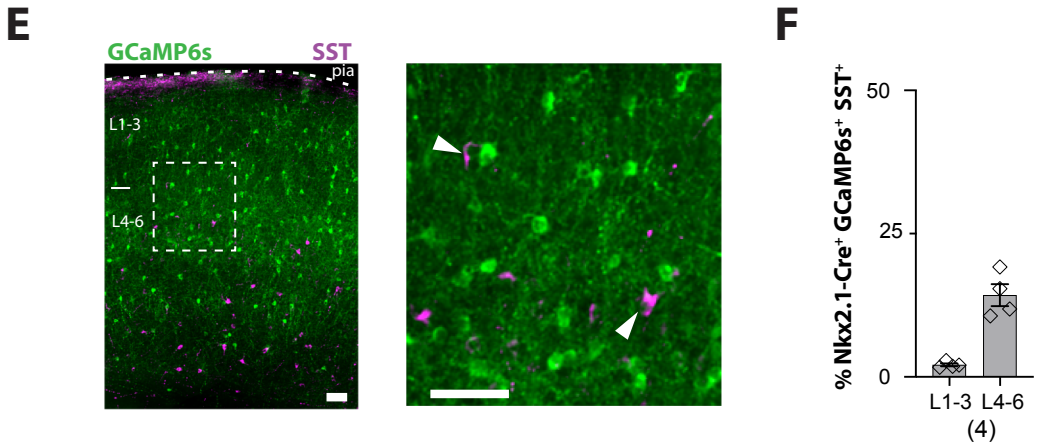

Percentage of Nkx2.1-tdTom⁺ cells that express SST at P6

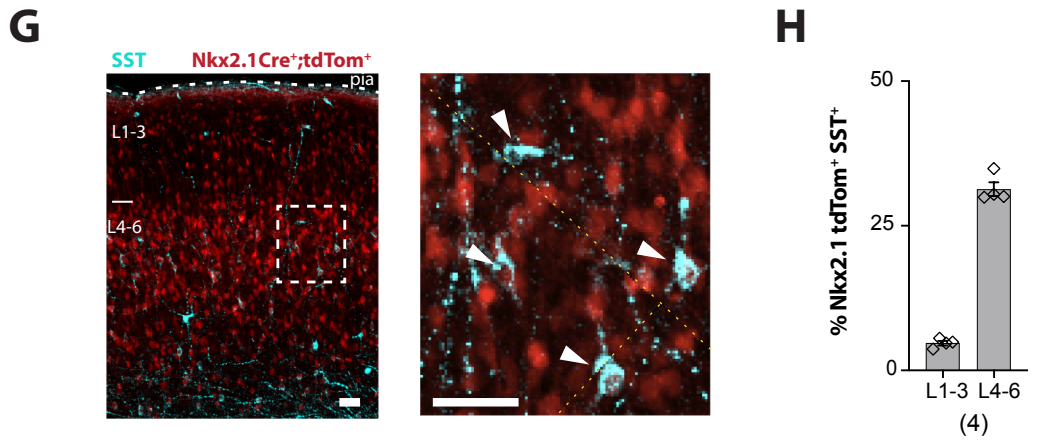

Supplementary Fig. S1

Supplementary Fig. S1: Efficacy of viral strategy to express GCaMP6s in different IN populations in P15 mice. (Related to Fig. 1)

A. Example field of view of PV-Cre^{+}-tdTom^{+} (magenta) expressing GCaMP6s (green) in PV-Cre;Ai14$^{+/-}$*; Fmr1* KO mice at P15.

B. An injection of rAAV-CAG-DIO-GCaMP6s virus in S1 at P10 resulted in a high proportion of PV-INs also expressing GCaMP6s by P15 (79.8± 7%, n=3 mice). This pertains to Fig. 1A-F. Scale= 20 µm.

C. Example field of view of Nkx2.1-Cre^{+}-tdTom^{+} (magenta) expressing GCaMP6s (green) in Nkx2.1-Cre;Ai14$^{+/-}$ *Fmr1* KO mice at P15.

D. An injection of rAAV-CAG-DIO-GCaMP6s virus in S1 at P1 resulted in 43.4± 1.6% of Nkx2.1-INs also expressing GCaMP6s (n=4 mice). Note that the density of Nkx2.1-Cre^{+}- GCaMP6s+ cells is comparable to other reports[1]. This pertains to Fig. 1G-L. Scale= 20 µm.

E. Representative image of Nkx2.1-INs expressing GCaMP6s (arrowheads, following injection of rAAV-CAG-DIO-GCaMP6s virus in S1 at P1) and immunostained for SST at P6. Scale= 50 µm.

F. Percentage of Nkx2.1-Cre^{+};GCaMPs^{+} INs that co-express SST at P6 (2.1± 0.2% in L1-L3 and 14.2± 1.9% in L4-6).

G. Representative image of Nkx2.1-Cre^{+};tdTom^{+} INs immunostained for SST at P6. Arrowheads depicts the co-expressing cells. Yellow dotted line indicates uneven stitching by Zeiss Apotome. Scale= 50 µm.

H. Percentage of Nkx2.1-Cre^{+};tdTom^{+} INs that co-express SST at P6 (4.7± 0.3% in L1-L3 and 31.3± 1.2% in L4-6).

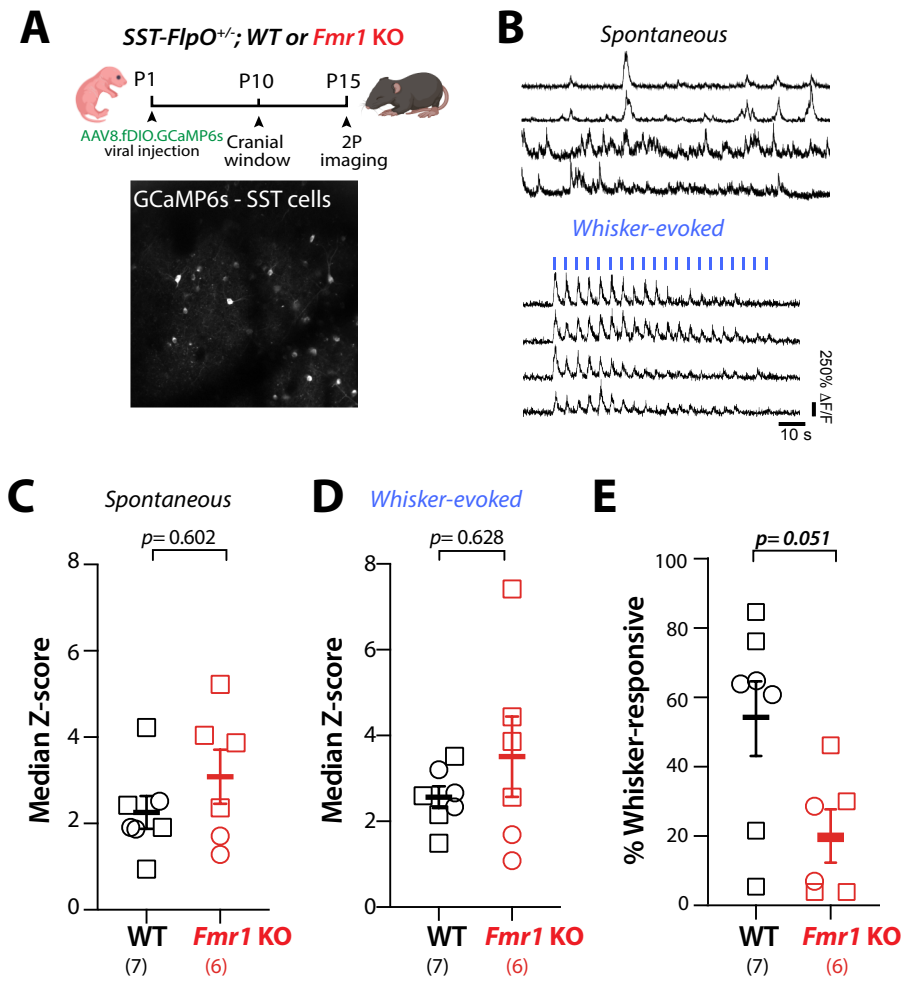

Supplementary Fig. S2

Supplementary Fig. S2: Activity of SST INs in S1 of P15 *Fmr1* KO mice is not different from WT controls. (Related to Fig. 1)

A. Top: Cartoon of experimental design for calcium imaging recordings in SST-INs. Bottom: Example field of view of SST-INs expressing GCaMP6s in SST-FlpO mice at P15.
B. Example traces of calcium transients for spontaneous and whisker-evoked activity in both SST-FlpO ; WT and SST-FlpO*; Fmr1* KO mice (we show traces from 2 different SST-INs of 2 different animals). The vertical blue bars represent the 20 whisker stimulations.
C. Mean Z-scores for spontaneous activity of SST-INs in *Fmr1* KO and WT mice at P15 (2.56± 0.38 for WT vs. 3.08± 0.62 for *Fmr1* KO, n=6 and 7 mice, respectively; p=0.602, MW t-test).
D. Mean Z-scores for whisker-evoked activity of SST-INs in *Fmr1* KO and WT mice at P15 (2.56± 0.25 for WT vs. 3.51± 0.94 for *Fmr1* KO, p=0.628, MW t-test).
E. Percentage of whisker-responsive SST-INs in *Fmr1* KO and WT mice at P15 (53.8± 11.0% for WT vs. 19.6± 7.6% for *Fmr1* KO, p= 0.051, M-W t-test).

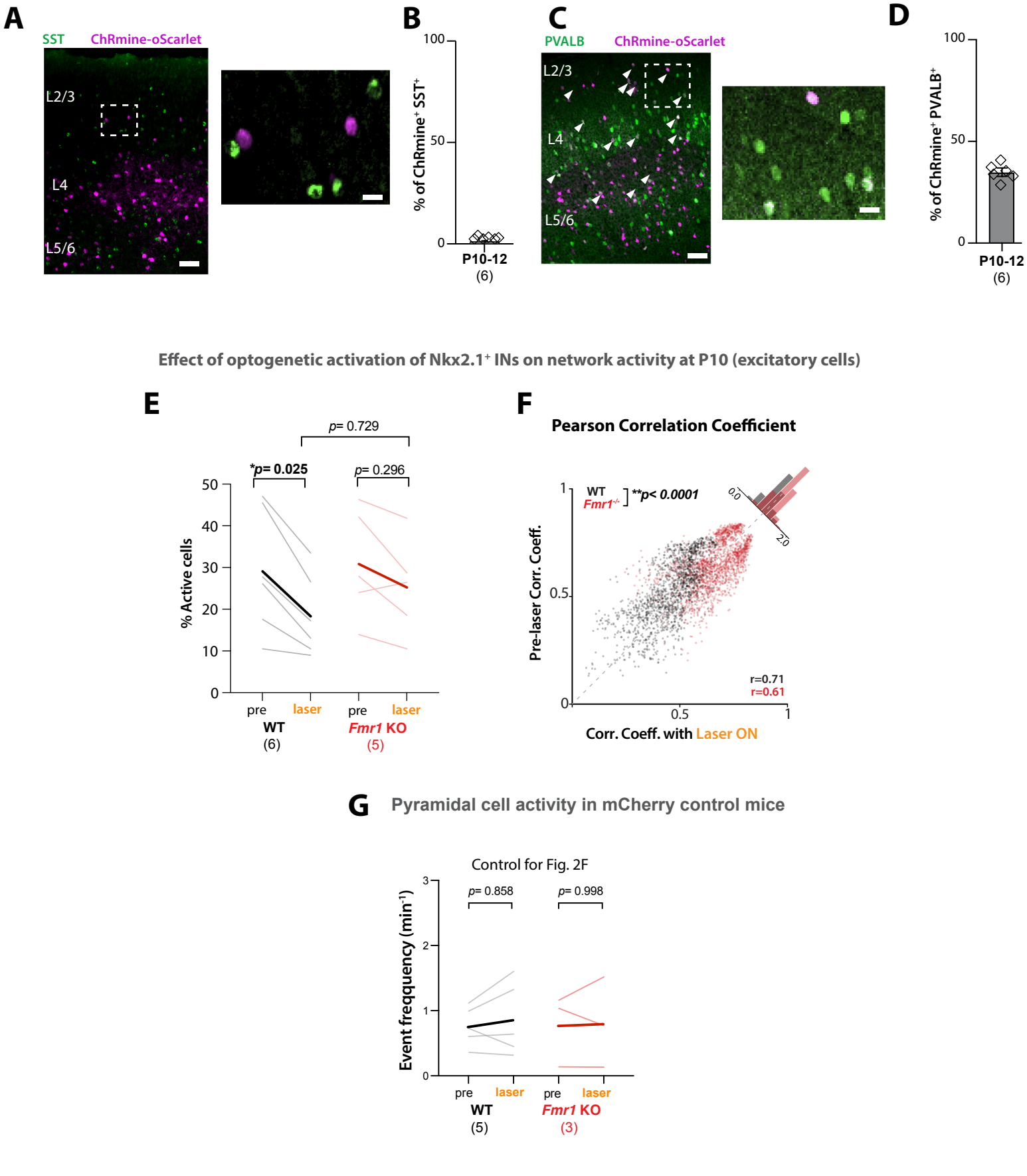

Supplementary Fig. S3

Supplementary Fig. S3: Controls for optogenetic experiments to stimulate Nkx2.1-INs in an attempt to modulate Pyr neurons in neonatal *Fmr1* KO mice at P10. (Related to Fig. 2)

A. Example field of view in S1 of Nkx2.1-Cre;Sst-FlpO*; Fmr1* KO expressing ChRmine (magenta), using AAV-EF1-CreON/FlpOFF-ChRmine-oScarlet- virus) and immunostained for SST (green).
B. Quantification of ChRmine^{+} cells that also express either PVALB or SST (by immunohistochemistry). As expected almost none of the ChRmine-labeled cells were SST immunoreactive (1.2± 0.4%, n= 6 mice), confirming the intersectional strategy worked as intended to target Nkx2.1^{+} but SST-FlpO^{+} cells at P10.
C. Example field of view in S1of Nkx2.1-Cre;Sst-FlpO*; Fmr1* KO expressing ChRmine (same as in b) and immunostained for SST (green). White arrowheads indicate double labeled cells.
D. Quantification of ChRmine^{+} cells that are also immunoreactive for PVALB. Overall, 34.9± 2.1% the ChRmine-labeled also expressed PVALB (n= 6 mice). This is consistent with the fact that at this developmental stage (P10-P12) not all future PV-IN have started expressing PVALB.
E. The percentage of active Pyr cells is significantly reduced upon laser stimulation of ChRmine-expressing future PV-INs in WT mice but is unchanged in *Fmr1* KO mice (29.1± 6.0 pre laser vs. 18.3± 4.0 laser On, p=0.025 in WT mice vs. 30.9± 5.9 pre laser vs. 25.2± 5.2 laser On in *Fmr1* KO mice, p=0.296, two-way ANOVA post-hoc Tukey).
F. Change in pairwise correlation coefficients after optogenetic Nkx2.1-IN activation in Nkx2.1-Cre;Sst-FlpO mice for individual pairs of neurons (Spearman r=0.71, n=1,449 neuron pairs from n=6 WT mice; Spearman r=.0.61, n=1,842 neuron pairs from n=5 *Fmr1*^{KO} mice). Note that correlation coefficients are significantly reduced by laser stimulation in WT mice, but not in *Fmr1* KO mice, as shown by the frequency distribution ($p<0.001$, Kolmogorov-Smirnov test).
G. Mean frequency of Pyr cell calcium transients remained unchanged upon optogenetic stimulation in Nkx2.1-Cre;Sst-FlpO WT and *Fmr1* KO mice that do not express the opsin ChRmine (mCherry controls; 0.67± 0.13 pre laser vs. 0.86± 0.25 laser On, p=0.312 in WT mice; 0.78± 0.32 pre laser vs. 0.81± 0.4 laser On, p=0.500, n=5 WT and n=3 *Fmr1* KO , two-way ANOVA, post-hoc Tukey).

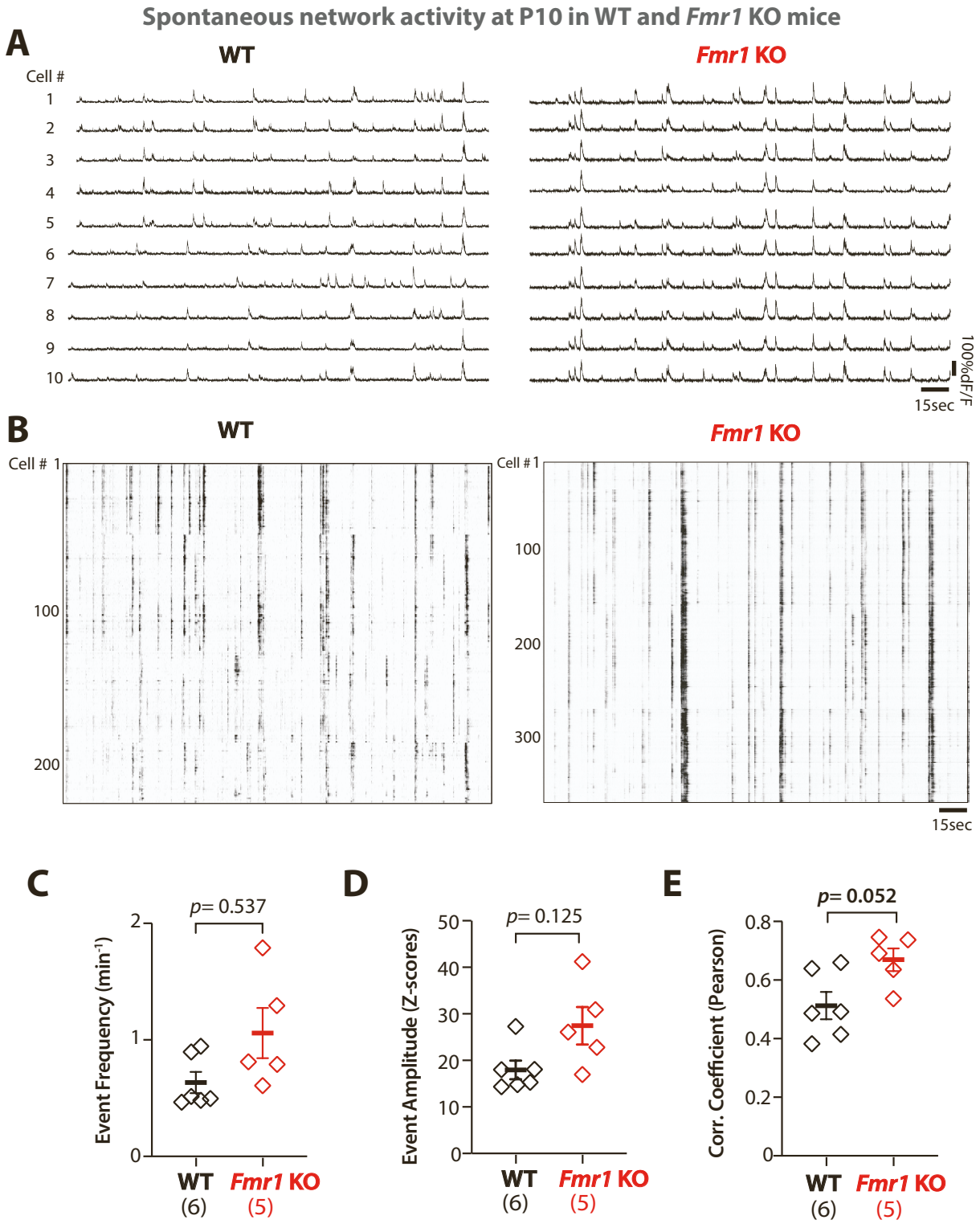

Supplementary Fig. S4

Supplementary Fig. S4: Pyr cell activity at P10 in *Fmr1* KO is hypersynchronous. (Related to Fig. 2)

A. Representative calcium traces of 10 example Pyr neurons in S1 of P10 WT and *Fmr1*^{KO}.
B. Raster plots of Pyr cell activity in a representative WT and *Fmr1* KO mouse. Note the higher synchrony of network *Fmr1* KO.
C. Mean frequency of Pyr cell calcium transients is not significantly different in WT and *Fmr1* KO mice (0.63± 0.09 in WT mice; 1.60± 0.21, n=6 WT and n=5 *Fmr1* KO mice, p=0.537 MW test).
D. Mean amplitude of Pyr cell calcium transients is not significantly different in WT and *Fmr1* KO mice (23.6± 2.00 in WT mice; 27.5± 4.0, n=5 WT and n=6 *Fmr1* KO mice, p=0.125, MW test).
E. Mean pairwise correlation coefficients is higher in *Fmr1* KO mice as compared to WT (0.51± 0.05 in n=6 WT mice; 0.67± 0.04, and n=5 *Fmr1* KO mice, p=0.052, MW test).

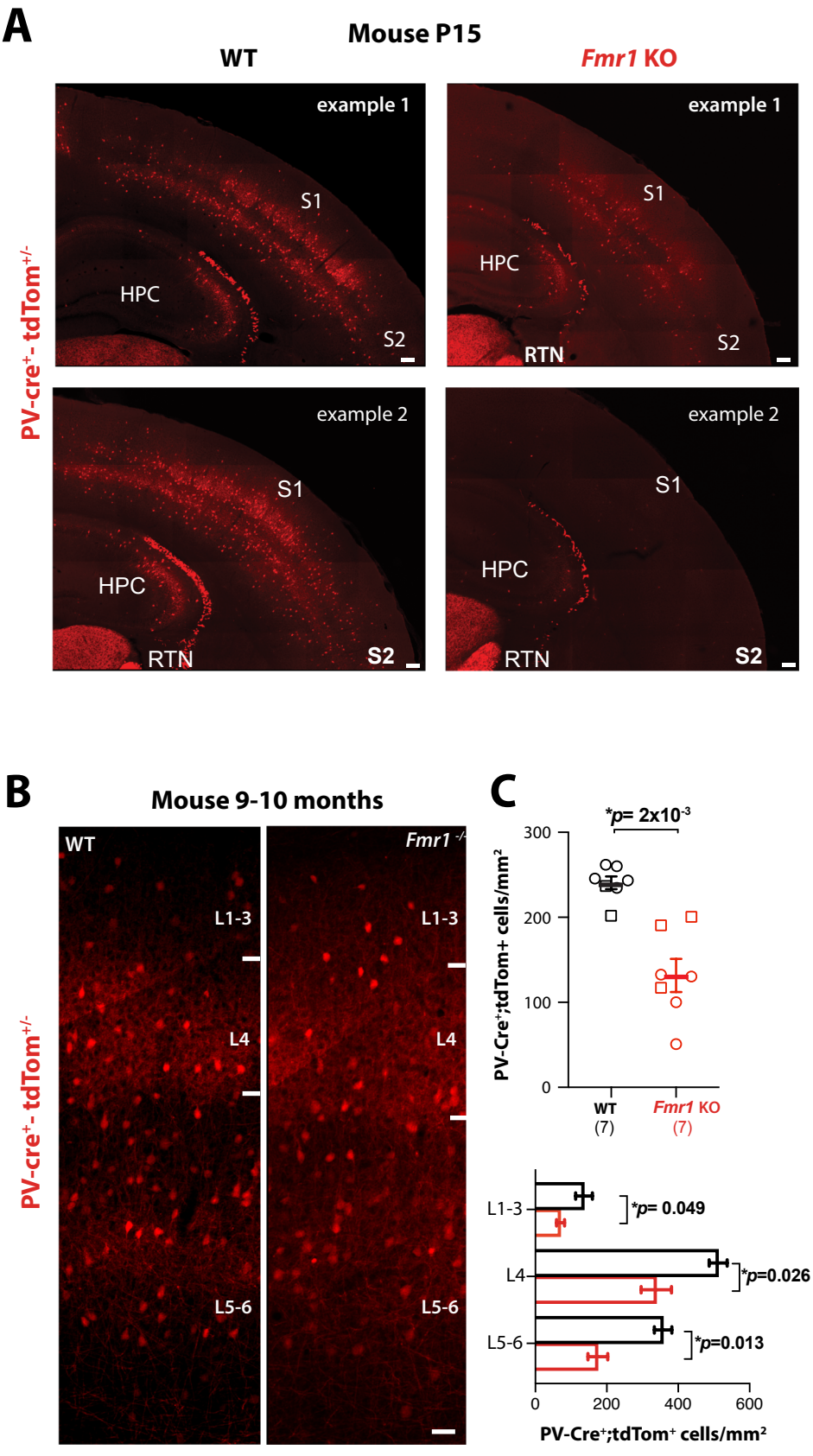

Supplementary Fig. S5

Supplementary Fig. S5: Reduced PV-IN density in *Fmr1* KO mice at P15 and at 9-10 months. (Related to Fig. 3)

A. Example coronal sections through S1 from *PV*-Cre;tdTom$^{+/-}$ mice (WT and *Fmr1*^{KO}) at P15 showing the range of PV-IN density in *Fmr1* KO mice across the dorsal brain. Notably some *Fmr1* KO mice (example 2) exhibit a dramatic loss of PV-INs in neocortex and hippocampus (HPC), while other bran regions, such as the reticular thalamic nucleus (RTN) are much less affected. S2: secondary somatosensory cortex. Scale=100 μm.

B. Coronal sections through the barrel field of S1 from PV-Cre;tdTom$^{+/-}$ mice (WT and *Fmr1* KO) at 9-10 months (corresponding approximately to age of human tissue in Fig. 3C-D). Scale= 50 μm.

C. Mean density of PV-tdTom^{+} INs in S1 is significantly lower in adult *Fmr1* KO mice (top), even across individual cortical layers (bottom). (all layers: 241± 8 cells/mm^2 for WT vs. 132± 2 for *Fmr1* KO; p=0.002, MW *t*-test; L2/3: 136± 23 vs. 69± 10, p=0.049, L4: 512± 26 vs. 339± 43, p=0.026; L5/6: 358± 24, two-way ANOVA, post-hoc Holm-Sidak test, p=0.013, n=7 per genotype).

SST-IN density in 15 day-old and adult WT and *Fmr1* KO mice

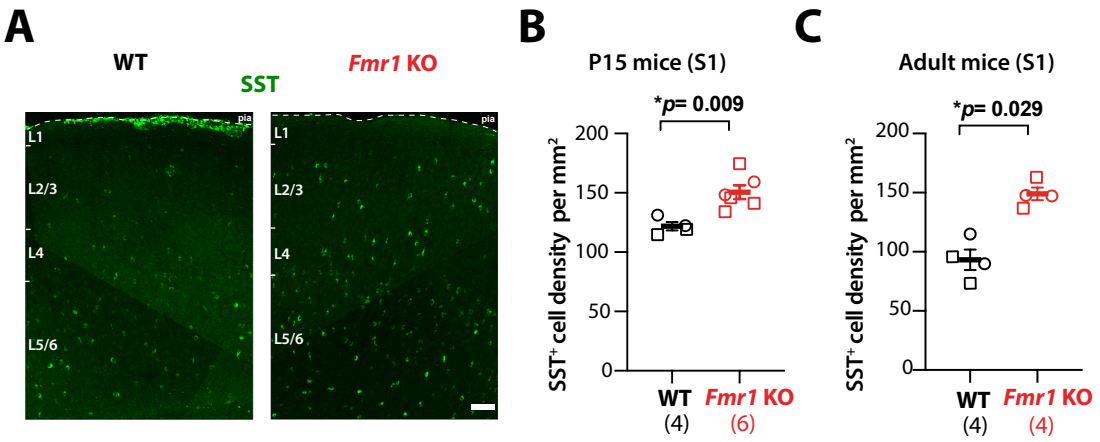

Density of Calretinin- and Calbindin-expressing interneurons subtypes in adult adult WT and *Fmr1*$^{-/-}$ mice

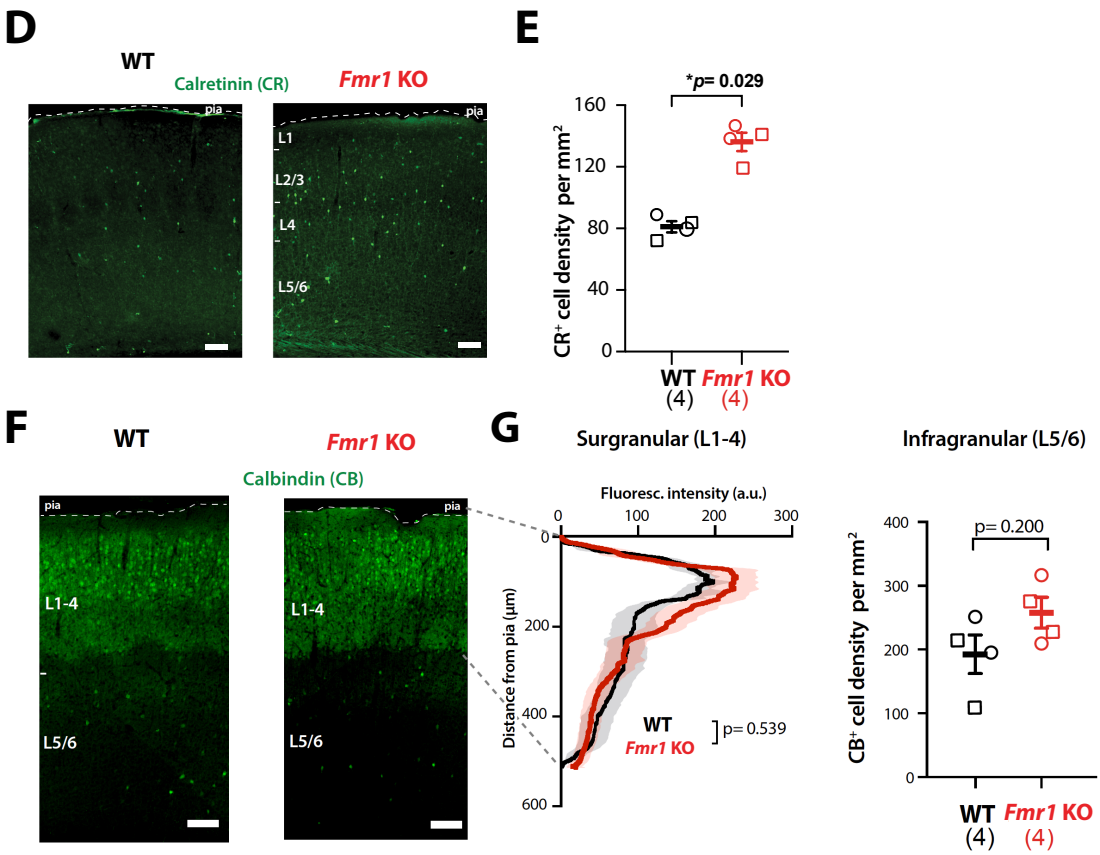

Density of Calretinin- and Calbindin-expressing interneurons in human samples

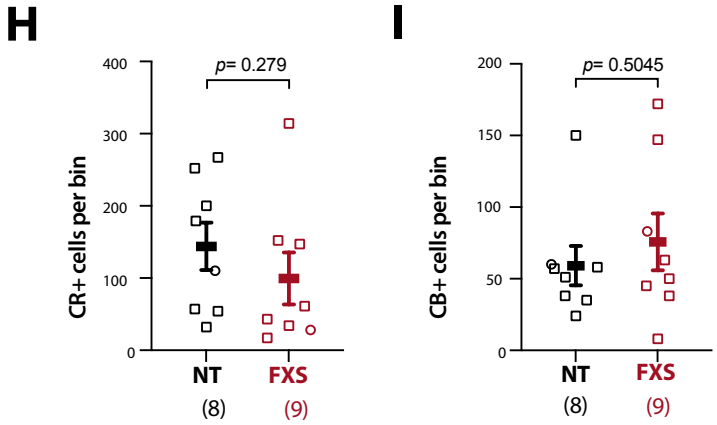

Supplementary Fig. S6

Supplementary Fig. S6: Density of SST, Calbindin, and Calretinin INs in FXS human cases and *Fmr1* KO mice. (Related to Fig. 3)

A. Representative images of SST immunostaining in S1 in P15 WT and *Fmr1* KO mice.
B. Quantification of total SST-immunoreactive cell density in the barrel field of S1 in WT and *Fmr1* KO mice in P15 (WT: 121.9± 3.7 cells/mm^2, *Fmr1* KO: 150.5± 5.9, n= 4 and 6, respectively; p=0.009, MW test).
C. Quantification of total SST-immunoreactive cell density in adult (4-5 months old) WT and *Fmr1* KO mice in and adult mice (WT: 93.14± 8.6 cells/mm^2, *Fmr1* KO: 149.1± 5.3, n= 4 per group; p=0.029, MW test)
D. Representative images of Calretinin immunostaining in S1 in adult WT and *Fmr1* KO mice.
E. Quantification of Calretinin-immunoreactive INs from adult WT and *Fmr1* KO mice (81± 3.6 for WT vs. 136± 5.9 for *Fmr1* KO, n=4 mice per group; p=0.029 MW *t* test).
F. Representative images of Calbindin immunostaining in S1 in adult WT and *Fmr1* KO mice. Note that the CB immunoreactivity is similar to previous reports. [2,3]
G. Quantification of Calbindin-immunoreactive INs in WT and *Fmr1* KO mice. The distribution and intensity of fluorescence is comparable in between WT and *Fmr1* KO mice in the supragranular layers (AUC= 48,036± 704 for WT vs. 42,093± 578 for *Fmr1* KO, n=4 mice per group; p=0.539, MW *t* test). The density of CB$^+$ INS in infragranular layers is similar between WT and *Fmr1* KO mice (192.6± 30.2 for WT vs. 257.7± 24.2 for *Fmr1* KO; p=0.200, MW *t* test).
H. Quantification of Calbindin-immunoreactive INs in human FXS and neurotypical control (NT) cases (59± 14 for NT vs. 76± 20 for FXS, n=8 and 9, respectively; p=0.279 MW *t* test).
I. Quantification of Calretinin-immunoreactive INs in FXS human and control (NT) cases (144± 33 for NT vs. 100± 36 for FXS; p=0.279 MW *t* test).

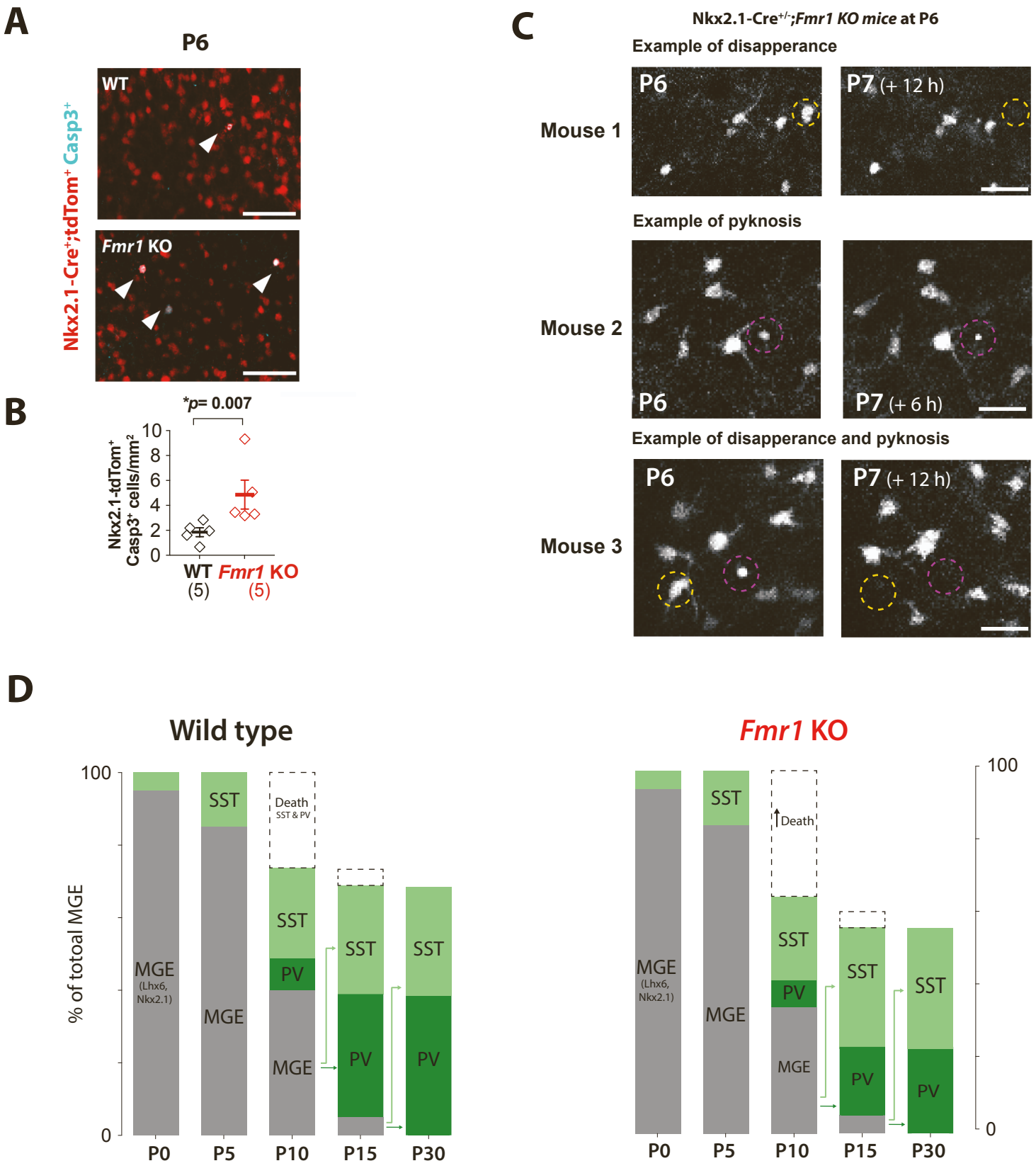

Supplementary Fig. S7

Supplementary Fig. S7: Evidence of apoptotic cell death of *Nkx2.1*-tdTom$^+$ INs in neonatal *Fmr1* KO mice. (Related to Fig. 3)

A. Coronal sections through S1 from *Nkx2.1-Cre* mice (WT and *Fmr1* KO) at P6 immunostained for cleaved Caspase-3 (cyan) showing rare double-labeled cells (arrowheads). Scale= 100 μm.

B. Mean density of Nkx2.1$^+$-tdTom$^+$-INs that co-express Caspase-3 was significantly higher in *Fmr1* KO mice (1.85± 0.35 cells/mm^2 for WT vs. 4.87± 1.16 for *Fmr1* KO; p=0.007, M-W test).

C. Representative maximum intensity projection (~20 μm) of *Nkx2.1*-tdTom$^+$ IN image stacks acquired by in vivo 2P microscopy of the same FOV at P6 and 6-12h later in 3 example *Nkx2.1-Cre;Ai14* $^{+/-}$; *Fmr1* KO mice. Yellow dotted contours indicate *Nkx2.1*-tdTom$^+$ INs present at P6 but absent at P7. Purple dotted contours indicate pyknotic Nkx2.1$^+$-tdTom$^+$-INs, indicative of apoptosis. Scale= 50 μm.

D. Cartoon representing developmental sequence of events related to differentiation of MGE-derived INs into SST and PV populations in WT (left) and *Fmr1* KO mice (right). Note that in WT mice, SST-INs differentiate before PV-INs, that naturally occurring cell death of SST-INs and PV-INs occurs roughly between P5 and P10, and that additional differentiation of PV-INs from MGE-derived precursors goes on after P15. In contrast, in *Fmr1* KO mice, there is 1. A lower density of PV-INs (due to an excess cell death), and 2. a higher density of SST-INs (presumably due to less cell death and/or greater differentiation from MGE-INs) compared to WT mice.

Chronic DREADD manipulation (P5 to P9)
in *Nkx2.1-Cre$^{+/-}$; WT or Fmr1* KO

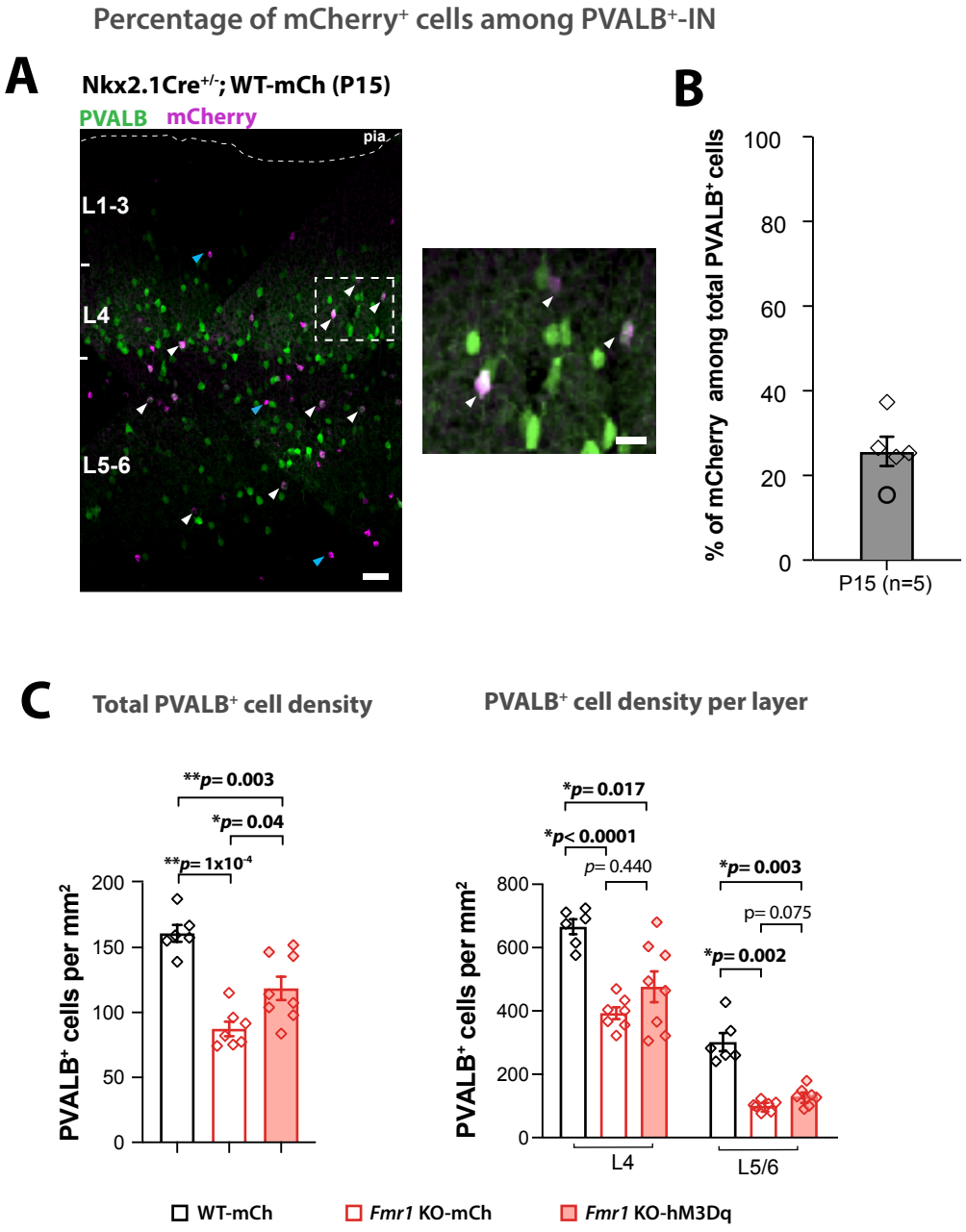

Supplementary Fig. S8

Supplementary Fig. S8: Chronic chemogenetic activation of Nkx2.1-INs (P5-P9) increases the density of PVALB$^+$ cells at P21. (Related to Fig. 4)

A. Coronal section through the barrel field of S1 in a P15 Nkx2.1-Cre;WT mouse expressing mCherry in Nkx2.1$^+$-IN (see Methods). Note the overlap in expression of mCherry (purple) in Nkx2.1$^+$-IN and PVALB immunoreactivity (green) across cortical layers (white arrowheads). As expected based on the low efficiency of viral transduction, only a small proportion of PVALB+ cells co-express mCherry (and the Gq DREADD construct) (blue arrowheads). Scale= 50µm.
B. Percentage of PVALB$^+$ INs that also express mCherry. (25.8± 3.5 cells/mm^2, n=5 mice).
C. Left: Quantification of PVALB+ INs density across cortical layers at P15. (161± 6 cells/mm^2 for WT-mCherry vs. 87± 6 for *Fmr1* KO-mCherry, p= 0.003; and 119± 9 for *Fmr1* KO-h3MDq, p= 0.040, n=6, 7 and 8, respectively). Right: the chronic DREADD manipulation did not significantly change the density of PV-INs in L4 or L5/6.

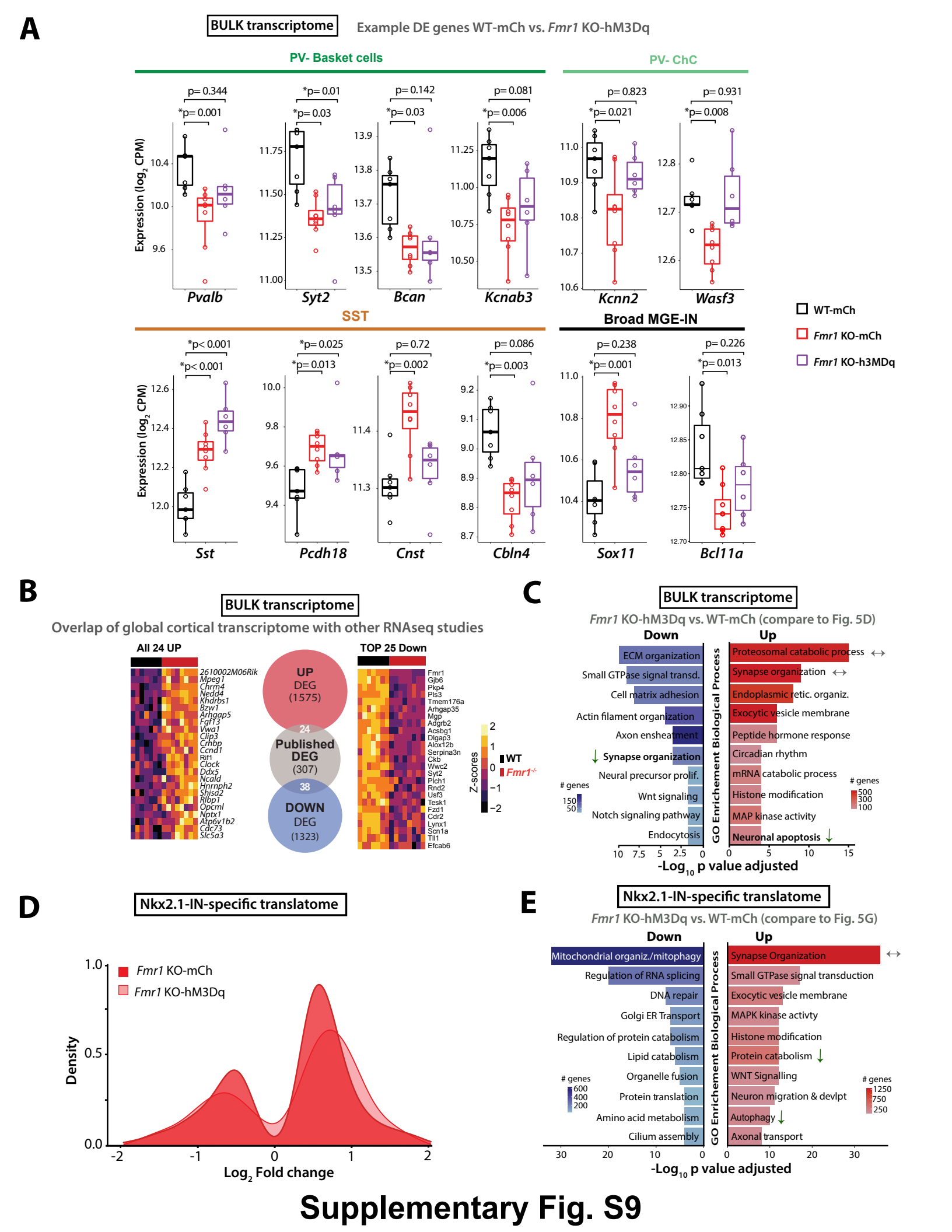

Supplementary Fig. S9

Supplementary Fig. S9: Gene ontology (GO) analysis for DE genes in *Fmr1* KO-hM3Dq mice compared to WT-mCherry mice, and effect of Gq DREADD manipulation. (Related to Fig. 5)

A. Whisker plots comparing the expression of several MGE-derived markers in the bulk transcriptome. Markers shown for PV-INs, including fast-spiking basket cells and chandelier cells, and SST-INs markers; Wilcoxon signed-rank test.
B. Number of DE genes in S1 cortex at P15 *Fmr1* KO-mCherry from the bulk transcriptome that overlap with previously reported differentially expressed in the hippocampus of adult *Fmr1* KO mice (see Methods). Heatmaps represent the changes of expression expressed as Z-scores among the up- and downregulated genes.
C. Top 10 GO terms (using the biological process package) enriched among downregulated (blue) and upregulated (red) genes from the bulk cortical transcriptome in *Fmr1* -hM3Dq vs. WT-mCherry mice. Scale bars represent the number of genes in each category. Note that "*Synapse organization*" and "*Neuronal apoptosis*" categories are less different (reduced number of genes and adjusted p value) than in the comparison shown in Fig. 5D between *Fmr1* KO (mCherry) and WT (mCherry) mice, suggesting they were 'improved' by the chemogenetic activation of Nkx2.1-INs.
D. Density plot showing how the $\log_2$ fold change was affected by the DREADD manipulation in the Nkx2.1-IN specific translatome. Note that differences with WT mice were accentuated by the DREADD intervention in both down- ad upregulated categories.
E. Top 10 GO terms for DE genes from the Nkx2.1-specific translatome in *Fmr1* KO -hM3Dq vs. WT-mCherry mice. Only a few GO terms were modestly improved by DREADDs (e.g., *Protein catabolism* and *Autophagy*).

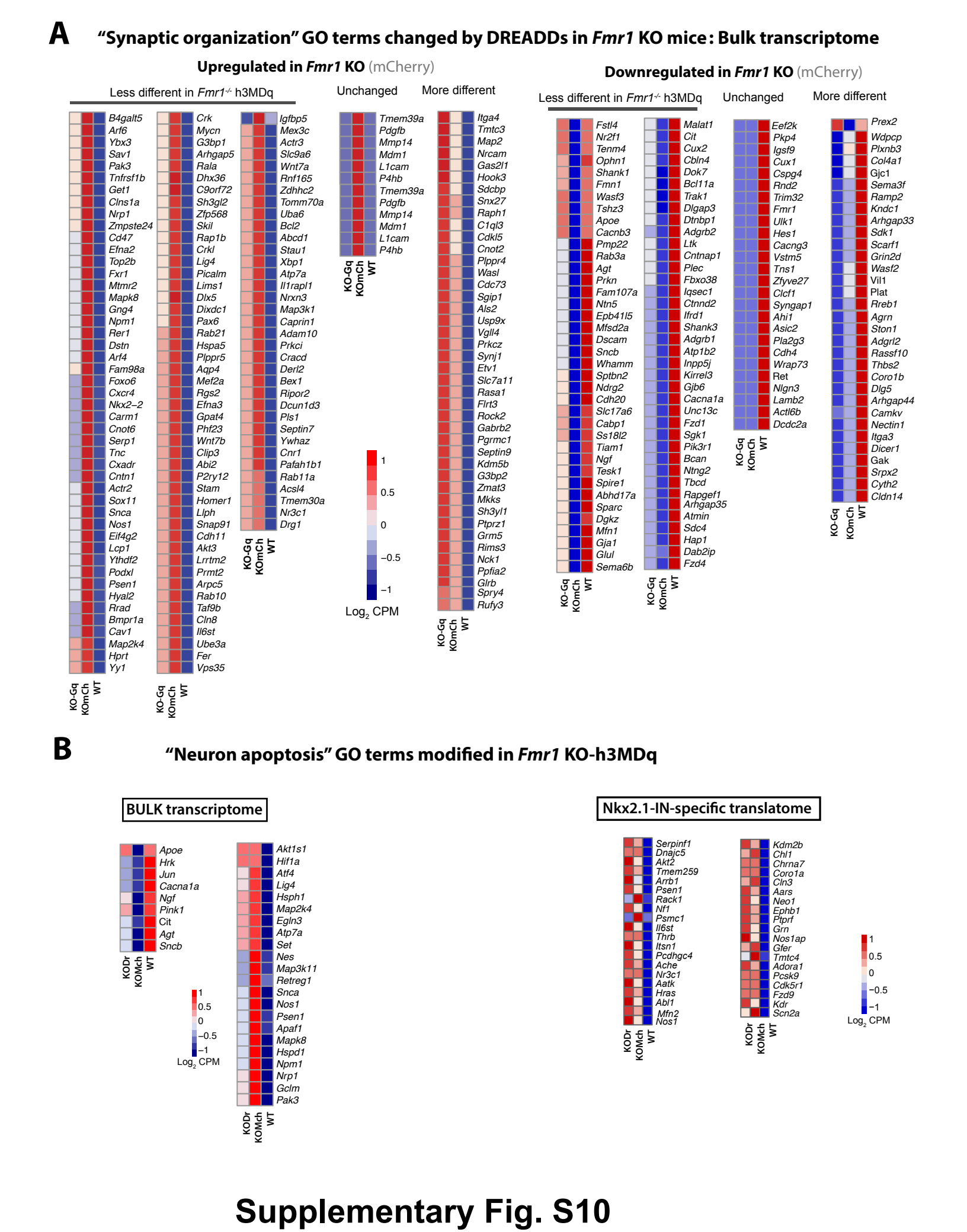

Supplementary Fig. S10

Supplementary Fig. S10: Gene expression levels changed by C21 treatment in *Fmr1* KO-hM3Dq mice. (Related to Fig. 6)

A. List of upregulated or downregulated genes among the GO term *Synapse organization* in *Fmr1* KO-mCherry and hM3Dq groups (as compared to WT-mCherry) within the bulk cortical transcriptome. Heatmaps represent the average for each treatment/genotype group in (log_2 CPM). Note that, while DREADD treatment reduced differences for many genes. The expression of other genes was either unhanged or worsened after C21 treatment.

B. Same as in panel A but for GO term "*Neuronal apoptosis*." In both bulk transcriptome (left) and Nkx2.1-IN specific translatome (right).

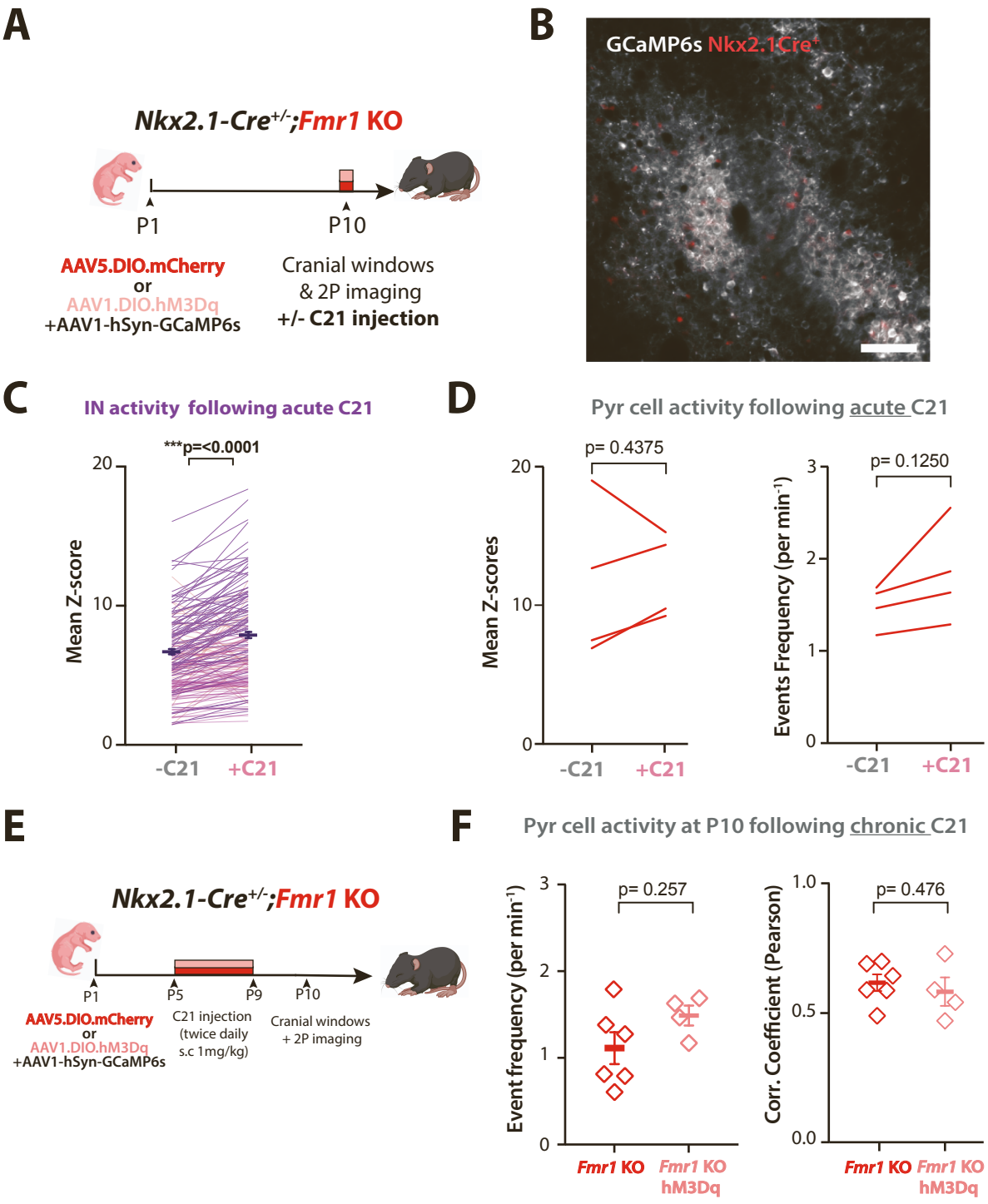

Supplementary Fig. S11

Supplementary Fig. S11: Acute chemogenetic activation of Nkx2.1-INs at P10 or chronic activation from P5 to P9, fails to modulate Pyr cell activity. (Related to Fig. 7)

A. Experimental design for acute chemogenetic activation of Nkx2.1-INs at P10 in *Fmr1* KO mice to assess cortical circuit activity using in vivo calcium imaging at P10.
B. Example FOV of Pyr cells expressing GCaMP6s and Nkx2.1-hM3Dq^{+} IN in S1 of *Nkx2.1-Cre; Fmr1* KO mouse (scale=100μm).
C. Mean Z-scores of Nkx2.1-INs before (-C21) and 30-40min after s.c. injection of C21 (+C21) in P10 *Fmr1* KO-hM3Dq mice. Mean activity of Nkx2.1-INs is significantly higher following C21 injection (-C21: 6.61± 0.19 and +C21: 7.83± 0.23, n= 182 cells from 3 mice; $p<0.0001$, Wilcoxon matched-pairs signed rank test).
D. Left: Mean Z-scores of Pyr cells before (-C21) and 30-40min after (+C21) s.c. injection of C21 (1mg/kg) in P10 *Fmr1* KO-hM3Dq mice. Acutely increasing the activity of Nkx2.1-INs had no effect on Pyr cell activity (-C21: 11.52± 2.82 and +C21: 12.16± 1.55, p=0.437, Wilcoxon matched-pairs signed rank test). Right: the mean frequency of synchronous network events (Pyr cells) remained unchanged after C21 in P10 *Fmr1* KO-hM3Dq mice. (-C21: 1.48± 0.11 and +C21: 1.83± 0.26 events/min, n= 4 mice; p=0.125, Wilcoxon matched-pairs signed rank test).
E. Experimental design for chronic chemogenetic activation of Nkx2.1-INs (from P5 to P9) in *Fmr1* KO mice to assess cortical circuit activity using in vivo calcium imaging at P10.
F. Left: Mean frequency of Pyr cell calcium transients at P10 was not significantly different *Nkx2.1-Cre; Fmr1* KO -hM3Dq mice after chronic C21 injections from P5 to P9 compared to *Fmr1* KO mice (1.11± 0.18 in *Fmr1* KO n=6 vs. 1.48± 0.11 events per min in *Fmr1* KO-hM3Dq mice n=4, p=0.257, MW test test). Right: Mean pair-wise correlation coefficients of Pyr cell calcium transients is unchanged in *Fmr1* KO-hM3Dq mice following chronic C21 injection from P5 to P9 (0.66± 0.03 in *Fmr1* KO n=6, and 0.62± 0.05 in *Fmr1* KO-hM3Dq mice n=4, p=0.476 MW test). Note that 1 animal was a new *Fmr1* KO-mCherry control, while the other 5 mice are *Fmr1* KO from Fig S4C-E.

Acute DREADD manipulation of PV-IN reduces spontaneous Pyr cell activity in P15 Fmr1 KO mice

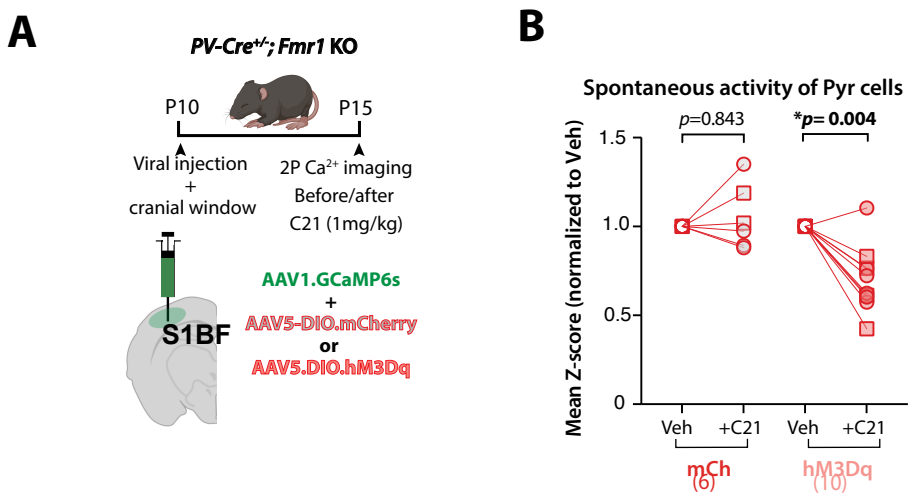

Acute optogenetic manipulation of MGE-IN reduces Pyr cell activity P15 Fmr1 KO mice

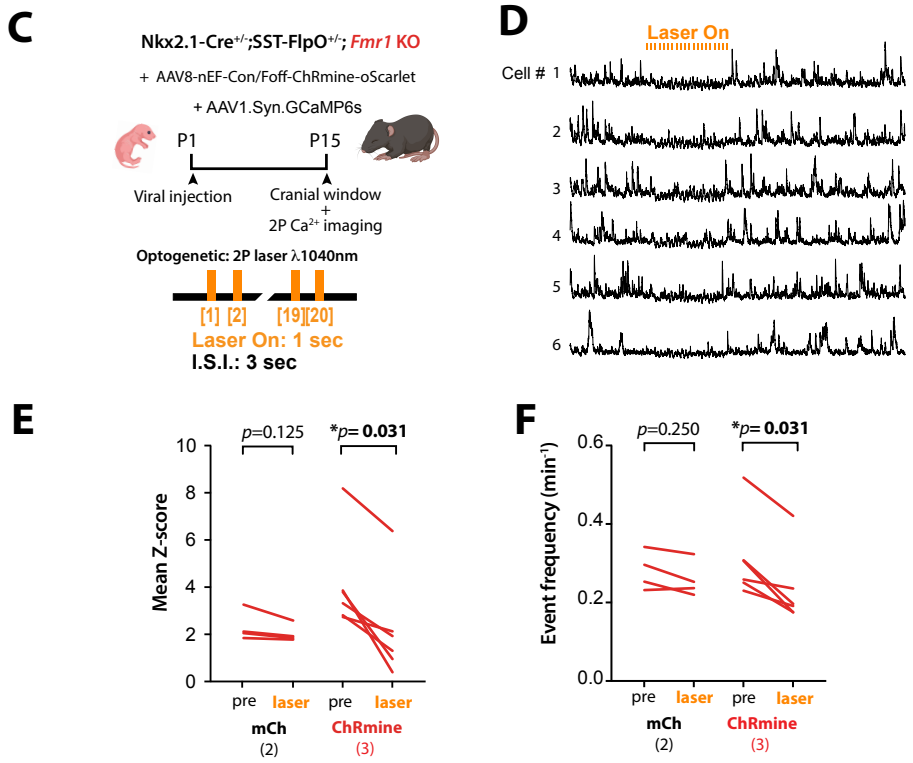

Acute DREADD manipulation of PV-IN modulates whisker-evoked responses

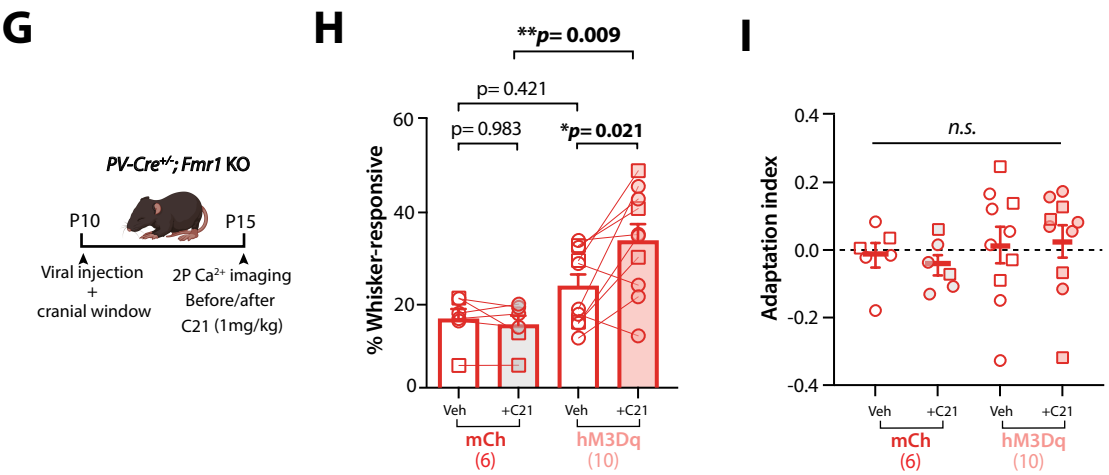

Supplementary Fig. S12

Supplementary Fig. S12: Acute chemogenetic or optogenetic activation of INs reduces Pyr cell activity at P15 in *Fmr1* KO mice. (Related to Figs. 7 and 8)

A. Experimental design for in vivo calcium imaging recordings in Pyr cells after acute chemogenetic activation of PV-INs at P15. Calcium imaging was performed at P15 before and 30-40min after s.c injection of C21.

B. Mean Z-score for spontaneous activity of L2/3 Pyr cells is reduced upon C21 injection in *Fmr1* KO -hM3Dq mice but not in *Fmr1* KO mCherry controls (before/after C21: 3.9± 0.7 vs. 4.0± 0.6 in mCherry group, p=0.843; and 2.3± 0.3 vs. 1.6± 0.3, p=0.004 in hM3Dq group; n=6 and 10 mice, respectively; Wilcoxon matched pair signed rank test).

C. Experimental design for optogenetic experiments. *Nkx2.1*-Cre mice (*Fmr1* KO or WT) were injected with a CreOn/FlpOff-ChRmine virus at P1 to express the opsin ChRmine in Nkx2.1-Cre^{+}; Sst-FlpO^{-} INs. Calcium imaging was done at P15 before, during, and after 20 laser pulses of orange light (1 s-long, 3 s I.S.I., λ=1,040 nm), just as in Fig. 2.

D. Representative calcium traces for 6 Pyr cells (black) upon 2P laser stimulation.

E. Mean Z-score of activity in Pyr cells before (pre) and during optogenetic stimulation (laser) in *Fmr1* KO mice. Each line in the panel represents an individual field of view. We observe a significant reduction of Pyr cell activity upon laser stimulation in ChRmine-expressing mice but not in control mCherry mice (2.32± 0.32 pre vs. 2.03± 0.18 with laser; p= 0.125; n=4 FOV from 2 control mice) ; 4.12± 0.83 pre vs. 2.18± 0.87 with laser; n=6 FOV from 3 ChRmine-expressing mice ; p= 0.019. Wilcoxon matched-paris signed rank test).

F. Mean event frequency of calcium transients of Pyr cells before (pre) and during optogenetic stimulation (laser) in P15 *Fmr1* KO mice. We observe a significant reduction of Pyr cell activity upon laser stimulation in ChRmine-expressing mice but not in control m-Cherry mice (0.28± 0.02 pre vs. 0.25± 0.02 with laser; p= 0.250 in control mice; 4.12± 0.83 pre vs. 2.18± 0.87 with laser for ChRmine-expressing mice; p= 0.031, Wilcoxon matched-pairs signed rank test).

G. Experimental design for calcium imaging recordings in Pyr cells after acute chemogenetic activation of PV-INs at P15 with the hM3Dq DREADD agonist C21 (same as Suppl. Fig. S12A-B).

H. The percentage of whisker-responsive Pyr cells at P15 was significantly higher in upon C21 injection in *Fmr1* KO-hM3Dq mice (n=10) but not in *Fmr1* KO mCherry controls (n=6). (hM3Dq group before/after C21: 23.5± 2.8% vs. 33.9± 3.9%; p=0.021; and mCherry group before/after C21: 15. 9± 2.3% vs. 14.5± 2.1%; p=0.983; two-way *ANOVA* with post-hoc Tukey).

I. Neuronal adaptation was not affected by the DREADD manipulation (mCherry group before/after C21: -0.02± 0.09 vs. -0.05± 0.03, hM3Dq group: 0.02± 0.05 vs. 0.03± 0.05, p>0.99; two-way *ANOVA* with post-hoc Tukey).

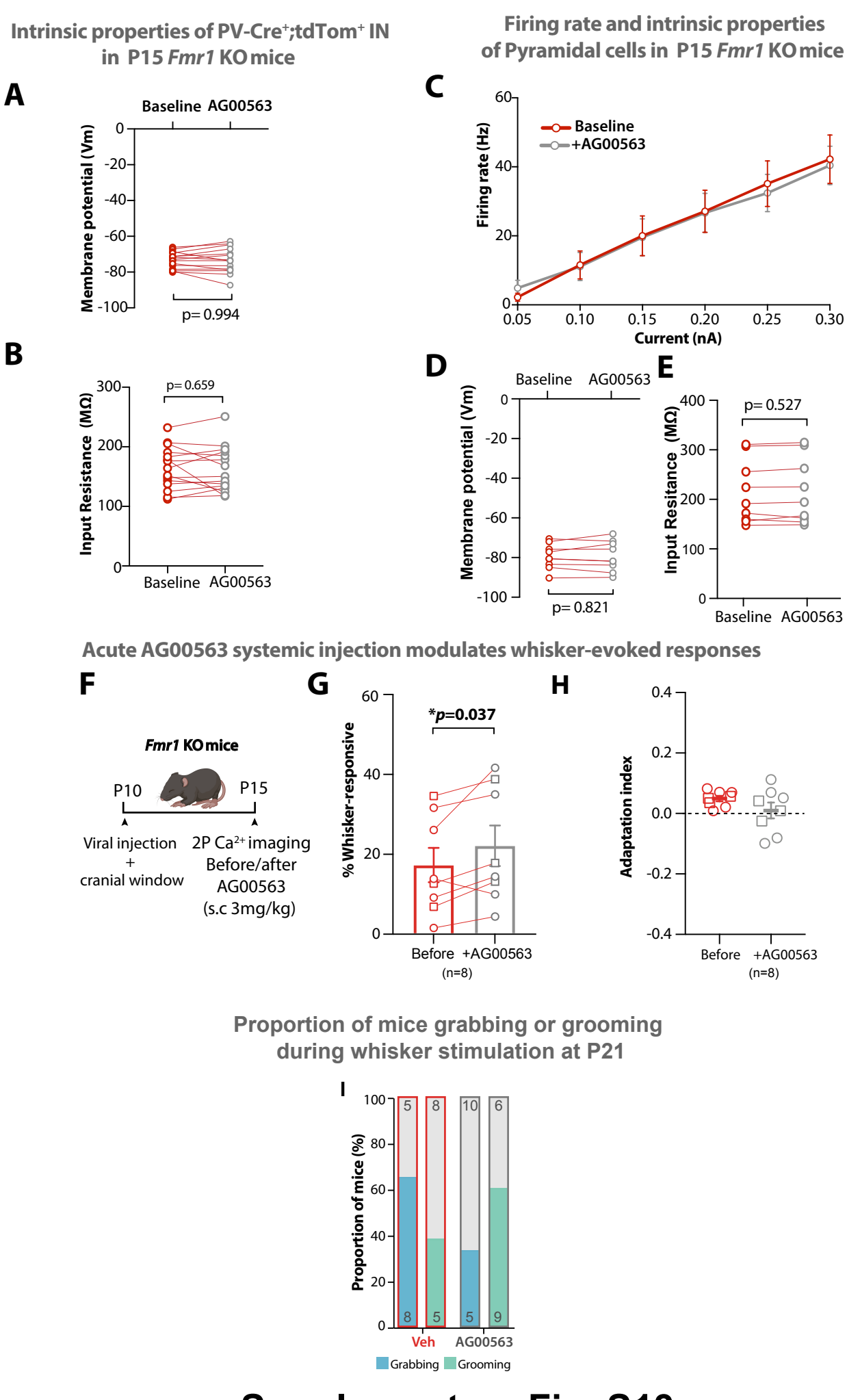

Supplementary Fig. S13

Supplementary Fig. S13: Intrinsic properties of PV-INs and Pyr cells are unchanged by AG00563 (and relative proportions of grabbing/grooming in AG00563 treated mice).

(Related to Fig. 8)

A. Resting membrane potential (Vm) of PV-INs is unchanged by bath application of AG00563 during current clamp recordings of *PV*-tdTom+ cells (-73.4± 1.2 mV vs. -73.2± 1.8 mV, p= 0.805, paired t-test, n=15 cells from 6 *Fmr1* KO mice at P15-16).
B. Input resistance (Rm) of PV-INs is unchanged by AG00563 (164.6± 9.2 MΩ vs. 161.2± 10.1 MΩ, p= 0.608, paired *t*-test).
C. Cumulative input-output curves during baseline (red) or bath application of AG00563 (gray) (n=9 Pyr cells from 6 PV-Cre;tdTom+/-;*Fmr1* KO mice, two-way RM ANOVA).
D. Vm of Pyr cells is unchanged by AG00563 (-79.5± 2.1 mV vs -79.3± 2.5 mV, p=0.805, paired t-test).
E. Rm of Pyr cells is unchanged by AG00563 (214.0± 21.4 MΩ vs. 215.4± 22.0 MΩ, p=0.608, paired *t*-test).
F. Experimental design for the acute administration of AG00563 (3 mg/kg, s.c.) and calcium imaging at P15, before and 30 min after injection.
G. The percentage of whisker-responsive Pyr cells in *Fmr1* KO mice was significantly higher after AG00563 injection compared to baseline (17.1± 4.3% baseline vs. 21.9± 5.1% ~30-40 min after AG00563, p=0.033; paired t-test, n=8 mice).
H. The neuronal adaptation index of Pyr cells was not changed by AG00563 (0.05± 0.01 baseline vs. 0.01± 0.03 after AG00563, p=0.033; paired t-test, n=8 mice).
I. A smaller percentage of mice showed defensive behavior (grabbing) at least once during whisker stimulation in the AG00563-treated group than among vehicle controls (5/15 mice vs. 8/13, respectively). The opposite was true for adaptive healthy behavior (grooming) (9/15 mice vs. 5/13, respectively).

Case ID	Sex	Age	PMI (Hours)	Diagnosis	CGG Repeat Count	Hemisphere	Cause of Death
UCD 14-15	M	60	80	Control	NA	Right	Pulmonary Emboli
UCD 18-05	M	62	37	Control	NA	Left	Cardiopulmonary Arrest
UCD 15-07	F	64	NK	Control	NA	Left	NK
UCD 18-07	M	65	240	Control	NA	Left	Cardiac Arrest
UCD 14-01	M	66	48.5	Control	NA	Right	Acute Renal Failure
UCD 18-08	M	68	168	Control	NA	Left	Hypoxic Respiratory Failure
UCD 14-12	M	68	NK	Control	NA	Left	Cardiac Arrest
UCD 19-12	M	81	72	Control	NA	Left	NK
1031-08-GP	M	57	20	FXS	436	Left	Multiple System Organ Failure
1031-09-LZ	M	64	11.5	FXS	429	Left	NK
1061-19-JB	F	64	30	FXS	629,780	Left	NK
1005-14-JC	M	65	60	FXS	600-700	Right	Congestive Heart Failure
1013-10-SK	M	76	NK	FXS & FXTAS	447,540	Left	Respiratory Failure
1001-18-LD	M	78	6	FXS	235	Right	NK
1033-08-WS	M	79	17.5	FXS		Left	NK
1007-18-RF	M	80	NK	FXS	1,000	Right	NK

Table S1. Clinical characteristics of postmortem neurotypical and Fragile X cases.
(Related to Figure 3).
(NK: not known; NA: not applicable; M: male; F: female; PMI: post-mortem interval; FXS: Fragile X syndrome; FXTAS: Fragile X-associated tremor/ataxia syndrome).

SUPPLEMENTAL VIDEOS

Supplementary video 1 (Related to Fig. 2). Example of in vivo calcium imaging of Pyr cells before, during, and after optogenetic stimulation of presumed future PV-IN s in Nkx2.1-Cre;SST-Flp$^{+/-}$ mice at P10. Data was acquired at 15 fps and is played back at 2x speed.

Supplementary video 2 (Related to Fig. 4). Example of in vivo calcium imaging of Pyr cells during whisker-evoked activity in Nkx2.1-Cre mice at P2. Data was acquired at 15 fps and is played back at 1x speed.

References

1. Che, A., Babij, R., Iannone, A.F., Fetcho, R.N., Ferrer, M., Liston, C., and García, N.V.D.M. (2018). Layer I Interneurons Sharpen Sensory Maps during Neonatal Development. Neuron *99*, 98-116.e7. 10.1016/j.neuron.2018.06.002.

2. Nigro, M.J., Hashikawa-Yamasaki, Y., and Rudy, B. (2018). Diversity and Connectivity of Layer 5 Somatostatin-Expressing Interneurons in the Mouse Barrel Cortex. Journal of Neuroscience *38*, 1622–1633. 10.1523/jneurosci.2415-17.2017.

3. Daigle, T.L., Madisen, L., Hage, T.A., Valley, M.T., Knoblich, U., Larsen, R.S., Takeno, M.M., Huang, L., Gu, H., Larsen, R., et al. (2018). A Suite of Transgenic Driver and Reporter Mouse Lines with Enhanced Brain-Cell-Type Targeting and Functionality. Elsevier Inc. *174*, 465-480.e22. 10.1016/j.cell.2018.06.035.